Università degli Studi di Genova
SCUOLA DI SCIENZE MATEMATICHE, FISICHE E NATURALI

XXXVIII Cycle of Ph.D. in Physics and Nanoscience

Superconducting Cables Development for High Energy Physics and Power Grids

Candidate:
Michela Bracco

Supervisors:
Riccardo Musenich
Stefania Farinon
Matteo Cialone

Data

In Partnership With

Politecnico di Torino

INFN
Istituto Nazionale di Fisica Nucleare

Contents

List of Figures

List of Tables

Introduction

Superconducting materials find application in a variety of advanced technologies, including components for high-energy physics experiments and systems for the transmission of electrical power with extremely low losses. In these applications, the performance of the conductors also depends on their mechanical response. From the earliest stages of manufacture right through to operational use, they are subjected to forces and deformations capable of altering their internal structure, affecting the shape of the components and the microstructure, with direct effects on their transport properties. The study of mechanical behaviour is therefore essential for understanding their performance and optimising the design of superconducting systems.

Within this framework, the thesis reports two studies on different materials and applications, which share the use of finite element modelling to investigate the mechanical behaviour of the conductors. The first study focuses on Nb_3Sn wires used in the manufacture of high-field magnets for particle accelerators. Magnets such as quadrupoles and dipoles developed for the upgrade of the HL-LHC at CERN or for future ultra-high-energy accelerators, such as the 14 T dipoles planned for the Future Circular Collider (FCC), operate at magnetic fields higher than those achievable with the Nb-Ti conductors currently in use. This necessitates the use of higher-performance superconducting materials, with Nb_3Sn being the preferred choice. The wires, containing the metallic precursors, are initially assembled into Rutherford cables, which form the basic structure of high-field magnets. These cables are then wound according to the final geometry of the coil. During the processes of cabling and winding, the unreacted wires, which remain in a plastic and deformable state, may be subjected to mechanical stresses that result in local deformations to the multifilamentary structure. This may result in changes to the arrangement and integrity of the filaments. The use of finite element modelling allows the simulation of wire behaviour under deformation, enabling the identification of the geometric configurations most susceptible to cabling-induced stress. This in turn guides the design of cables to minimise performance degradation. Subsequently, the heat treatment of the magnets converts the precursors into Nb_3Sn.

A primary challenge is that Nb_3Sn is brittle, and stresses from cooling, assembly, and Lorentz forces during magnet energisation significantly affect its transport properties. Consequently, the operational range of high-performance, high-field magnets is constrained by these stresses. A preliminary FEM model of the reacted phase was also developed. The aim of this model was to provide a first representation of the mechanical state of the wire after the heat treatment and to establish the basis for future analyses under realistic operating conditions.

The second research line is being carried out as part of the Tricheco project, an Italian High-Relevance National Project, which aims to validate the technical and economic feasibility of a 30-kilometre-long hybrid submarine infrastructure (Superconducting Energy Pipeline, SCEP) located in the Adriatic Sea. This infrastructure is designed to connect an offshore energy hub, comprising wind farms, floating photovoltaic plants and an electrolysis system, to the onshore grid. The pipeline enables the simultaneous transport of low-loss direct current (DC) electricity and liquid hydrogen (LH_2). In this architecture, hydrogen fulfils a dual function: it acts as a high-density energy carrier and serves directly as a cryogenic fluid for cooling the MgB_2 multifilamentary superconducting cable, ensuring its operation within a temperature range of 20 K to 29 K. The operating conditions impose stringent structural requirements on both the cryostat and the conductor. In this context, finite element modelling (FEM) can be used to validate the integrity of the corrugated stainless steel cryostat, verifying its stability under the combined action of thermal contraction, the internal pressure gradient and the external hydrostatic pressure typical of a submarine installation at a depth of 40–50 metres. Concurrently, numerical analysis facilitates the study of the mechanical behaviour of the superconductor cable, taking into account thermal contractions governed by the varying coefficients of thermal expansion of the constituent materials. This approach allows for the verification of local stresses on the MgB_2 strands, ensuring they remain within safety limits, and the precise quantification of overall shrinkage of the cable on a kilometre-scale. Accurate determination of this shrinkage is critical for defining the exact manufacturing length of the conductor. An underestimation would mean that the cable, once cooled, would be under tensile stress against the system's fixed-length components, such as joints and terminations. This could generate unwanted stresses capable of compromising the cable's integrity.

In light of the issues discussed above, the aim of this thesis is to analyse the mechanical response of superconducting conductors in different application contexts using finite element modelling. Some of the results presented in this work have been published in scientific journals. In particular:

- M. Bracco, J. Bijlsma, J. Baumann, T. Boutboul, S. Farinon, E. Gautheron, S. C. Hopkins, *Numerical Analysis of Unreacted Nb_3Sn Wires Under Compression*, IEEE Transactions on Applied Superconductivity, vol. 36, no. 5, 2026. doi: 10.1109/TASC.2026.3659580 [1].

- M. Bracco, A. Balbo, C.-E. Bruzek, M. Breschi, L. Cavallucci, S. Farinon, A. Macchiagodena, G. Mangiulli, R. Musenich, L. Soldati, L. Savoldi, *Design of a Submarine 30-km MgB_2 Cable for the Combined Transfer of 0.3 GW_e and LH_2 from Offshore Plants to the Ravenna Port*, IEEE Transactions on Applied Superconductivity, vol. 35, no. 5, 2025. doi: 10.1109/TASC.2025.3528923 [2].

These works serve as direct references for the analyses presented in the following chapters. The thesis is organised as follows. Chapter 1 introduces the fundamental properties of superconducting materials and the main technologies for multifilamentary wires, drawing on the discussion of critical parameters and the phenomenology of Type II materials reported in the literature [3]–[6]. Chapter 2 reviews the state of the art regarding the types of cables used in particle accelerator magnets and power transmission lines. Chapter 3 describes the FEM methodology employed, detailing the two-dimensional and three-dimensional formulations implemented in Ansys. Chapter 4 focuses on the study of unreacted Nb_3Sn wires, analysing the impact of the actual geometry on the distribution of deformations during compression and introducing a preliminary model for the reacted configuration. Chapter 5 presents the results related to the Tricheco project, with emphasis on the thermo-mechanical modelling of the MgB_2 cable and cryostat, and on the quantification of shortening on a kilometre-scale. Finally, Chapter 6 summarises the general conclusions and discusses future prospects, highlighting the impact of the results in both high-field magnets and advanced energy infrastructure.

Chapter 1

Superconductivity and Superconducting Wires

1.1 Introduction to Superconductivity

The phenomenon of superconductivity was first observed by the Dutch physicist Heike Kamerlingh Onnes in 1911, when, while measuring the electrical conductivity of pure metals at very low temperatures, he noticed the abrupt drop to zero of the resistivity of mercury at about 4 K. The behavior was completely unexpected, and Kamerlingh Onnes named this phenomenon superconductivity, a new state of matter. The passage from the normal state to the superconducting state at a certain temperature, called the critical temperature T_c, is therefore a thermodynamic phase transition. In Figure 1.1 one can see the different trends of resistivity as a function of temperature for a non-superconducting metal and for a superconductor. Note that in a normal metal, even at temperatures approaching 0 K, a certain residual resistivity is present, whereas in a superconductor there is a sudden collapse of resistivity at the critical temperature and no residual resistivity.

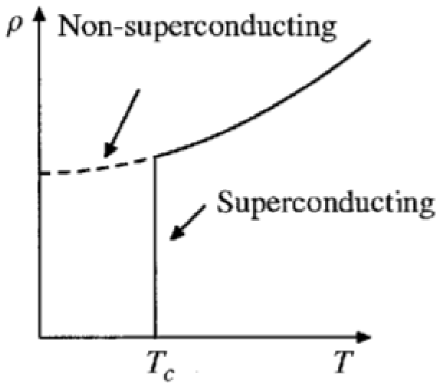

Figure 1.1: Comparison between the resistivities of a normal metal and of a superconductor as a function of temperature [3].

Today we know that not only mercury, but also many elements of the periodic table, under different pressure and/or temperature conditions, exhibit this type of behavior, as reported in Figure 1.2 .

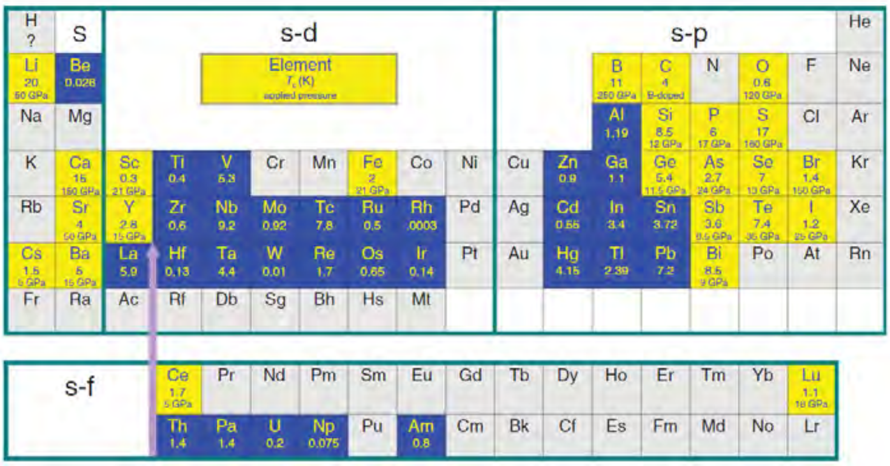

Figure 1.2: Superconducting elements in the periodic table [7].

Among these, niobium (Nb) is the element that, at atmospheric pressure, exhibits the highest critical temperature (9.2 K). Over the years, the phenomenon of superconductivity has then been found in numerous compounds that display very different critical temperatures and properties.

The disappearance of resistance at the critical temperature is not, however, the only distinctive property of superconducting materials. Inside them one also observes the Meissner–Ochsenfeld effect and perfect diamagnetism. The Meissner–Ochsenfeld effect consists of the expulsion of an external magnetic field applied to the superconductor by the superconductor itself. This effect is a property of thermal equilibrium: it does not depend on the sample's history; field expulsion occurs whether the field is applied before cooling down to T_c or after cooling. If diamagnetism were only a consequence of zero electrical resistivity, then, in the case where cooling occurred after the application of the external field, the field would remain trapped inside the material (see Figure 1.3).

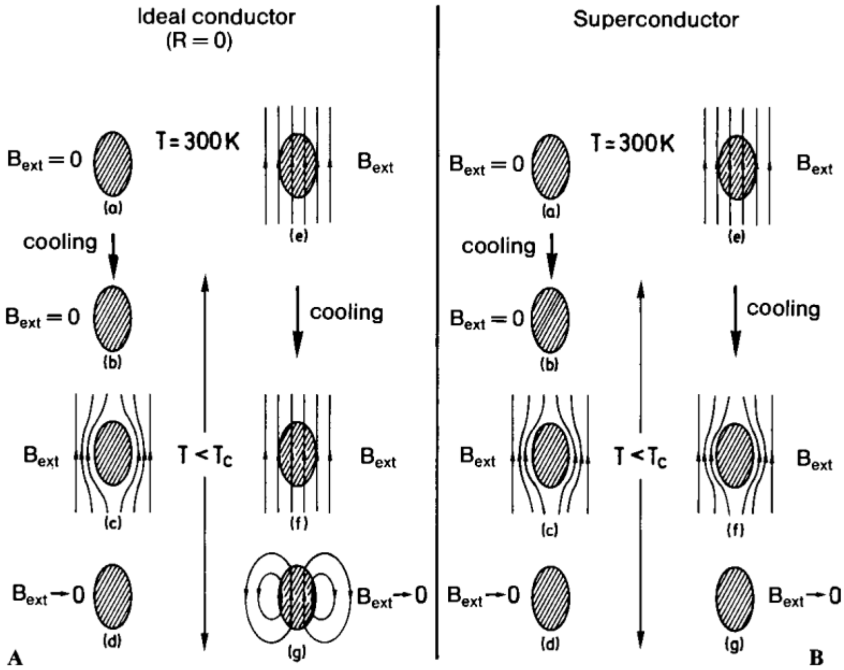

Figure 1.3: Difference between the behaviors of a metal (ideal conductor) and a superconductor when an external magnetic field is applied [8].

Since the magnetic field inside a superconductor must be kept null, screening currents must necessarily be created inside that produce a magnetic field equal and opposite to the applied external magnetic field. In this way one has $B_{\mathrm{tot}} = 0$. One also has that:

$$\mathbf{B} = \mu_0 (\mathbf{H} + \mathbf{M}) \tag{1.1}$$

where **B** is the magnetic induction, **H** is the magnetic field, and **M** the magnetization. Therefore, one obtains:

$$\mathbf{M} = -\mathbf{H} \tag{1.2}$$

The magnetic susceptibility is then defined as:

$$\chi = \left.\frac{dM}{dH}\right|_{H=0} \tag{1.3}$$

For superconductors, therefore:

$$\chi = -1 \tag{1.4}$$

Negative magnetic susceptibility is typical of diamagnetic materials, i.e. materials capable of shielding part of the external magnetic field. Since superconductors have negative susceptibility and completely shield the external magnetic field, they are considered perfect diamagnets.

1.1.1 Type I and Type II Superconductors

What has been described so far holds for relatively low external magnetic fields, but for higher fields two different situations are distinguished. The first case is that of Type I superconductors, in which the field inside the superconductor remains zero until a certain value of the external magnetic field is reached, called the critical field H_c, above which the superconducting behavior disappears. Many superconductors, however, behave in a more complex manner and are called Type II superconductors. In this case two values of critical field are present, the lower H_{c1} and the upper H_{c2}. For values lower than H_{c1}, the behavior is that typical of a superconductor (Meissner phase), and the same properties of Type I superconductors hold. When the applied field exceeds H_{c1} while remaining below H_{c2}, a particular situation arises in which the external magnetic field begins to penetrate inside the material and the magnetization loses its linear trend as a function of the field and begins to rise, approaching zero. Increasing the field beyond H_{c2} one finally has the destruction of superconducting behavior and the transition to the normal state (Figure 1.4).

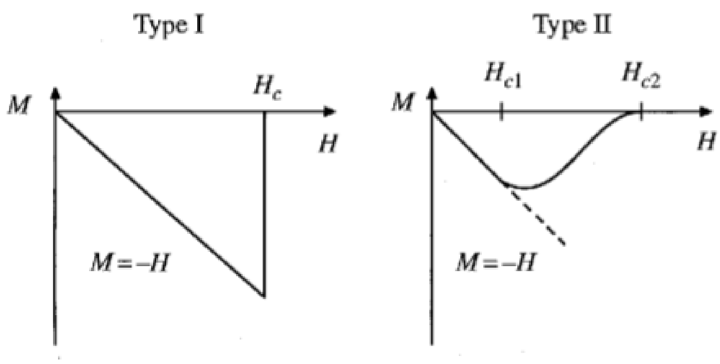

Figure 1.4: Magnetization as a function of the magnetic field H in the two different types of superconductors [3].

The particular behavior of Type II superconductors when the applied field is between H_{c1} and H_{c2} is due to the formation of an intermediate mixed phase, the Shubnikov phase, characterized by the presence of vortices, or fluxons, of quantized flux $\Phi_0 = h/2e$, called Abrikosov vortices. Each vortex consists of a region in which a supercurrent circulates around a normal-conducting core of a few nanometers in radius through which the lines of flux of the external magnetic field enter. These vortices repel each other due to the circulating currents and arrange themselves into a hexagonal lattice, known as the Abrikosov lattice, which allows the superconductor to maintain its properties until the field exceeds H_{c2} (Figure 1.5).

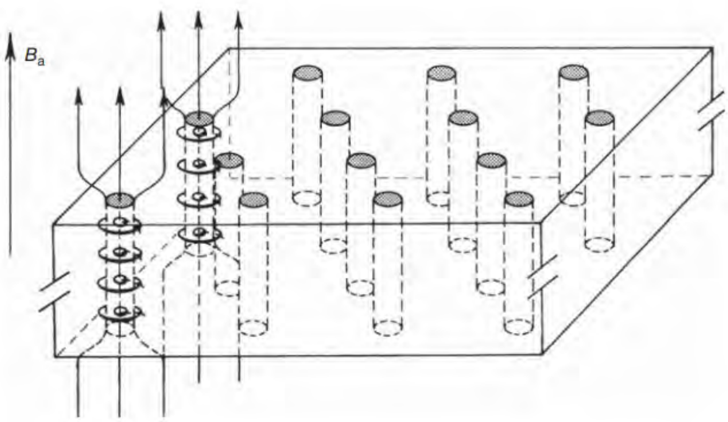

Figure 1.5: Schematic representation of the Shubnikov phase and the Abrikosov vortices [7].

The penetration depth λ and the coherence length ξ are two fundamental parameters that describe the spatial extent of the supercurrents and the size of the vortex core, respectively. The ratio

$$\kappa = \frac{\lambda}{\xi} \tag{1.5}$$

known as the Ginzburg–Landau parameter, determines the type of superconductivity:

- if $\kappa < \frac{1}{\sqrt{2}}$, the material is a Type I superconductor;
- if $\kappa > \frac{1}{\sqrt{2}}$, it is a Type II superconductor.

For both types of superconductors, the values of critical field depend on temperature and go to zero when the critical temperature T_c is reached (Figure 1.6).

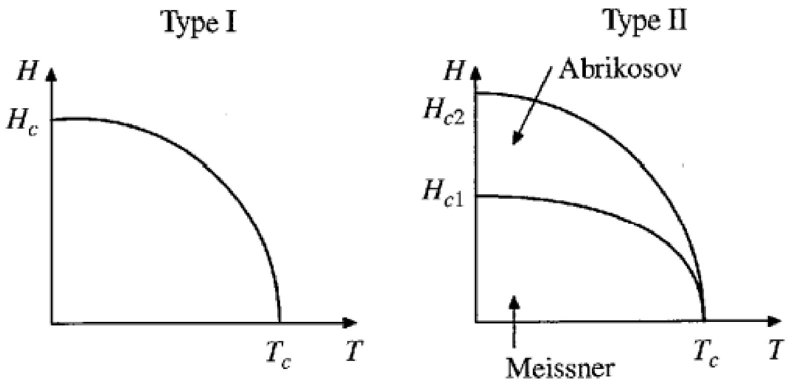

Figure 1.6: H–T diagram for Type I and Type II superconductors [3].

1.1.2 Critical current density and critical surface

The explanation of the superconducting phenomenon is due in particular to J.Bardeen, L.N.Cooper, and J.R.Schrieffer who in 1957 formulated a theory that provides a microscopic explanation of the behavior of superconductors; the theory takes the name BCS from the initials of their surnames. The BCS theory is based on the existence of attractive interactions, mediated by phonons, between the electrons near the Fermi level that lead to the formation of pairs of electrons, called Cooper pairs. They thus represent the charge carriers. Being bosons condensed into one state, the pairs move, when subjected to electric and/or magnetic fields, without friction and coherently; the electrical resistance of the material is therefore null. There is, however, a limit to this behavior. There exists, in the excitation spectrum of the superconductor, an energy gap 2Δ corresponding to the energy required to break a Cooper pair into two single electrons. When this energy is reached a pair breaks, causing a perturbation of the system and, consequently, the collapse of superconductivity. The energy 2Δ can be reached, for example, because of the passage of a current. Therefore, a critical current density can be defined J_c for which the transition to the normal conducting state occurs. This is certainly true for Type I superconductors, whereas in Type II superconductors the phenomenon is more complex. When, in fact, a current flows through the superconductor, Lorentz forces are produced that act on the vortices, causing them to move. The vortices, by moving, produce heat; therefore, the temperature of the material increases up to the transition to the normal state. This phenomenon, in so-called "hard" superconductors, is limited thanks to flux pinning: the vortices are anchored in potential wells constituted by lattice defects, such as impurities, defects, and grain boundaries. The critical current density could therefore be defined as the value of current density at which the Lorentz force exceeds the pinning force, causing depinning of the vortices and the onset of the degradation of superconductivity. However, depinning also occurs at lower currents due to thermal activation (flux creep) and, consequently, with increasing current a continuous increase in resistivity is observed, which is described by the power law:

$$\rho = \rho_c \left(\frac{J}{J_c} \right)^n \tag{1.6}$$

where J_c is the critical current density and n is a value that depends on the pinning energy and, in superconducting wires, on the state of degradation of the filaments (deformations, fractures, etc.). Since the transition is continuous, the critical current is operationally defined according to criteria that can be based on either the resistivity ($\rho_c = 10^{-14}\,\Omega \cdot \mathrm{m}$) or the potential difference per unit length.

It is also important to note that the interaction between fluxons cannot be ignored. An increase in their density, for example due to a more intense external magnetic field, makes the pinning state less stable by increasing the repulsive forces between the vortices. This weakening of the pinning reduces the effectiveness with which the vortices are retained, causing a decrease in the critical current density. Therefore, J_c is not a constant value, but rather varies as a function of temperature and the intensity of the applied magnetic field. A three-dimensional critical surface is used to fully describe the operating limits of a superconducting material, whose axes represent temperature (T_c), magnetic field (B_c), and current density (J_c). This surface defines the region within which the material retains its superconducting properties. (Figure 1.7).

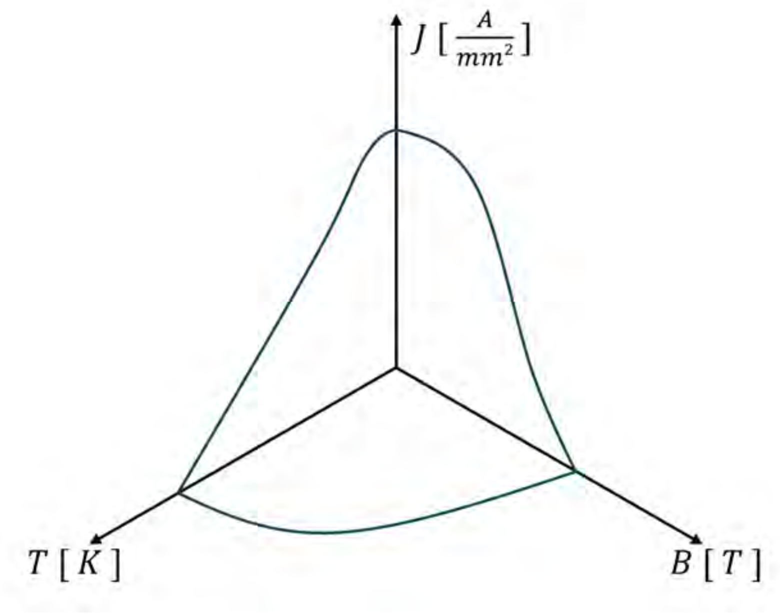

Figure 1.7: Qualitative representation of a generic critical surface.

The critical temperature, the critical magnetic field, and the critical current density are, therefore, very important parameters also from an engineering point of view because they make it possible to determine up to what point a material can exhibit superconducting behavior. It should be kept in mind that, unlike the critical temperature and the critical field, the critical current density depends strongly on the history of the material, i.e., on the mechanical deformations and on the heat treatments undergone.

1.2 Superconducting Wires

Superconductors used in practical applications, such as magnets and power cables, are not employed as pure bulk materials but as multifilamentary composites, in which fine superconducting filaments of a few μm are embedded in a high conductivity metallic matrix. In fact, a bulk hard superconductor exposed to a transverse magnetic field stores magnetic energy through screening currents. Even a minor disturbance can raise the local temperature, reduce the critical current density, and trigger a flux jump, that is, a sudden penetration of magnetic flux which may lead to a complete transition to the normal state, known as quench. At cryogenic temperatures, the volumetric specific heat is extremely low, so even a small energy input can cause a full flux jump. To mitigate this risk, the filament diameter must be reduced: smaller filaments store less magnetic energy and are therefore more stable. The maximum allowable filament size can be estimated from the adiabatic stability criterion:

$$a \leq \frac{1}{J_c}\sqrt{\frac{3\,\rho\,C\,(T-T_c)}{\mu_0}} \tag{1.7}$$

where a is the maximum stable filament radius, J_c the critical current density, ρ the material density, C the specific heat, T_c the critical temperature, T the temperature, and μ_0 the magnetic permeability of vacuum.

Clearly, it is not possible to use a single filament because the current carried would be limited, which is why a large number of filaments are arranged within a metal matrix. The matrix plays multiple roles: it enables current redistribution in the case of local discontinuities, dissipates heat generated by disturbances, and provides dynamic stabilization. In addition, during a quench, the matrix can temporarily carry the transport current, protecting the conductor from irreversible damage. However, the presence of many parallel filaments would introduce electromagnetic coupling problems. In a varying magnetic field, the composite would behave almost like a single large filament, with significant induced coupling currents that cause flux jumps. To mitigate this effect, the filaments are twisted helically around the wire axis. The twist pitch cannot be arbitrarily short due to mechanical constraints, so some residual coupling remains.

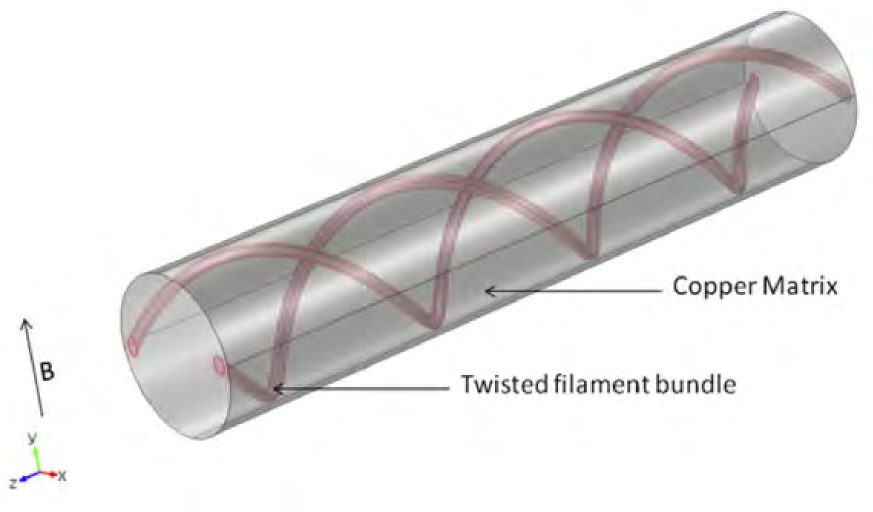

Figure 1.8: Twisting of superconducting filament bundle in a copper matrix [9].

1.2.1 Self-field effects

Although its effectiveness in uniform fields and partially in varying fields, twisting is not effective with respect to the self-field. When a superconducting wire carries current, it generates its own magnetic field, called the self-field. This field is concentrated near the surface of the conductor and adds to any externally applied magnetic field. The combined field determines the local operating point relative to the critical surface, so the presence of the self-field effectively reduces the margin between operating conditions and the critical limits of the material. In high-current multifilament conductors, the self-field can be large enough to approach or exceed the lower critical field locally, promoting flux penetration and increasing the risk of flux jumps. The amplitude of the self-field is proportional to the carrying current and inversely proportional to the radius of the conductor, approximately as $B = \frac{\mu_0 I}{2\pi a}$. Therefore, one solution to mitigate this effect is to use very thin filaments, provided that this does not significantly affect the critical current density. In addtion, other several strategies are employed, such as adopting multifilament designs to distribute the current and reduce field concentration, and optimising the cable geometry by twisting or transposing it. To ensure stable performance, it is also important to select superconducting materials with a weaker dependence of J_c on magnetic field, and to operate with sufficient margin below the critical limits.

1.2.2 AC losses

These solutions not only limit the self-field but also play a decisive role in reducing alternating current (AC) losses, which occur when the conductor is exposed to time-varying magnetic fields or currents. AC losses represent an intrinsic limitation for superconducting wires and are typically divided into three components: hysteresis losses in the superconducting filaments, coupling losses between filaments through the metallic matrix, and eddy current losses in the stabilizer. Hysteresis losses increase with filament size and with the amplitude of the magnetic field variation, making fine filaments essential for low-loss designs. Coupling losses depend on the transverse resistivity of the matrix and the twist pitch, and can be characterized by a time constant that governs the decay of coupling currents; reducing this time constant through shorter twist pitches and resistive barriers is a common approach. Eddy current losses, which occur in the stabilizer and other metallic components, increase with the square of the rate of change of the magnetic field and the electrical conductivity of the material. Therefore, the same design principles, fine filaments, effective transposition, and optimized matrix resistivity, are critical for both self-field control and AC loss minimization. This dual optimization is fundamental for achieving high-performance superconducting wires.

1.2.3 Practical parameters

In the context of superconductor wires, it is necessary to introduce a set of technical parameters that describe the wire in its entirety, including not only the superconducting material itself, but also the stabilizing matrix.

The first parameter defined is the critical current density, referred only to the area occupied by the superconducting filaments A_{SC}. It is obtained by normalizing the critical current with respect to the superconducting area:

$$J_c^{SC} = \frac{I_c}{A_{\mathrm{SC}}} \tag{1.8}$$

and it allows to isolate the contribution of the region that is actually superconducting, providing a parameter that is sensitive to the intrinsic properties of the material. For clarity, it is important to note that in copper-stabilized conductors one also defines the non-Cu critical current density, where the current is normalized to the total non-Cu area rather than to A_{SC}. Alongside J_c^{SC}, the engineering current density is defined as:

$$J_e = \frac{I_c}{A_{\mathrm{tot}}} \tag{1.9}$$

which accounts for the entire cross-section of the wire, including the stabilizing matrix. Since the total area also contains non-superconducting material, J_e is inevitably lower than J_c^{SC}. The relative amount of non-superconducting material, which determines this difference, can be directly expressed through the ratio between the non-superconducting area A_{NC} and the superconducting area A_{SC}:

$$\frac{A_{\mathrm{NC}}}{A_{\mathrm{SC}}} \tag{1.10}$$

This ratio, commonly referred to as the Cu/non-Cu ratio in copper-stabilized wires such as Nb_3Sn wires, is a key design parameter as it determines the balance between the wire's ability to carry current and its thermal stability. A larger matrix fraction increases the wire's ability to dissipate heat and redistribute current during local disturbances, thereby reducing the likelihood of quenches. Conversely, a smaller matrix fraction increases the superconducting area, leading to higher critical current and current density but offering less protection against thermal runaway. Therefore, the optimal NC/SC ratio is the result of a trade-off: sufficient matrix is required to ensure stability against disturbances and protection in the event of a quench, but excessive matrix limits performance by reducing the effective superconducting fraction.

In addition to these geometric aspects, there is the quality of the stabilizing metallic material, quantified by the Residual Resistivity Ratio (RRR), defined as:

$$\text{RRR} = \frac{\rho(300\ \text{K})}{\rho(T_{\text{low}})} \tag{1.11}$$

This ratio indicates the purity of the matrix and its residual resistivity at low temperatures. As the resistivity of metals decreases with temperature and is dominated by the effects of impurities and lattice defects close to absolute zero, high RRR values correspond to better electrical and thermal conductivity. This promotes more effective heat dissipation and rapid current sharing between the matrix and filaments during local disturbances, thereby contributing to the stability of the conductor.

1.3 Practical Superconducting Materials

From a materials perspective, superconductors can be either pure elements, alloys or compounds. However, most elemental superconductors (e.g., Pb, Hg) are type I and unsuitable for high-field applications because of their low critical magnetic fields and limited current-carrying capacity. In contrast, type II superconductors can sustain magnetic flux penetration and operate under much higher magnetic fields. For example, niobium (Nb) and its alloys and compounds exhibits the characteristics of a type II superconductor and can therefore tolerate relatively high magnetic fields. That is why they have been extensively investigated as candidate materials for high-energy physics magnets. Cold-drawn niobium cables represented the first step toward wires capable of carrying large currents. In 1954, the Nb_3Sn compound was discovered to achieve very high magnetic fields, but its widespread adoption was delayed due to brittleness and the difficulty of producing thin wires.

The development of practical superconductors began in the 1960s with the first usable wires based on Nb-Zr and later Nb-Ti. Nb-Ti, discovered in 1961, became the key material for superconducting magnet technology thanks to its ductility, ease of fabrication, and reliable performance. It was widely used in accelerator magnets; however, Nb-Ti is limited to fields below 10 T, even when cooled to 1.9 K, and cannot meet the requirements of next-generation high-energy physics experiments. To overcome this limitation, attention shifted to Nb_3Sn, which offers a higher critical temperature 18 K and an upper critical field exceeding 25 T, despite its brittleness and strain sensitivity.

In the late 1980s, a new family of ceramic high-temperature superconductors (HTS) was discovered. These materials can operate above 77 K and exhibit upper critical fields exceeding 100 T, enabling cooling with liquid nitrogen, a simpler and more economical alternative to liquid helium. However, HTS materials face challenges related to mechanical strain, quench protection, and cost.

In 2001, the discovery of superconductivity in magnesium diboride (MgB_2) introduced a new class of materials. With a critical temperature of 39 K, MgB_2 bridges the gap between low-temperature superconductors (LTS) and HTS. It is a conventional type II superconductor with simple chemistry and low raw material costs. Although it is not able to carry current at high field due to its low irreversibility field, MgB_2 is being explored for applications where moderate fields and higher operating temperatures are acceptable.

The evolution of superconducting materials has been driven by the need to balance performance, manufacturability, and cost, enabling their integration into increasingly demanding technologies. Today, superconductors play a crucial role in applications requiring high current densities, strong magnetic fields, and minimal energy losses. Key applications include accelerator magnets for beam steering and focusing, MRI systems for medical imaging, NMR spectrometres, and fusion reactors for plasma confinement under extreme magnetic fields. In the energy sector, superconductors are being developed for power transmission cables, fault current limiters, and compact transformers, offering improved efficiency and reduced losses. Rotating machinery such as motors and generators benefits from their high torque density and compact design. Beyond power and magnet systems, superconductors are essential in scientific instrumentation and emerging quantum technologies, where zero resistance and coherence are critical. As fabrication techniques advance and cryogenic systems become more accessible, superconductors are expected to expand into broader industrial, medical, and energy applications.

Table 1.1: Practical Superconductors: Properties and Applications

Material	$\mathbf{T_c}$ **[K]**	$\mathbf{B_{c2}}$ **[T]**	**Mechanical Properties**	**Applications**
Nb-Ti	9.2	$\sim$10	Excellent ductility, tolerates heavy plastic deformation	Accelerator magnets (LHC), MRI, NMR
Nb_3Sn	18	>25	Brittle, strain-sensitive; wind-and-react	High-field magnets, fusion, NMR
HTS	77–135	>100	Extremely brittle; best perfomances only in thin tapes	Ultra-high-field magnets, power devices
MgB_2	39	15–20	Moderately brittle	MRI, solenoids, cables

1.3.1 Nb_3Sn

Nb_3Sn is a type-II superconductor with a critical temperature of 18 K and is an intermetallic compound adopting the A15 crystal structure. The stoichiometry of this class is A_3B, where B-type atoms occupy the cube corners and center, while A-type atoms reside on the cube faces. A distinctive feature of the structure is that A atoms form linear, mutually orthogonal chains running parallel to the crystallographic axes (Fig. 1.9).

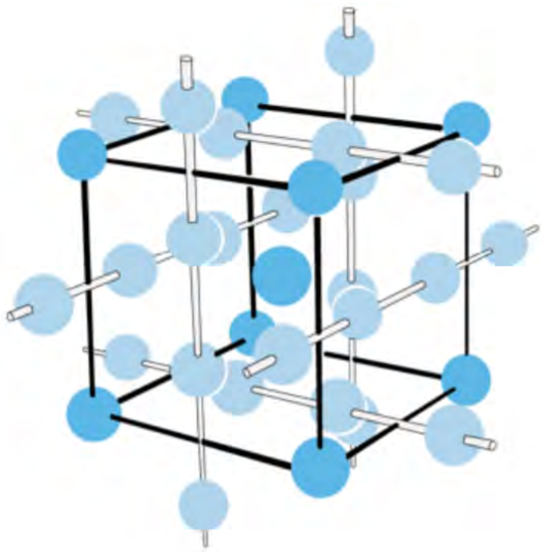

Figure 1.9: A15 crystallographic structure. [10]

This structure is an example of a topologically close-packed (tcp) arrangement, resulting from the packing of polyhedra of various sizes to accommodate atoms of different radii. Intermetallic phases with this structure are known as Frank-Kaspar phases [11].

Many intermetallics of this class exhibit excellent superconducting properties and, as in other type II superconductors, their critical current density depends on the phase microstructure.

Specifically for Nb_3Sn, the critical current density J_c in high magnetic fields is inversely proportional to the average grain size. To maximize grain-boundary area and enhance flux pinning, Nb_3Sn can be doped or synthesized via solid-state reaction at relatively low temperatures (550–700 °C) [11].

The tin concentration in Nb_3Sn affects the stability of the A15 phase and also the superconducting properties. In particular, the critical temperature and the upper critical field vary almost linearly with the atomic percentage of Sn. Around 24 at.% Sn, the critical temperature saturates at 18 K and the upper critical field reaches a maximum before decreasing rapidly, because of a transition from the cubic to the tetragonal phase. To avoid this transformation, small additions of titanium or tantalum, stabilizing the cubic phase, can be introduced. In this way, an upper critical field of about 30 T and a critical temperature of 18 K can be achieved. [12].

Another important feature of Nb_3Sn is the strong influence of mechanical deformation on its transport properties, particularly the critical current. Large deformations can cause severe and irreversible damage by inducing cracks and fractures in the very brittle A15 phase. More moderate deformations can still modify superconducting properties by introducing lattice instabilities that lead to tetragonal distortion and affect electron-electron interactions; in this case the damage can be reversible (Fig. 1.10) [13].

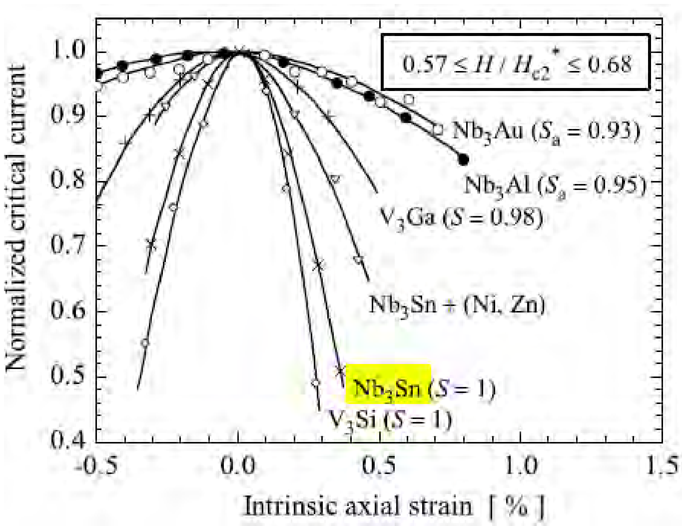

Figure 1.10: Critical current sensitivity to deformation for type A15 superconductors with different degrees of disorder (highlighting Nb3Sn) [12].

Thanks to its high critical temperature and upper critical field, Nb_3Sn has established itself as a key material for high-field superconducting applications, enabling operation in magnetic fields well beyond the limits of Nb-Ti. These properties are indispensable for accelerator magnets, fusion reactors, and other demanding technologies. However, Nb_3Sn's brittleness and sensitivity to mechanical strain present significant challenges during wire and cable fabrication. Precise control of deformation and heat treatment is necessary to prevent irreversible damage. Despite these limitations, Nb_3Sn continues to evolve through advances in alloying, microstructural optimization, and innovative wire architectures. These developments aim to enhance Nb_3Sn's current-carrying capacity and mechanical robustness, ensuring it remains a cornerstone of next-generation high-energy physics and energy applications.

1.3.1.1 Wire production technologies

At present, Nb_3Sn wire production is based on assembling copper, tin, and niobium into billets that are subsequently extruded and/or cold-drawn to achieve the target diameter. The resulting wires consist of fine filaments embedded in a copper matrix, separated by diffusion barriers (Nb or Ta), and containing precursors (mainly Cu, Nb, and Sn) arranged in a regular pattern. The intermetallic compound is formed afterwards through a solid-state reaction at about 700 °C.

Industrial production predominantly employs three routes: *bronze route*, *internal tin (IT)*, and *powder-in-tube (PIT)*.

Bronze route. Nb filaments are embedded in a Sn-rich bronze matrix, usually wrapped by a diffusion barrier (Ta, Nb, or V) and enclosed in high-purity copper; the billet is then extruded and drawn 1.11.

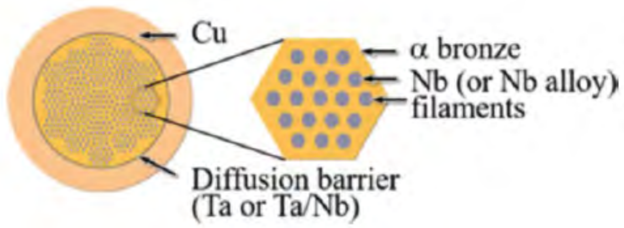

Figure 1.11: Schematic diagram of an Nb_3Sn wire obtained using the bronze route technique before the heat treatment [14].

The main limitation is the effective amount of Sn available to react with Nb, constrained by solubility in bronze (9.1 at.% Sn) and incomplete utilization during reaction. This leads to a significant fraction of non-stoichiometric Nb-Sn compound, which is not superconducting at high fields. The small volume fraction of Sn-rich Nb_3Sn, combined with the fact that a portion of the wire is occupied by bronze, results in a relatively low non-Cu critical current density ($J_c \approx 1000\,\mathrm{A/mm^2}$ at 4.2 K and 12 T) [15].

Internal tin (IT). Nb or Nb-alloy filaments are assembled around a core of pure Sn (or Sn alloy) within a copper matrix, surrounded by a diffusion barrier, and enclosed in pure copper; the billet is extruded and drawn 1.12.

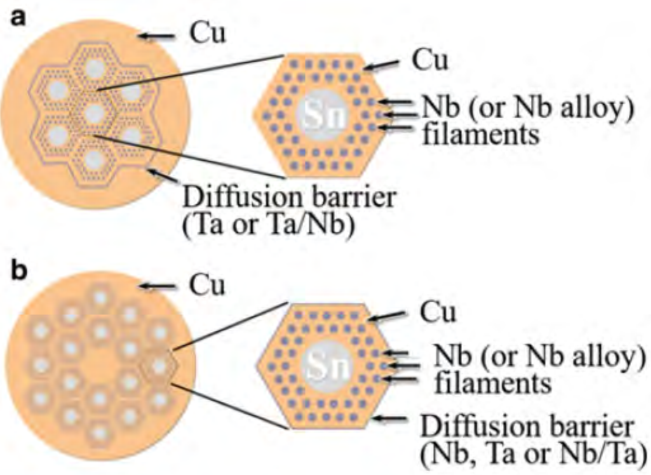

Figure 1.12: Schematic diagram of an Nb_3Sn wire obtained using the internal tin technique before the heat treatment [14].

The presence of a tin core eliminates the solubility limitation inherent to bronze-route conductors and allows near-stoichiometric Nb_3Sn. By optimizing the tin quantity, adding alloying elements (Ti or Ta), controlling grain size, and tailoring the wire architecture, high non-Cu J_c values are achieved. For example, for wires produced via the Restacked Rod Process (RRP®), J_c is $\approx 3000\,\mathrm{A/mm^2}$ at 4.2 K and 12 T.

Powder-in-tube (PIT). Nb tubes are filled with fine $NbSn_2$ powder inside a high-purity copper matrix. The composite is extruded, drawn, and heat-treated to form Nb_3Sn (Fig. 1.13).

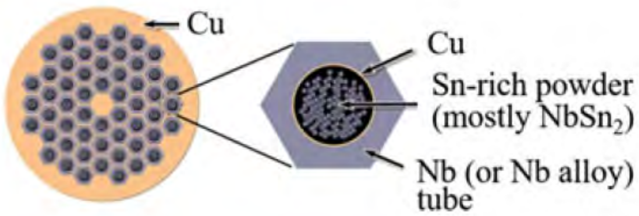

Figure 1.13: Schematic diagram of an Nb_3Sn wire obtained using the powder-in-tube technique before the heat treatment [14].

Through optimized layouts, high-quality powders, and Ta alloying inside the Nb tubes, PIT wires can reach non-Cu $J_c \approx 2500\,\mathrm{A/mm^2}$ at 4.2 K and 12 T.

Transport properties differ among these wire types because the microstructure and microchemistry of Nb_3Sn are strongly influenced by the fabrication route and by the sequence of phases formed during heat treatment [16]. Furthermore, the degradation of transport properties caused by mechanical deformation during cable and magnet fabrication depends on wire architecture [17]. For these reasons, understanding the specific properties of each wire type is essential to select the most suitable conductor for a given application.

1.3.2 MgB_2

Magnesium diboride (MgB_2) is a binary intermetallic compound that gained attention in 2001, when Akimitsu and colleagues reported its superconductivity at 39 K [18]. The relatively high critical temperature, combined with its simple chemical composition and crystal structure, makes MgB_2 a unique material that bridges the gap between conventional low-temperature superconductors and the more complex high-T_c cuprates [19]. In addition, its ease of synthesis and favorable transport properties, quickly positioned it as a promising candidate for both electronic and large-scale applications [5].

MgB_2 crystallizes in the AlB_2-type hexagonal lattice, where boron atoms form graphite-like honeycomb layers and magnesium atoms occupy the interstitial sites between them (1.14). The boron layers are primarily responsible for the superconducting behavior, hosting the σ and π electronic bands that give rise to the material's distinctive two-gap superconductivity. [5]

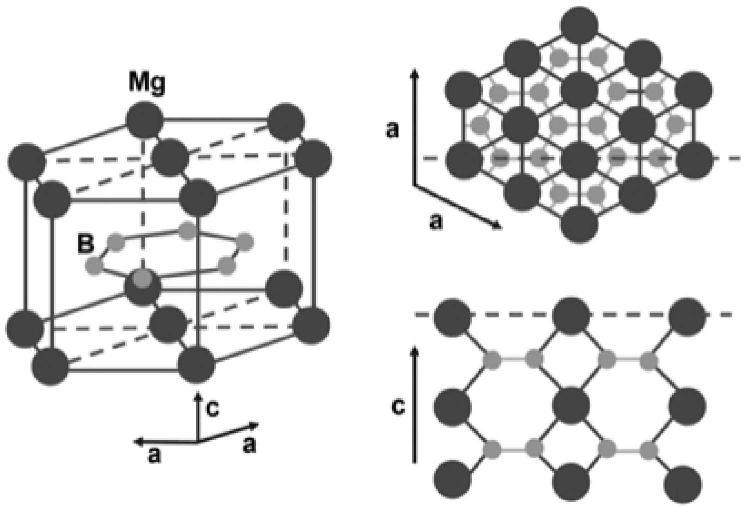

Figure 1.14: AlB_2-type structure of magnesium diboride. [5]

The layered configuration leads to strong anisotropy in bonding and compressibility, with the c-axis being significantly more compressible than the a-axis, and in the superconducting properties. The upper critical field H_{c2} is highly anisotropic and highly sensitive to doping and disorder: while clean single crystals may exhibit H_{c2} values of

3-4 T perpendicular to the boron planes, in thin films doped with oxygen or carbon values exceeding 40 T have been reported [19], [20], [21].

MgB_2 exhibits high critical current densities (J_c), particularly in thin films and well-connected polycrystalline samples. In optimized films, J_c can exceed 10^5A/mm^2 at 4.2 K in self-field, while wires and tapes fabricated via the powder-in-tube (PIT) method routinely achieve J_c values of above 10^3A/mm^2 in self-field. Importantly, unlike HTS, MgB_2 does not suffer from weak-link behavior at grain boundaries, allowing efficient current transport even in non-epitaxial polycrystalline forms. This property is crucial for large-scale applications, where mechanical flexibility and ease of fabrication are essential [19], [21].

MgB_2's compatibility with cryogenic systems operating above liquid helium temperatures adds to its appeal. Its performance at 20–25 K makes it suitable for cooling with liquid hydrogen or cryocoolers, which are more economical and practical for certain applications. This has enabled its use in open MRI systems, fault current limiters, rotating machinery, and power transmission cables. Despite its many advantages, MgB_2 does have limitations. It is sensitive to moisture and oxidation, and its superconducting properties can degrade if not properly protected. However, this issue is much less significant in practical forms, such as wires. Moreover, its critical temperature remains below that of cuprates. Nevertheless, ongoing research into doping strategies, such as the introduction of carbon, silicon carbide, or aluminum, and microstructural optimization continues to improve its performance and expand its potential.

1.3.2.1 Wire production technologies

The fabrication of MgB_2 wires has evolved significantly since the early 2000s, with both academic and industrial efforts contributing to the development of reliable, scalable, and high-performance conductors. Today, the most widely adopted method is the powder-in-tube (PIT) technique, which exists in two main variants: in-situ and ex-situ. Another technique is the IMD (Internal Mg diffusion).

Ex-situ powder-in-tube. The ex-situ method uses pre-reacted MgB_2 powder inserted into a metallic tube, typically a Nb barrier surrounded by a Ni, Cu-Ni or Monel sheath (Fig. 1.15). The composite is mechanically deformed through drawing and rolling, then subjected to a short high-temperature recrystallization heat treatment at $900° - 1000°C$. This route ensures excellent homogeneity and industrial scalability, producing kilometer-length wires with consistent properties. Typical ex-situ wires exhibit $J_c \approx 3000\,\text{A/mm}^2$ at 4.2 K and 3 T, and $J_c \approx 400\,\text{A/mm}^2$ at 4.2 K and 7 T.

Although their high-field performance is lower than that of other routes, ex-situ wires remain the preferred choice for large-scale applications requiring uniformity [22].

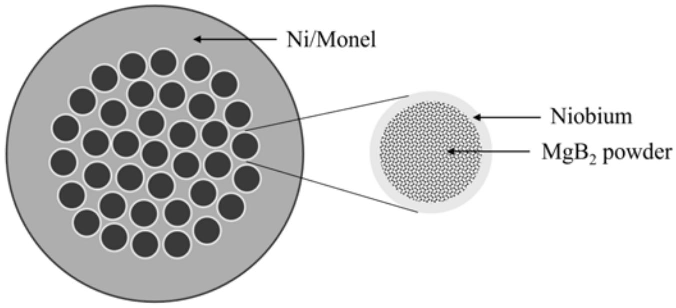

Figure 1.15: Schematic diagram of a MgB_2 wire obtained using the ex-situ powder-in-tube technique before the heat treatment.

In-situ powder-in-tube. Elemental magnesium and boron powders, ground to improve homogeneity, are mixed in a stoichiometric ratio (typically 1:2), and packed into the metallic tubes. The composite is then mechanically deformed through rolling or drawing to achieve the desired wire geometry (Fig. 1.16). A final heat treatment, typically at temperatures between $650°C$ and $750°C$, initiates the solid-state reaction that forms the MgB_2 superconducting phase, directly within the tube core. This method allows carbon doping during synthesis, improving high-field performance. Advanced in-situ wires using nano-sized boron and optimized carbon additions have achieved $J_c \approx 100\,\mathrm{A/mm^2}$ at 4.2 K and 13 T, outperforming ex-situ wires in high-field regimes [22].

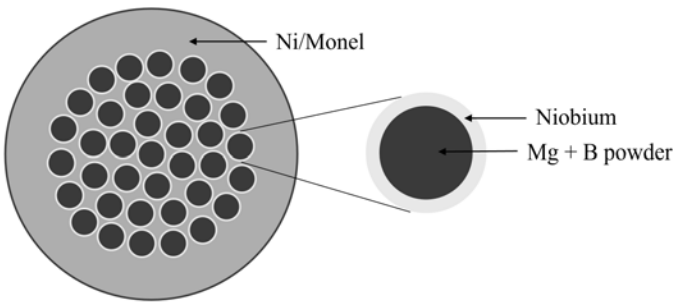

Figure 1.16: Schematic diagram of a MgB_2 wire obtained using the in-situ powder-in-tube technique before the heat treatment.

Internal Magnesium Diffusion (IMD). A pure Mg rod is placed at the centre of a Ta or Nb tube, and the hollow space between the metal sheath inner wall and the Mg rod is filled with boron (B) and carbon (C), with the carbon present either as a thin carbon layer on the surface of the B particles or as polycyclic aromatic hydrocarbons, such as anthracene $C_{14}H_{12}$, powders (Fig. 1.17). During heat treatment at $\approx 640°C$, Mg diffuses into B, forming dense MgB_2 layers (>90% theoretical density). This process yields superior J_c values, exceeding $\approx 1000\,A/mm^2$ at 4.2 K and 10 T, and up to $\approx 3000\,A/mm^2$ at 20 K and 4 T. IMD wires are particularly promising for high-current applications [22], although the extreme fragility remains a significant issue.

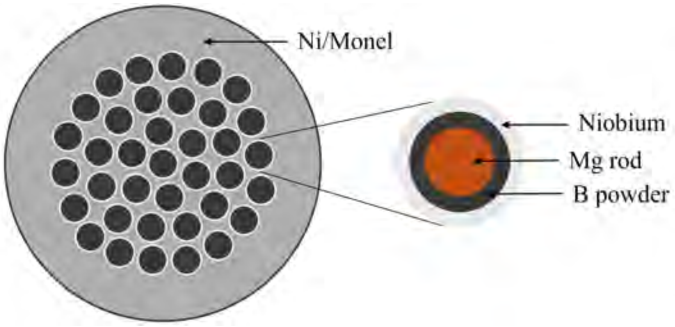

Figure 1.17: Schematic diagram of a MgB_2 wire obtained using the IMD technique before the heat treatment.

The choice between ex-situ, in-situ, and IMD routes significantly affects the microstructure, connectivity, and doping level of MgB_2, which determine its critical current density and high-field performance. Understanding these relationships is essential for tailoring conductors for specific applications, such as MRI systems and power transmission cables, where operating temperature, mechanical flexibility, and cost constraints play a decisive role.

1.4 Performance Limits: Load-Line and Operating Conditions

Superconducting wires are used to wind superconducting magnets; therefore, their performance must be evaluated also in the context of the operating conditions imposed by magnet design. To define the operational limits and safety margins of the magnet, one of the most widely used tools is the load-line, which graphically represents the evolution of the magnetic field at the conductor location as a function of the transport current, based on the specific geometry and configuration of the magnet. When superimposed on the critical surface of the superconductor—typically expressed in the (B, J) plane at a fixed temperature—the load-line allows for a direct assessment of the maximum allowable operating point. To ensure stable operation and avoid premature quenching, the magnet must operate below this threshold, and appropriate margins must be defined, typically along the load-line. These margins are typically quantified in term of current as the percentage difference between the operating current density J_{op} and the critical current density J_Q, that would cause a quench at the operating temperature T_{op}. Alternatively, the same margins can be obtained using the magnetic field:

$$M[\%] = (1 - \frac{J_Q}{J_{op}}) \times 100 = 1 - \frac{B_Q}{B_{op}} \times 100 \quad (1.12)$$

where B_{op} is the peak magnetic field at the operating point, and B_Q the corresponding quench limits at the operating temperature. Typical field margins for accelerator magnets range between 15% and 30%, in order to maximize the performance of the collider without compromising stability.

Margins can also be expressed in terms of temperature as:

$$M_T[K] = T_Q - T_{op} \quad (1.13)$$

where T_Q is the temperature at which the conductor reaches its critical surface under the given field and current, and T_{op} is the actual operating temperature. In this case, the margin indicates the thermal robustness of the superconducting state.

Understanding the load-line thus provides a crucial link between the intrinsic properties of the wire and its practical performance in magnet applications, guiding both conductor development and magnet design.

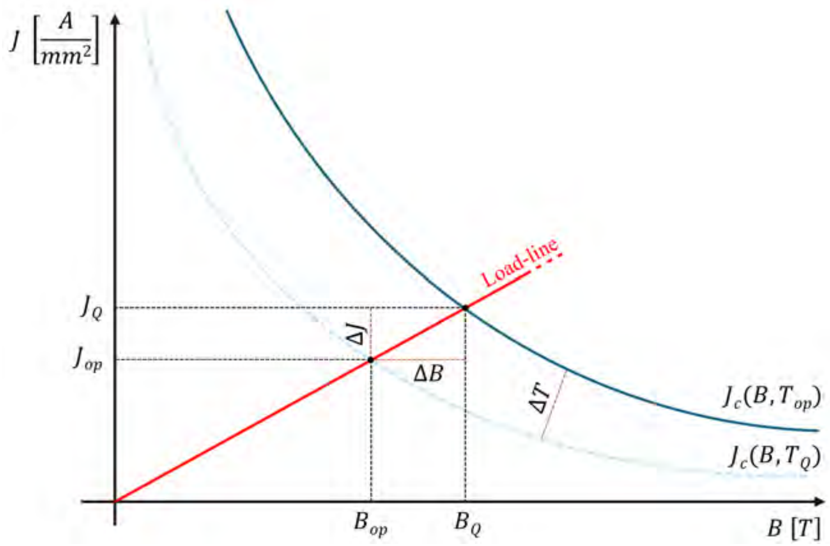

Figure 1.18: Qualitative plot of a load line of a superconducting magnet together with the $J_c(B)$ curves a the operating temperature T_{op} and at the quench temperature T_Q.

Chapter 2

Technical superconductors cables

Numerous applications involving high-field or high-current density necessitate conductors with fully transposed current paths to guarantee low AC-losses and uniform current density. In areas such as accelerator magnets, fusion magnets, high-current transport cables, transformers, and motors, various multi-strand cable designs are employed.

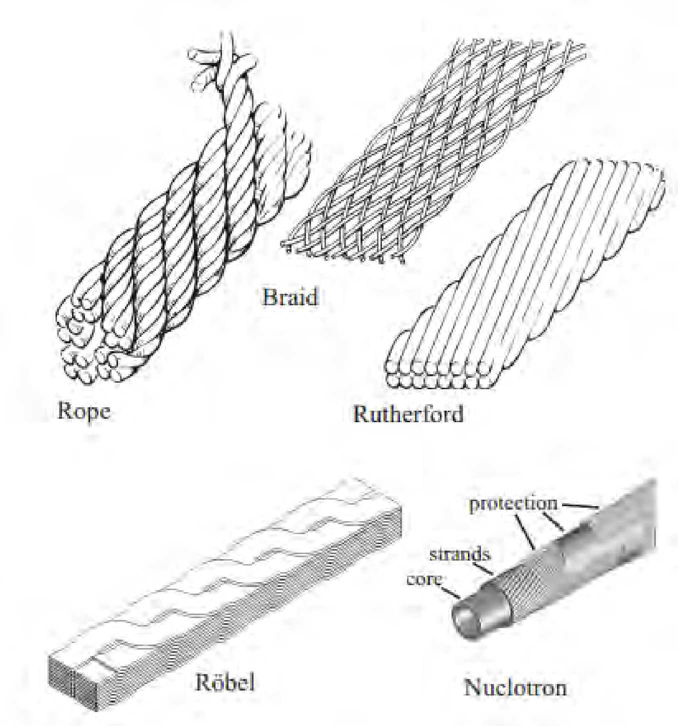

Figure 2.1: Examples of different types of superconducting cables [23].

2.1 Cables for magnets

Superconducting cables for accelerator magnets must be able to carry very high currents in strong magnetic fields, while ensuring thermal stability and mechanical robustness. In order to meet these demanding conditions, they must exhibit very low AC losses and be able to withstand the high Lorentz forces that develop during magnet operation. For this reason, accelerator magnets use multi-strand superconducting cables. This architecture serves multiple purposes: it reduces the number of turns in the coil windings, thereby lowering the magnet's overall inductance, and it limits coupling currents between strands, minimizing AC losses. In addition, the cable design facilitates a uniform current distribution, helping to maintain the required field quality. Over the past decades, cable architectures have evolved to meet increasingly demanding requirements, leading to designs such as Rutherford cables, cable-in-conduit conductors (CICC), and advanced HTS tape-based concepts (Roebel and CORC®).

2.1.1 Rutherford cables

Rutherford cable is the most widely used type of conductor in superconducting magnets for particle accelerators, thanks to its excellent mechanical, electrical, and thermal properties. Introduced in the 1970s, it is now used in both Nb-Ti-based and Nb_3Sn-based magnets. Its flat and compact geometry allows for high current density and good stability, reducing AC losses and improving magnetic field distribution. The cable consists of dozens of multifilament wires arranged in two layers and transposed along the cable axis (Fig. 2.2). Transposition is crucial to minimize coupling currents and ensure uniform current distribution between the wires. After twisting, the wire bundle is compacted by lamination, resulting in a rectangular or slightly trapezoidal cross-section, ideal for use in accelerator magnet coils. The flat shape maximizes the filling factor and reduces field inhomogeneities, improving field quality [24].

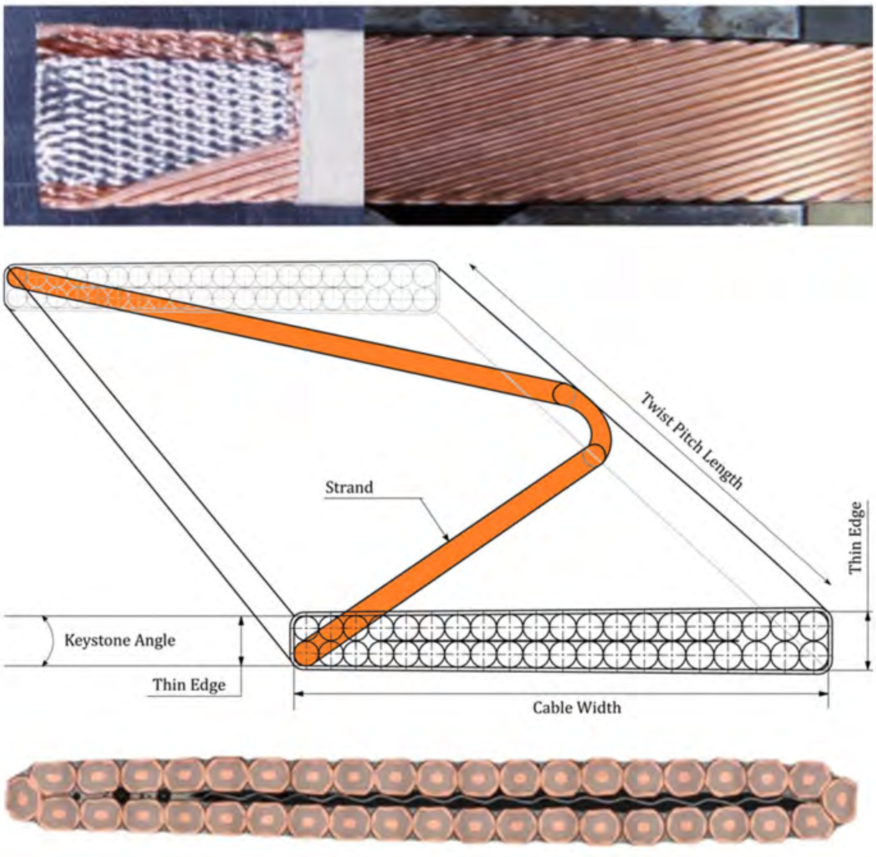

Figure 2.2: Structure of a superconducting Rutherford cable.

The critical current limit of the cable is given by the sum of the critical currents of the individual wires, reduced by degradation phenomena during cabling due to plastic deformation and possible damage to the sub-elements, especially in the case of Nb_3Sn, a fragile material that is sensitive to mechanical stress [13], [25].

A critical aspect is the management of variable regime losses, which depend on the contact resistance between the wires. To reduce coupling currents between different layers, it is necessary to increase the inter-layer contact resistance without compromising the ability to share current between adjacent wires. The most effective solution is to insert a thin resistive core (typically stainless steel) in the center of the cable, which increases the resistance between the two layers (R_c) and reduces AC losses, while keeping the contact between adjacent wires (R_a) low [26], [27]. In addition, wires are often coated with chromium, which resists high-temperature heat treatment cycles and helps to increase R_c without compromising surface conductivity [27].

From a geometric point of view, the cable has fundamental parameters such as transposition angle, compaction factor, and keystone angle. The transposition angle influences both mechanical stability and field distribution: typical values vary between 9° and 16°, with lower limits causing instability and upper limits generating defects such as sharp edges and strand popping [28]. Optimal design requires a compromise between compactness, mechanical integrity, and electromagnetic performance. For Nb_3Sn, Rutherford technology required significant attention. The fragility of the material imposes stringent constraints on the wiring process and heat treatment. Excessive deformation of the sub-elements during compaction can cause diffusion barrier breaks and merging of the sub-elements, resulting in an increase in effective diameter (d_{eff}) and worsening stability at low fields [13], [29], [30]. For this reason, modern Nb_3Sn wire architectures (RRP® and PIT) are designed to better withstand wiring stresses, and compaction procedures are carefully controlled to limit plastic deformation [25].

2.2 Superconducting Power Cables

The massive integration of renewable energy sources required by the European Green Deal calls for a radical rethinking of current transmission grids [31], [32]. This infrastructural renewal process is driven by European Union targets for CO_2 emission reduction and enhanced energy efficiency in transmission systems [33]. In this context, superconducting cables can represent an innovative solution to overcome the limitations of conventional electrical transmission systems, particularly in high-density urban areas and networks where the demand for energy is growing [34]–[37]. In traditional copper or aluminum conductors, resistive losses increase with the square of the current, causing significant heat dissipation, insulation aging, and the necessity for very large cross-sections or extreme voltages to increase transport capacity [34], [35], [38], [39]. Superconducting materials, conversely, allow the transport of enormous amounts of energy with almost zero dissipation in direct current (DC) regimes, provided they operate below the critical temperature and within the limits of the critical surface [35], [38]. Therefore, it is no longer necessary to elevate the voltage to extreme levels to increase capacity, but the current can be significantly increased, reducing the size of the infrastructure [3], [36], [40], [41].

The discovery of high-temperature superconductors (HTS), such as Bi-2223 and REBCO, has made it possible to operate at 77 K using liquid nitrogen, an inexpensive, safe, and readily available fluid [35]. Most recently, the discovery of the superconducting properties of magnesium diboride (MgB_2) introduced a highly significant alternative. Produced industrially from widely available raw materials, MgB_2 allows for a cost reduction of up to tenfold compared to HTS. Unlike HTS, MgB_2 is primarily manufactured as multifilamentary wires with a circular cross-section. This morphology provides superior mechanical versatility, making it ideal for torsion stresses, handling and industrial cabling techniques, as demonstrated by the kilometre-scale production for CERN's Superconducting Links [22], [42], [43].

A superconducting cable consists of several layers: superconducting tapes or wires wound around a core, high-voltage insulation impregnated with liquid cryogen, and a cryostat that reduces heat loss thanks to a vacuum and multi-layer superinsulation. Flexible cryostats with corrugated steel tubes are the most common. Examples of cable layouts are shown in Fig. 2.3. The terminations and junctions are critical components that manage the transition between cryogenic and room temperatures by minimising heat ingress. The cooling system uses pressurized liquid nitrogen or helium or hydrogen, with high-efficiency pumps and cryogenic refrigerators [35].

Figure 2.3: Possible layouts for superconducting power cables [44].

These cables offer several notable advantages, including high current capacity in a compact geometry, losses one order of magnitude lower than conventional cables, and trench sizes reduced by more than half. Furthermore, there are no thermal impacts or electromagnetic interference, allowing installation in confined urban spaces or near sensitive equipment. Projects such as the AmpaCity installation in Essen, theSuperRail project in Paris, and the Superconducting Links at CERN have confirmed the technical feasibility and economic potential, showing that superconducting cables can replace high-voltage infrastructure with medium-voltage solutions, reducing costs and freeing up valuable space [45]–[49]. However, the high cost of conductors, the complexity of cryogenic systems and the requirement for operational experience to be accumulated remain challenges. Advances in manufacturing and cooling technology, coupled with growing energy demand and urban constraints, are paving the way for superconducting cables to become a key component of future smart grids and HVDC supergrids. Their ability to carry enormous amounts of power with minimal losses and reduced footprint makes them an ideal solution for renewable energy integration, and special applications such as data centers, industrial plants, and electric ships.

2.2.1 MgB_2 power cables

Superconducting cable technology based on MgB_2 is currently one of the most promising solutions to address the challenges of the energy transition. MgB_2 combines good electrical properties with an operating temperature compatible with cryogenic systems using gaseous helium or liquid hydrogen. Recent advances have led to robust, flexible multifilament wires suitable for compact, mechanically stable cables that withstand torsion and bending during installation [50], [51].

From a construction point of view, a MgB_2 cable consists of a central conductor formed by several superconducting wires arranged helically together with copper strands or around a copper core. This type of configuration ensures mechanical stability and uniform current distribution. The copper also protects the cable against faults that can cause the transitions of the superconductor to the normal state [52]. An electrical insulation system made of lapped materials, such as polyimide or PPLP, is applied around the conductor. These materials are chosen for their ability to maintain mechanical and dielectric properties at cryogenic temperatures. The insulation is designed to be impregnated with cryogenic fluid without compromising dielectric strength and is complemented by a grounded electrical shield and external mechanical protection. The entire assembly is enclosed in a flexible cryostat with high vacuum and layers of thermal superinsulation to minimize heat loss. In hybrid systems, the cryostat also serves as a conduit for liquid hydrogen, simultaneously enabling cooling and chemical energy transport [53], [41], [54].

Initial studies confirmed the feasibility of integrating superconducting cables into a cryogenic infrastructure for liquid hydrogen transport, paving the way for combined electricity and energy carrier distribution [55], [56]. These tests demonstrated the ability to maintain stable thermal conditions and ensure electrical insulation in severe environments, thus validating hybrid lines combining two forms of energy in a single system. Further projects have shown the capability to implement high-power DC connections with MgB_2 cables, verifying dielectric strength, thermal stability, and compatibility with network requirements [57], [58]. These efforts have driven the development of optimized conductor architectures, advanced insulation systems, and low-loss cryostats.

Today, research focuses on two main areas: lines cooled with gaseous helium for high-current, medium-voltage terrestrial applications, and MVDC systems cooled with liquid hydrogen for simultaneous electricity and hydrogen distribution. Large-scale demonstrators are under construction, featuring compact cables, improved insulation, and protection strategies to handle faults and transients without compromising superconducting stability [59], [60], [61]. Simulations and type tests assess performance under real conditions, including ripple phenomena, power reversals, and mechanical stresses [37], [38], [62].

Experimental demonstrations and ongoing large-scale projects confirm that MgB_2 technology can support high-power DC transmission and hybrid systems integrating electricity and hydrogen transport. These achievements mark the transition from proof-of-concept to pre-commercial deployment. Nevertheless, critical issues remain, including cost optimization, standardization of components, and integration with existing grids.

Chapter 3

Finite Element Methodology

First introduced in 1943 by R. Courant [63], Finite Element Analysis (FEA) or Fem Element Method (FEM) is a numerical method based on the discretization of continuous domains for solving partial differential equations that govern complex physical phenomena. The fundamental principle consists in replacing the continuous problem with a discrete system, obtained by dividing the domain into finite sub-regions, called elements, connected by nodes. The variables of interest within each element, such as displacements, stresses, or temperatures, are approximated by shape functions that are defined to ensure continuity between elements and stability of the solution. This transforms the original problem into a system of linear or nonlinear algebraic equations that can be solved using robust numerical methods. The accuracy of the solution depends on the quality of the discretization and the order of the shape functions [64], [65].

The finite element method process begins with the idealization of the problem, which means simplifying the physical system into a mathematical model while retaining its essential characteristics. Next comes discretization, which consists of generating the mesh by dividing the domain into finite elements. The type of element chosen depends on the geometry and phenomenon being analyzed (Fig. 3.3). Each element is characterized by its number of dimensions, degrees of freedom, material properties, and number of nodes. Nodes are the points that define an element's geometry and correspond to the locations at which values of the relevant physical quantities are calculated. Boundary and initial conditions are also imposed during this stage. The quality of the discretization process directly impacts the accuracy and numerical stability of the model. Therefore, it is essential to use a mesh that ensures that the solution converges within acceptable error limits while balancing precision and computational efficiency. Adaptive mesh refinement techniques can be employed to optimize this trade-off [66]

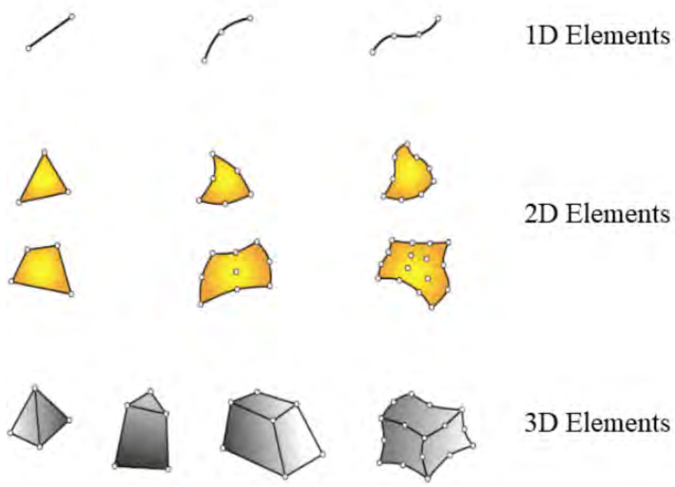

Figure 3.1: Examples of element types. The white dots are the nodes.

The mathematical formulation of the problem results in the creation of a stiffness matrix and the assembly of a global system. This system is then solved using direct or iterative methods. A crucial step is the verification of convergence, in which the result must stabilize as the density of the mesh (h-convergence) or the order of the elements (p-convergence) increases [64]. After obtaining the numerical solution, it is good practice to vary some parameters to test the robustness of the model. Specifically, the solution should improve as the discretization increases and exhibit reasonable sensitivity to variations in material properties or boundary conditions. If this does not occur, it indicates an incorrect formulation of the problem.

Model validation is equally important because the idealization and discretization processes inevitably introduce numerical errors through simplifications. Therefore, it is necessary to verify that these errors are within pre-established tolerance limits. According to international guidelines (ASME), two steps are required: numerical verification and physical validation. Numerical verification ensures the mathematical correctness of the formulation and its implementation. This includes checking that the governing equations have been properly discretized and solved, that the numerical algorithms are stable, and that the solution converges as the mesh is refined or the element order increases. Physical validation, on the other hand, determines whether the model accurately represents the real-world phenomenon under study. This involves comparing simulation results with experimental data, performing a critical analysis of discrepancies, and, whenever possible,conducting a direct comparison with measurements. If significant differences arise, the model must be refined. This may involve reformulating the idealization, modifying the boundary or initial conditions, or improving the mesh. Without this phase, there is a risk of obtaining solutions that are numerically correct but physically meaningless.

There is a wide range of commercial software solutions available for implementing finite element models. ANSYS, COMSOL, and Opera are among the most widely used in research and industry due to their versatility and advanced capabilities.

3.1 Ansys

ANSYS is one of the most widely used and versatile software programs for finite element method (FEM) simulations. It is a platform that offers advanced tools for structural, thermal, fluid dynamics, and electromagnetic analysis. Thanks to its ability to handle complex models and provide accurate results, ANSYS is now a benchmark in industrial and academic settings. ANSYS is available in two main versions: Ansys Workbench, which has a graphical user interface (GUI) and is designed to simplify model creation and simulation management; and Ansys Mechanical APDL (Ansys Parametric Design Language), which is command language-based and allows for more detailed and flexible control.

APDL is a scripting language derived from Fortran that enables direct communication with the ANSYS solver via text commands. Within the software environment, users can enter individual commands or create macros containing sequences of commands to be executed in batch mode. This approach is particularly advantageous for parametric analyzes and optimizations because it automates processes, reduces calculation times, and allows quick modification of variables and conditions. APDL provides full control over the simulation workflow. Users can specify material properties, geometry, mesh details, interaction between components, and all necessary conditions. APDL also supports defining loads and electrical currents, as well as commands for processing and visualizing results after analysis.

ANSYS supports 1D, 2D, and 3D simulations, ensuring high flexibility when modeling complex phenomena. Its combination of computational power and automation makes ANSYS an ideal tool for parametric analysis and optimization processes, where rapid modification and efficient variable management are essential to reduce development time and costs. [67]

3.1.1 2D Simulation Options

Two-dimensional simulations are a crucial aspect of engineering analysis. They offer a powerful methodology that can drastically reduce processing time and conserve computational resources when the effects of the third dimension are negligible or can be accurately represented by simplifying assumptions. In the mechanical modeling of solid structures, a 2D approach generally provides three main analysis options: plane stress, plane strain, and generalized plane strain. An additional option, axisymmetric geometry, is essential for cases with rotational symmetry [65]. Understanding the precise applicability and underlying assumptions of each formulation is critical to ensuring the scientific validity of the simulation results.

The plane stress formulation is suitable for structures where the z dimension is considerably less than the x and y dimensions. This option assumes zero stress and non-zero strain in the out-of-plane direction (z). Also the out-of-plane stress components must be zero across the entire section [68]:

$$\sigma_z = \sigma_{xz} = \sigma_{yz} = 0$$

Zero longitudinal stress (σ_z) allows for free elongation in the z direction. When using this option, a thickness field is available to specify the model's thickness. Typical applications include flat plates subjected to in-plane loading and thin disks under pressure or centrifugal forces.

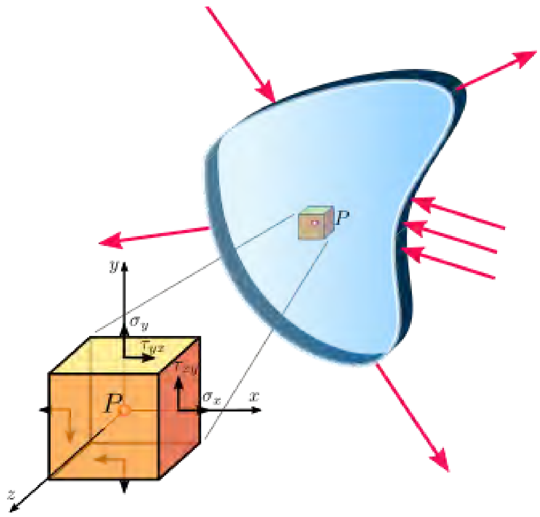

Figure 3.2: Representation of plane stress state in a continuum.

On the other hand, the plane strain formulation is used to model an infinitely long structure in which the material is mechanically constrained orthogonally to the $x - y$ cross-section plane. The main assumption in this model is that strain along the z-axis is zero [68]:

$$\epsilon_z = \epsilon_{xz} = \epsilon_{yz} = 0$$

The stress in the z-direction (σ_z) is non-zero, but it is induced by the constraint and contributes to equilibrium. Since out-of-plane strain is zero, no reduction in cross-section occurs, indicating the preservation of volume within the constraint. This option is appropriate for structures in which the z dimension is much larger than the x and y dimensions, such as long bodies with constant cross sections. It is essential to understand that the typical plane strain behavior cannot be applied in thermal analyses, whether steady-state or transient.

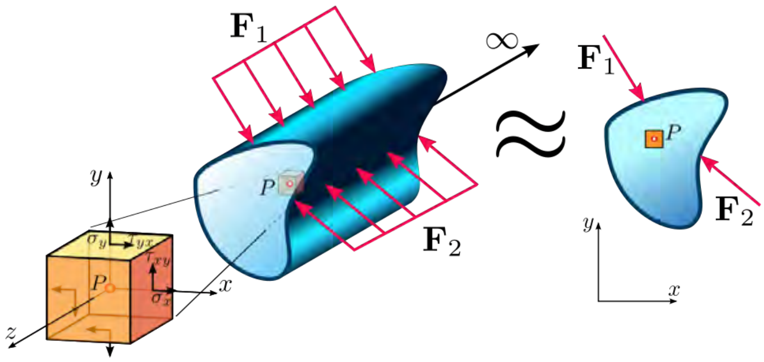

Figure 3.3: Representation of plane strain state in a continuum.

The generalized plane strain option assumes a finite deformation domain length in the z-direction, unlike the standard Plane Strain which assumes infinite length. This approach provides more practical results for deformation problems in which a z-dimension exists but is not dominant. It allows for the two-dimensional representation of a "fiber" in which all cross sections deform identically along its length ($\epsilon_z =$ constant), but with a non-zero, uniform axial strain:

$$\epsilon_z = \text{constant} \neq 0, \quad \epsilon_{xz} = 0, \quad \epsilon_{yz} = 0$$

By allowing for the application of longitudinal strain, generalized plane strain accurately accounts for section reduction during deformation, a phenomenon that standard plane strain cannot capture. To use this option, additional properties must be specified, such as the fiber length and the rotations of the end planes about the x and y axes.

Finally, the axisymmetric formulation assumes that a three-dimensional model and its loading can be generated by revolving a two-dimensional section 360° about the y-axis. The key requirement is rotational symmetry in geometry, material properties, and loading. The axis of symmetry must coincide with the global y-axis, and the geometry must lie on the positive x-axis of the $x-y$ plane. In this representation, the y-direction is axial, the x-direction is radial, and the z-direction corresponds to the circumferential (hoop) direction. Although the hoop displacement is zero, the formulation naturally includes the effects of hoop strains (ϵ_θ) and stresses (σ_θ), which are typically significant in maintaining radial equilibrium in the circular structure.

3.2 Elasto-plastic behaviour representation

In non-linear analyses, the bilinear stress-strain curve is used as a simplified approximation of the material's response under monotonic loads. While it does not correspond to the actual experimental behaviour, it replaces it with two linear sections, defined by the parameters E, σ_y and H, in order to provide an essential description of the elasto-plastic transition. (Fig. 3.4).

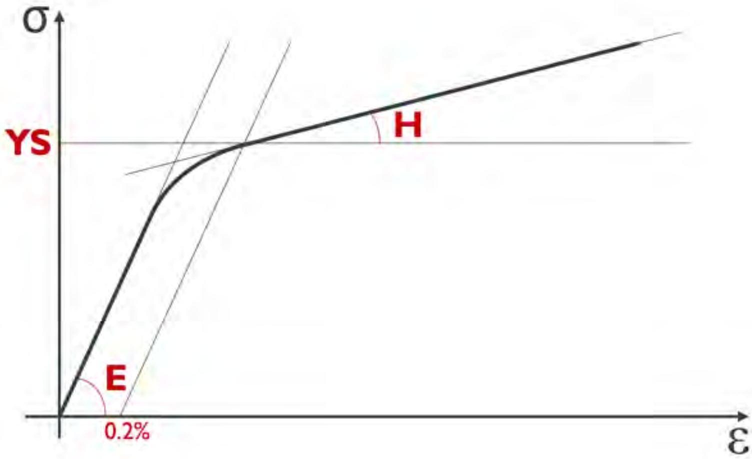

Figure 3.4: Example of a stress-strain curve with the parameters needed for the bilinear model.

The initial response of the material is purely elastic and is governed by Young's modulus E, which defines the stiffness for small increments of strain. This phase continues until the yield stress σ_y is reached; beyond this point, the deformation is no longer fully reversible. Once yielding occurs, the material enters a plastic regime that is represented by a second linear segment with a reduced slope, defined by the tangent modulus H. This description provides a simplified representation of the behaviour of the material beyond yielding, capturing the initial evolution of plastic deformation. The idealised elastic–plastic behaviour is commonly referred to as isotropic hardening. The term reflects the assumption that, once yielding begins, the material's resistance to further deformation increases uniformly, without introducing directional effects. The bilinear approximation thus offers a concise yet effective representation of the transition from elastic to plastic behaviour, while ensuring a numerically stable formulation that is straightforward to implement in computational models. Its structure is particularly compact: only three experimentally measurable parameters (the elastic modulus, the initial yield stress, and the tangent modulus) are required to reproduce the material response in both the elastic and plastic regions.

Chapter 4

Nb_3Sn wire model

Current particle accelerator magnets predominantly use Nb-Ti technology. However, the next generation of accelerators will require dipole magnets that can generate magnetic fields of up to 14 T. [69]. This represents a significant leap beyond the capabilities of Nb-Ti, establishing Nb_3Sn as the most promising candidate for future high-field applications. Nb_3Sn offers substantially higher upper critical fields and critical temperatures than Nb-Ti, enabling operation in regimes where Nb-Ti would far exceed its superconducting limits. However, transitioning to Nb_3Sn introduces new challenges in terms of conductor design, fabrication, and mechanical integrity. These challenges must be addressed to ensure reliable magnet performance.

Among the various manufacturing technologies for Nb_3Sn wires, the Restacked Rod Process (RRP) has emerged as the preferred choice for accelerator magnets because it combines high critical current densities J_c with adequate mechanical and magnetic stability [70].

As mentioned in Chapter 2, these wires are assembled into multi-strand Rutherford cables for practical magnet construction to reduce coil inductance and improve current distribution. However, the cabling process can cause severe mechanical deformation of the strands, which may result in the shearing of the unreacted superconducting subelements within the wires [70]. This damage may compromise the integrity of the thin diffusion barriers that separate tin (Sn) from the copper (Cu) stabilizer. The consequences of barrier failure are critical. If Sn penetrates into the Cu stabilizer during the subsequent high-temperature reaction heat treatment, the copper's electrical conductivity is significantly degraded. This contamination lowers the Residual Resistivity Ratio (RRR), a parameter directly linked to the thermal and electrical stability of the magnet. A reduced RRR has been associated with dynamic instabilities and an overall deterioration of magnet performance. This has been demonstrated through magneto-optical imaging and confocal microscopy [71], and has been further confirmed through correlation studies between filament distortion and RRR degradation. [72]. These findings highlight that mechanical damage during cabling affects not only the stabilizer purity, but also the superconducting properties of the strand. In fact, cabling-induced deformation can severely compromise both J_c and RRR in Nb_3Sn wires, making the control of mechanical robustness a critical aspect of conductor design [73]. Therefore, preserving these properties requires minimizing damage during cabling. This demands strand designs that are mechanically robust under deformation. Key parameters such as sub-element spacing, barrier thickness, and internal architecture must be carefully optimized [74]. While full-scale cabling tests demand hundreds of meters of strand and are costly and time-consuming, preliminary evaluations can be performed using flat deformation techniques. Although rolling a strand flat does not perfectly replicate the complex stresses of cabling, previous studies on Nb-Ti [75] and Nb_3Sn [73], [76], [77] have demonstrated a reasonable correlation between filament distortion under flat deformation and actual cabling-induced damage. Therefore, flat rolling is a practical and efficient method for assessing mechanical robustness during early design stages. In this context, finite element (FE) mechanical modeling has become an indispensable tool to complement experimental approaches. FE simulations allow to predict how Nb_3Sn wires will respond to cabling-like stress conditions. These simulations provide insights into strain distribution, barrier integrity, and potential failure points. Several studies have developed and refined these models to optimize wire layout and minimize cabling degradation [74], [78], [79], [80]. These computational tools allow for the systematic optimization of wire architecture prior to large-scale fabrication, thereby reducing development costs and accelerating progress toward high-field magnet technology.

In summary, the shift from Nb-Ti to Nb_3Sn for next-generation accelerator magnets introduces a complex interplay between electromagnetic performance and mechanical resilience. The success of this transition depends not only on achieving high Jc but also on maintaining stabilizer purity and RRR through robust strand design and controlled deformation during cabling. Experimental techniques such as flat rolling, combined with advanced FE modeling, represent powerful strategies for addressing these challenges and ensuring the reliability of future high-field superconducting magnets.

In this context, the Genoa section of INFN is collaborating with CERN to develop a finite element model that simulates the mechanical behavior of superconducting wires during processing. The main objective is to study how deformation induced by the wiring process affects unreacted wires. The focus is on the distribution of stresses and geometric variations that occur during this phase. To this end, two-dimensional models of wire cross-sections have been created. Some of these models have idealized, symmetrical geometries, while others are derived directly from scanning electron microscope (SEM) micrographs of commercial RRP wires. This allows for a comparison between theoretical and real configurations. The goal is to evaluate the differences between these representations and quantify how deformed geometry, stress, and strain correlate with experimental data obtained by analyzing cross-sectional images through numerical simulations.

4.1 The wire

The Nb_3Sn strand used to wind the MQXF quadrupole coils in the High-Luminosity LHC is produced by Oxford Superconducting Technology and cabled into 40-strand Rutherford cables [81]. This wire has a 108/127 restack design, whereby 108 superconducting subelements are arranged within a within a matrix of 127 total available positions. The 19 central positions are occupied by a solid copper core. The conductor has a nominal diameter of (0.850 ± 0.003) mm and a specified Cu/non-Cu ratio in the range 1.10–1.30. Within this Cu/non-Cu range, the corresponding effective sub-element diameter is approximately 55 μm. The 108 sub-elements are arranged on nominally hexagonal arrays, although micrographs, as can be seen in Fig. 4.1, show distortions at the corner positions. The copper spacing between sub-elements is not explicitly specified but is typically around 6.5 μm in this strand design. The MQXF conductor specifications include a non-Cu critical current density $J_c \geq 2450\,\mathrm{A/mm^2}$ at 12 T and 4.2 K, and 1280 $\mathrm{A/mm^2}$ at 15 T, which ensures adequate performance at the peak fields (11–12 T) encountered in MQXF operation [81]. The strand design also satisfies the requirement of residual resistance ratio (RRR) ≥ 150 for thermal stability, and its mechanical performance within Rutherford cabling maintains I_c integrity under transverse stress, confirming its suitability for MQXF coil fabrication [82].

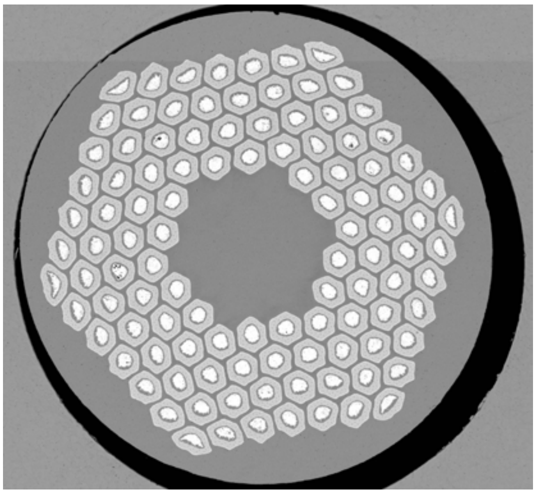

Figure 4.1: SEM micrograph of the RRP 108/127 for MQXF magnets.

4.2 FE models implemented in Ansys APDL

Two distinct models have been developed to represent the conductor structure. The first is based on a simplified geometric construction (Fig. 4.2a), in which the different components of the wire are described by ideal shapes arranged according to the nominal design specifications. The second model, on the other hand, is based on a microstructural representation derived from a micrograph obtained using a scanning electron microscope (SEM) with backscattered electrons (Fig. 4.2b) to capture the true complexity of the composite.

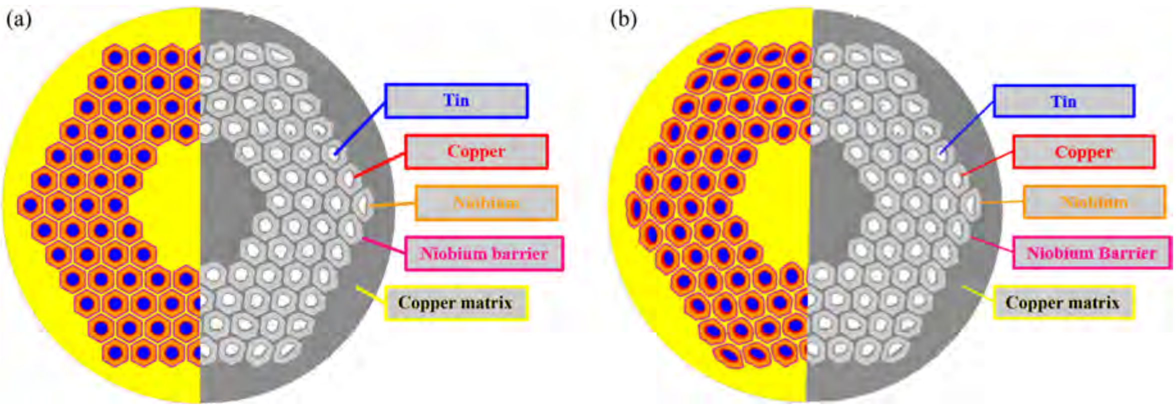

Figure 4.2: (a) Geometrical FE model together with the SEM micrograph of the wire. (b) FE model based on a SEM image together with the SEM micrograph of the wire.

This model was constructed by processing the SEM micrograph using ImageJ software [83] and applying segmentation techniques to identify and isolate the different constituent phases. The image was examined in detail and converted into a suitable format for segmentation. Then, thresholding and region-selection tools were used to distinguish the areas corresponding to the individual phases. This procedure enabled each region to be more clearly defined, ensuring the boundaries between phases were accurately traced and the resulting segmented domains could be cleanly and consistently extracted (Fig. 4.3).

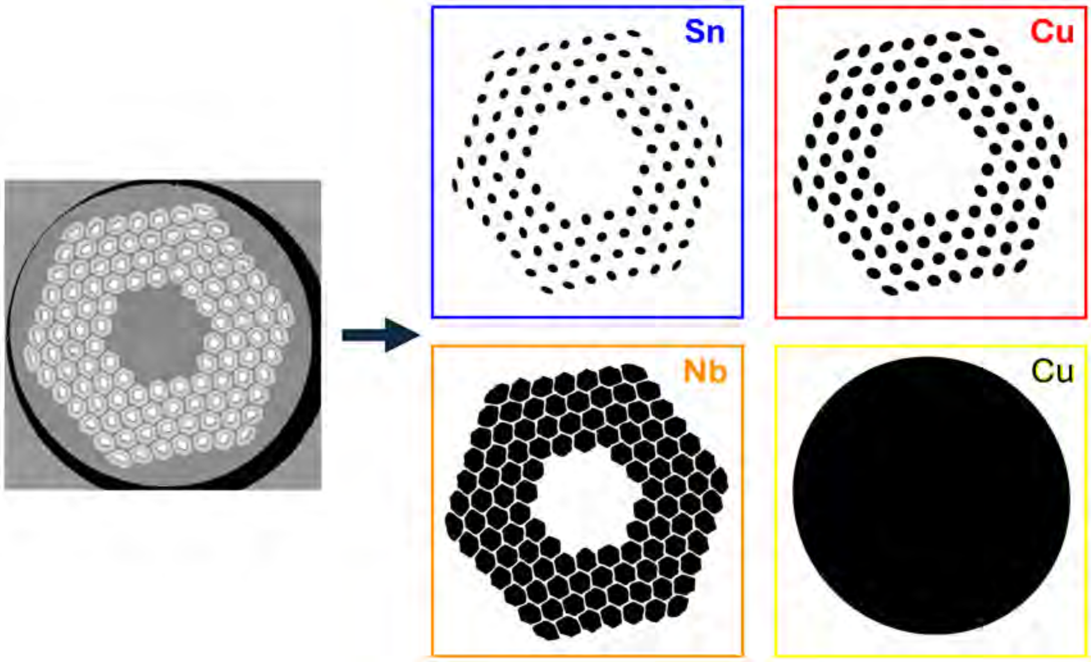

Figure 4.3: Separation of the components from the SEM micrograph using ImageJ.

The segmented regions were then converted into files with the extension ".anf", compatible with ANSYS, and imported for merging and mesh generation (Fig. 4.4). This step enabled the segmented areas to be transferred directly into the finite element environment while preserving their geometry and boundaries. It is important to note that, for the construction of the niobium barrier, the niobium areas were isotropically scaled to facilitate future parametric studies on the influence of barrier thickness. This uniform resizing enables the dimensions of the barrier to be varied in a controlled manner, eliminating the need to repeat the entire segmentation process.

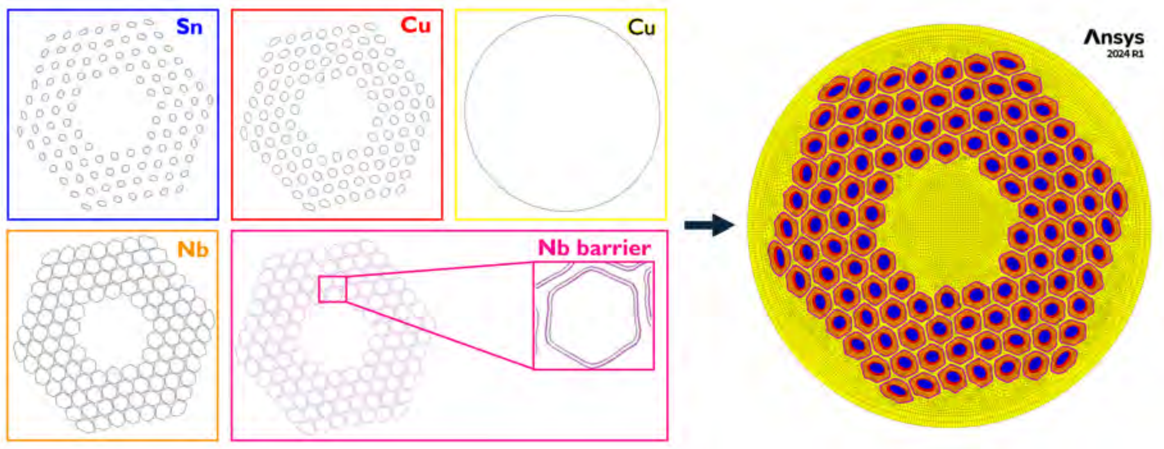

Figure 4.4: Segmented regions and importation into ANSYS.

All models were implemented in ANSYS APDL using the PLANE182 element [67]. This general-purpose 2D solid element is suitable for both linear and non-linear analyses. It performs reliably in simulations involving plasticity and heterogeneous materials, making it well suited for modelling the mechanical behaviour of composite Nb_3Sn wires. Within this framework, bilinear stress–strain curves were adopted as a compact representation of the elasto-plastic material behaviour. As detailed in Chapter 3, this idealisation requires three experimental input parameters: Young's modulus E, the yield strength σ_y, and the tangent modulus H. Poisson's ratio ν, which describes deformation perpendicular to the applied force, is also required to complete the material description. Two sets of material properties were considered. The first set is based on literature data reported by Rochepault et al. [80], derived from experiments conducted within the NED programme [84]. The second set, referred to here as 'Measured Properties' (MP), is obtained at CERN through nanoindentation measurements on the RRP 108/127 wire examined in this study. Including both sets enables an evaluation of the influence of different material assumptions on the predicted mechanical response. Since the tangent modulus H cannot be obtained directly from nanoindentation measurements, and determining it would require additional assumptions or indirect estimation procedures that are not uniquely defined, the values reported in [80] were used for both property sets. This approach ensures consistency with previous studies and avoids introducing further modelling uncertainties. The complete list of material parameters used in the simulations is provided in Table 4.1.

Table 4.1: Mechanical properties

Rochepault et al. [80]	E [GPa]	σ_y [MPa]	H [GPa]	ν
Copper	112	330	7.5	0.364
Nb/Cu filament pack	108	615	4.5	0.38
Tin	44	15	0.07	0.33

Measured at CERN (MP)[a]	E [GPa]	σ_y [MPa]	H [GPa]	ν
Copper	122	360	[80][b]	0.364
Nb/Cu filament pack	124	880	[80][b]	0.38
Tin	[80][b]	[80][b]	[80][b]	0.33

[a] Measured at CERN (MP) means that the properties have been extimated by nanoindentation at CERN specifically for this study.
[b] This values are taken from Rochepault et al. [80].

The rolling process is modelled by placing the wire between two rigid plates. The lower plate is fixed and the upper plate moves downwards along the Y-axis, thereby imposing the desired deformation (Fig. 4.5). This simplified configuration captures the essential mechanics of the laboratory rolling setup used to characterise Nb_3Sn strands. The plates are modelled as perfectly rigid to ensure that the imposed displacement is fully transferred to the wire without introducing artificial compliance into the system. The upper plate moves kinematically, meaning the prescribed downward displacement directly controls compression and ensures numerical stability when reaching the target reduction. The selected level of deformation corresponds to a 15% reduction in wire diameter, representing the standard amount of compressive strain routinely applied at CERN during Nb_3Sn acceptance tests. This value reflects well-established practices aimed at identifying potential defects in the sub-elements, the barrier or the copper stabiliser, while ensuring that deformation remains within the reversible or quasi-reversible range for most components of the strand. Reproducing this specific reduction in the numerical model makes the simulations directly comparable with the experimental procedures used in quality control tests. This enables consistent interpretation of the computed stress and strain fields.

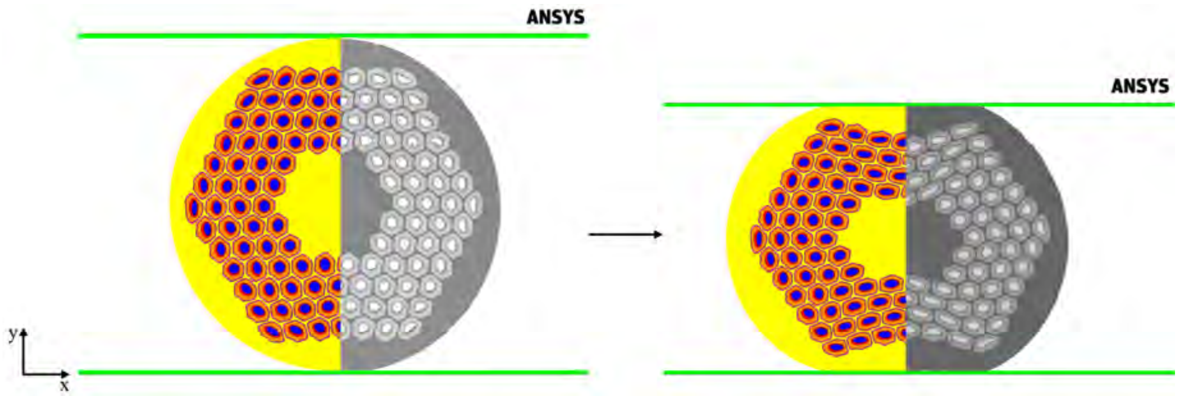

Figure 4.5: Simulated deformation and corresponding SEM micrographs shown side-by-side for visual comparison.

4.3 Validation of the model

To validate the simulation results, a Scanning Electron Microscope (SEM) backscattered electron micrograph of the deformed RRP 108/127 wire (Fig. 4.6a) was used as experimental reference. The analysis focused on the internal tin subelements, which display cross-sections that are approximately elliptical after deformation, as highlighted in Fig. 4.6b. Contours extracted from the SEM image were used to characterise the geometry of the subelements after deformation and to provide a benchmark for comparison with the finite-element predictions.

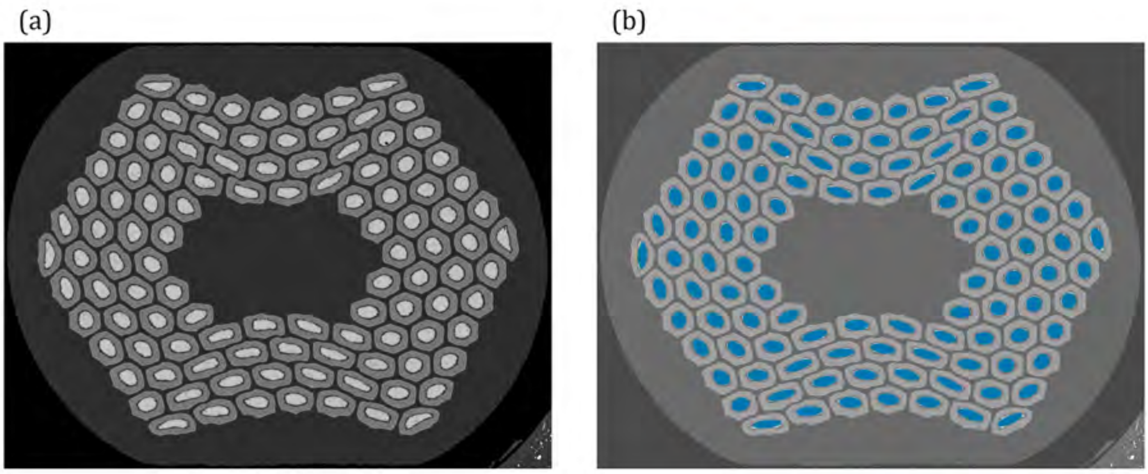

Figure 4.6: SEM micrograph of the 15% deformed 108/127 wire (a) and micrograph with approximate tin ellipses highlighted.

A custom Python script was developed to process the micrograph by automatically detecting the subelements, fitting ellipses to their boundaries, and extracting the relevant geometric parameters, including centroid coordinates, semi-axis lengths, aspect ratio, area, and perimeter. The script also divided the ellipses into a series of angular zones labelled A to L, as shown in Fig. 4.7, allowing for a more detailed spatial comparison between experiment and simulation. The same workflow was applied to the elliptical subelements obtained from the 2D Ansys models using a second script, ensuring methodological consistency between the two datasets.

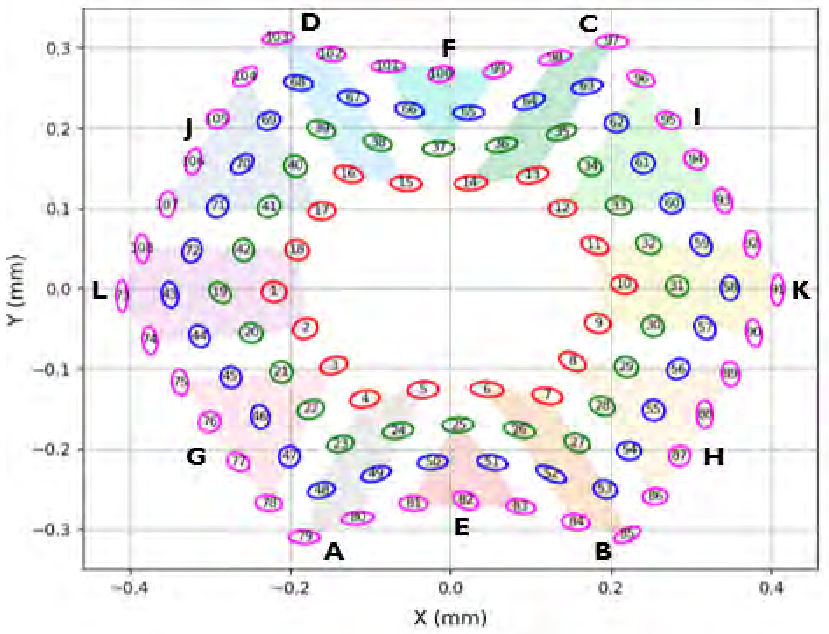

Figure 4.7: Example of a fit of the ellipses divided into zones.

For each corresponding subelement, the relative percentage difference between simulated and experimental parameters was computed according to Eq. (4.1):

$$\%Difference = \left(\frac{Parameter_{model} - Parameter_{real}}{Parameter_{real}} \right) \times 100 \tag{4.1}$$

where *Parameter* denotes any of the geometric properties of the ellipses, such as centroid coordinates, semi-axis lengths, aspect ratio, area, or perimeter. The average percentage difference was then evaluated for each model variant to quantify how accurately the simulations reproduced the deformation behaviour and geometric characteristics of the internal-tin subelements. Results were visualized using scatter plots and summary statistics, with error bars representing the RMS of the percentage differences, allowing systematic trends and discrepancies to be identified across the simulations. This analysis made it possible to determine which 2D modelling strategy achieved the best agreement with the experimental geometry and to assess the sensitivity of the predictions to the underlying material and geometric assumptions.

4.3.1 Selection of the 2D Finite Element formulation

Choosing an appropriate two-dimensional finite element (FE) representation is crucial to obtain a reliable description of the deformation of the wire under transverse loading. Although the analysis focuses exclusively on the cross section, the longitudinal assumption still influences the result, because the axial behaviour is coupled to the transverse deformation. As explained in Chapter 3, among the 2D formulations available in ANSYS, three options are provided: plane stress, plane strain, and generalized plane strain. The generalized plane strain formulation was adopted instead of plane strain to allow for a uniform longitudinal strain. Consequently, the analysis was restricted to a comparison between generalized plane strain and plane stress, which allows for free elongation in the z direction, as these options provide fundamentally different treatments of the longitudinal strain representation. The results clearly show how these modelling assumptions influence the predicted mechanical response of the wire. The plane stress formulation leads to a stronger transverse contraction, which becomes evident when comparing the areas of the tin ellipses calculated by the model with those of the reference case. The average percentage difference associated with plane stress is -9%, indicating that this formulation substantially overestimates the deformation. This behaviour arises from the $\sigma_z = 0$ constraint, which leaves the material unconstrained in the axial direction and amplifies the Poisson-driven in-plane contraction. The generalized plane strain formulation, by introducing a finite but uniform longitudinal strain, limits this effect and provides results much closer to the expected behaviour. In this case, the average percentage difference is only -0.2%, showing that generalized plane strain reproduces the deformation with much higher accuracy and avoids the excessive contraction observed in the plane stress case. Therefore, the generalized plane strain formulation will be adopted for the further analyses.

4.3.2 Comparison between idealised and SEM-derived geometries

An additional evaluation was conducted to determine whether the idealised or SEM-derived geometry provided a more effective representation of the real wire deformation. The comparative results are plotted in Fig. 4.8. The analysis shows that including the actual wire geometry substantially improves the overall accuracy of the study. This is primarily due to the fact that the idealised geometry is based on the assumption that the subelements are perfectly regular hexagons with identical circular cores. However, this simplification fails to capture the structural complexities of the real wire, where both the subelements and their cores are distorted. By contrast, with the geometry derived from the SEM micrograph, it is possible to account for the non-uniform, non-hexagonal shape of the subelements and the elliptical nature of their cores, which exhibit varying degrees of elongation depending on their position within the wire cross-section. This discrepancy between the two modelling approaches is particularly evident in the estimation of the aspect ratio, which is significantly underestimated when regular hexagonal subelements are assumed. Specifically, the model based on the idealised geometry produces an average percentage difference of approximately -13% (Fig. 4.8b), indicating that the simplified hexagonal assumption does not fully capture the geometry of the wire. Conversely, when using the geometry taken from the SEM micrograph, the average percentage difference is reduced to approximately 3% (Fig. 4.8a), showing that including the actual geometry produces a result that more closely aligns with reality. This distinction is important because high local deformation can significantly affect stress concentration and cause barrier damage.

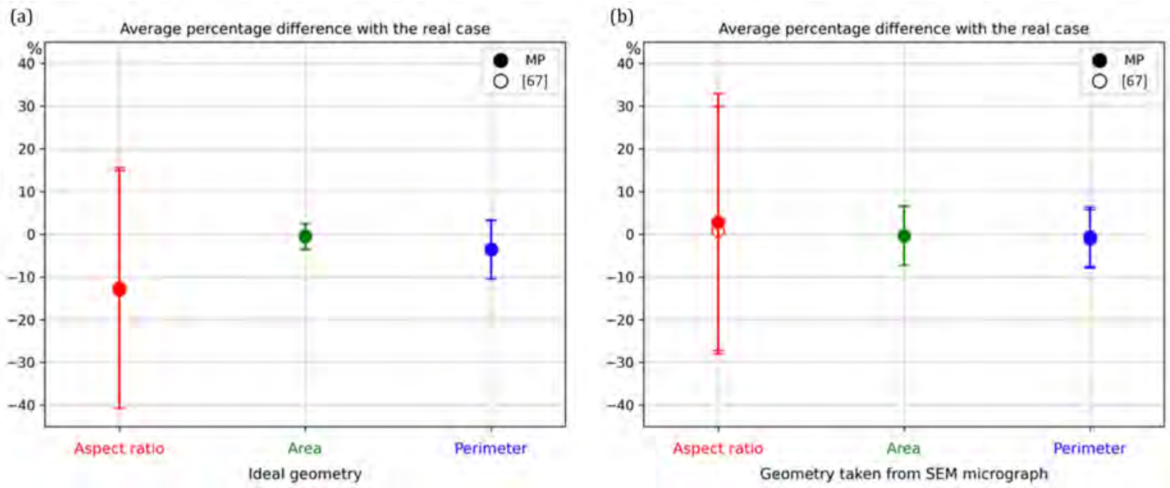

Figure 4.8: Average percentage difference for aspect ratio (red), area (green), and perimeter (blue) between the real wire and (a) the SEM-based model and (b) the ideal geometry model, for both CERN [MP] and Rochepault et al. [80] properties.

This distinction is particularly evident when analysing the shear strain distribution across the wire (Fig. 4.9). The distribution obtained using the SEM-derived geometry (Fig. 4.9a) reveals high local peak strains exceeding $\pm$ 0.28, which are located on the diffusion barriers of a greater number of subelements than those obtained using the idealised geometry (Fig. 4.9b). This phenomenon is concentrated specifically within the two innermost rings of subelements situated closest to the centre of the wire. While the idealised model can reproduce certain fundamental features of the shear strain distribution, such as localisation of strain along 45° bands it may not be suitable for all purposes. Nevertheless, it remains valuable in specific contexts, such as preliminary comparisons between different wire designs. In fact, it is the only viable approach for investigating configurations that have not yet been manufactured, or for which SEM micrographs are unavailable. As real geometrical data cannot be obtained without physical samples, the idealised model provides a means to systematically explore new subelement arrangements and guide the design process prior to production. In this context, it also enables a preliminary assessment of the influence of different architectural choices on the mechanical response. However, the SEM-derived geometry provides results that are more consistent with experimental observations of wire deformation and diffusion barrier leakage. For example, studies on similar wire designs (specifically RRP-R1 and RRP-R2 [72]) have shown that barrier leakage initially occurs within these two innermost rings of subelements during rolling processes. The corner subelements located near the wire periphery are a special case because they have a high initial aspect ratio in the actual wire before rolling. In the idealised geometry model (Fig. 4.9b), these subelements are treated as nearly regular hexagons, leading to a prediction of relatively low shear strain levels. In contrast, the SEM-derived geometry (Fig. 4.9a) incorporates the initial irregular morphology of these peripheral subelements. This results in higher predicted shear strain values. However, these subelements do not exhibit the highest strain concentrations. This observation aligns with previous findings suggesting that barrier damage is concentrated towards the centre of the wire [4]. Although the impact of subelement geometry in round wires has been documented [85], and correlations between RRR and post-rolling aspect ratio distributions have been studied [72], [73], tracing how the initial geometry of individual subelements dictates local strain distributions is more challenging. Using the SEM-derived geometry in this study enables this to be explored more directly in future work.

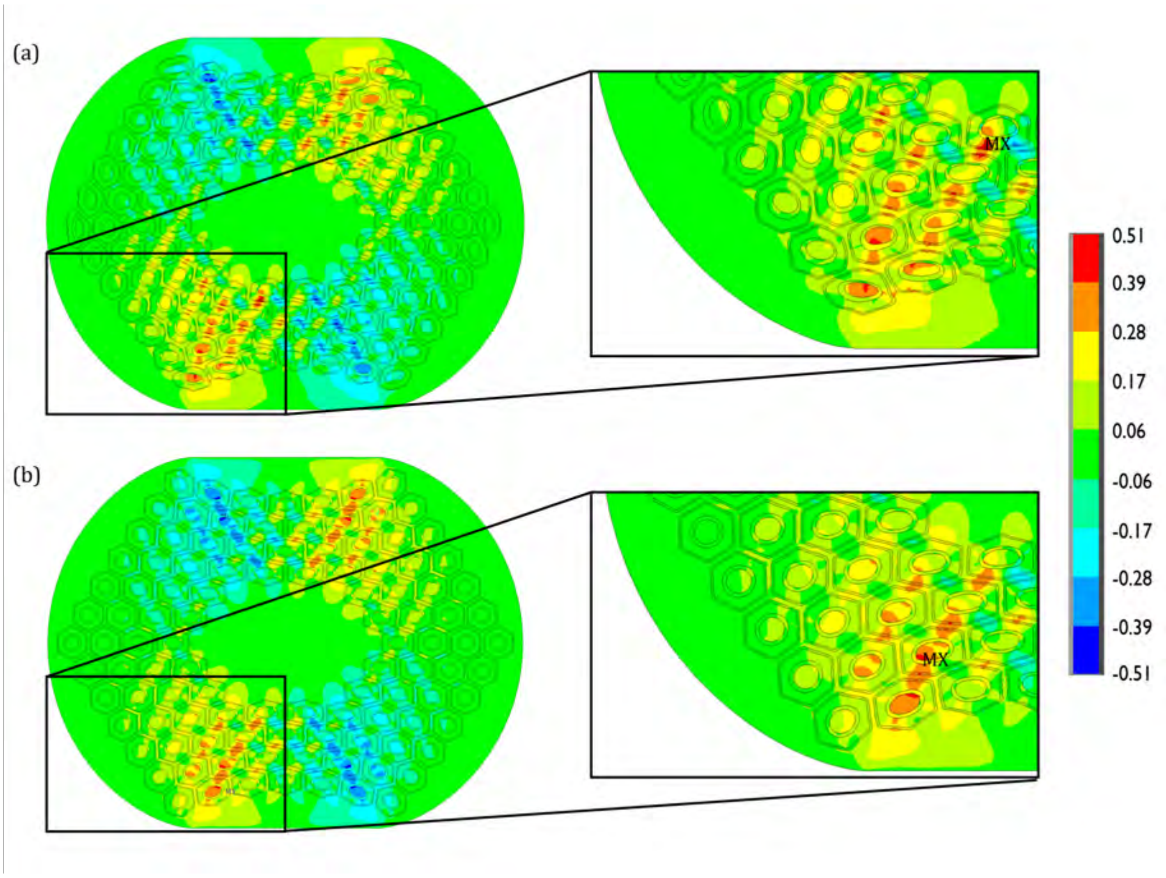

Figure 4.9: Shear strain for the model with the perfect SEM geometry (a) and for the model with the ideal geometry (b) both with properties measured at CERN.

4.3.3 Effect of the mechanical properties

As the two selected sets of mechanical properties exhibit similar values and yield comparable results (see Fig. 4.8), a comprehensive parametric study was undertaken to evaluate the influence of the properties of the different components. The aim was to vary the mechanical properties of each component individually to identify which, if any, have the greatest influence on the simulated wire deformation. Several factors were considered in the selection of variables for this study. Young's modulus remained relatively consistent across the different references consulted because this property is generally less sensitive to material conditions, such as cold work, purity levels or grain size. In contrast, yield strength and tangent modulus are more strongly influenced by the specific chemical composition and thermomechanical processing history. Furthermore, the influence of the tin core's mechanical properties was expected to be negligible in these RRP designs, primarily because the tin is physically enclosed by the niobium within the subelement cores, which limits its impact on the overall stress distribution. Similarly, estimates for copper yield stress were consistent across available datasets.

To assess the specific influence of the tangent modulus, the analysis incorporated data provided by Barzi et al. [79]. Consequently, parameter variations were applied to both material property datasets: those from Rochepault et al., and the measured properties. These variations included a ±10% variation in the copper yield stress and a more substantial ±30% variation in the yield stress of the Nb/Cu filament pack. Furthermore, the tangent moduli for the copper and the Nb/Cu filament pack were replaced with values from Barzi et al. to evaluate the impact of the tangent modulus. As illustrated in Fig. 4.10, the results of this sensitivity analysis indicate that, within the investigated ranges, variations in material properties have a remarkably limited impact on the average percentage difference.

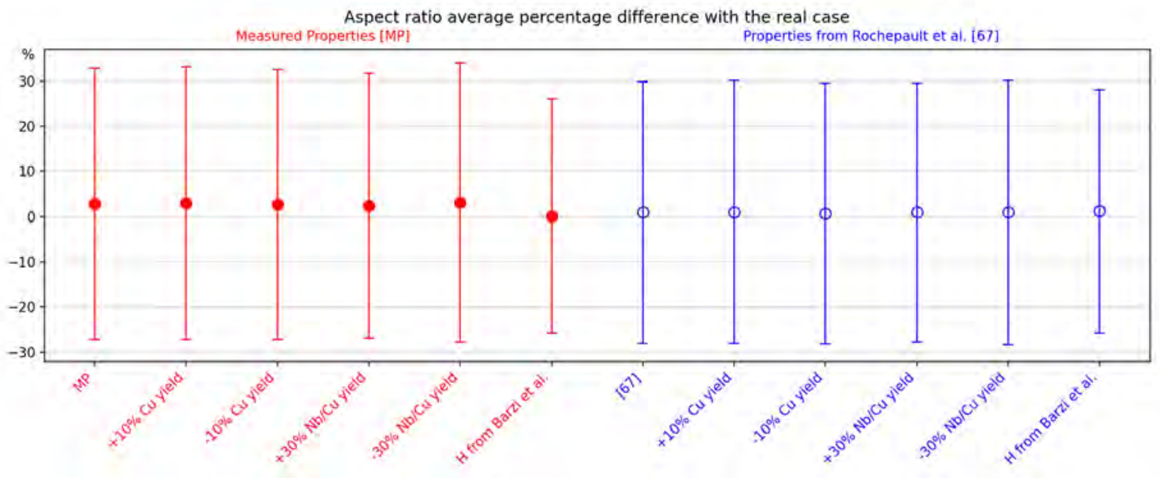

Figure 4.10: Average percentage difference between the actual wire and the model with the geometry taken from the SEM micrograph when varying the mechanical properties.

4.4 Stress and Strain Analysis

The shear and equivalent stress and strain states across the wire cross-section were also investigated. As previously established, the idealised geometry does not accurately reflect the actual cross-sectional configuration of the strand, particularly with regard to the shape of the subelements near the periphery. This leads to less accurate predictions of stress and strain distributions than the experimental evidence. Consequently, the analysis was conducted using the model based on SEM-derived geometry, which provides a more accurate representation of the wire's mechanical response. Regarding the material properties, as the differences between the various property datasets were not substantial, the results presented below refer to the model incorporating the measured properties (MP) obtained at CERN as the representative case.

The distribution of shear stress (Fig. 4.11) and shear strain (Fig. 4.12) reveals clear localisation along the 45° diagonals. This pattern is particularly significant as these diagonal bands correspond to regions where diffusion barrier failures are most frequently observed [72]. Furthermore, the equivalent stress (Fig. 4.13) and strain (Fig. 4.14) maps show that the central region of the wire experiences high mechanical loading. This suggests that subelements near the wire core are subjected to the highest levels of deformation during the rolling process.

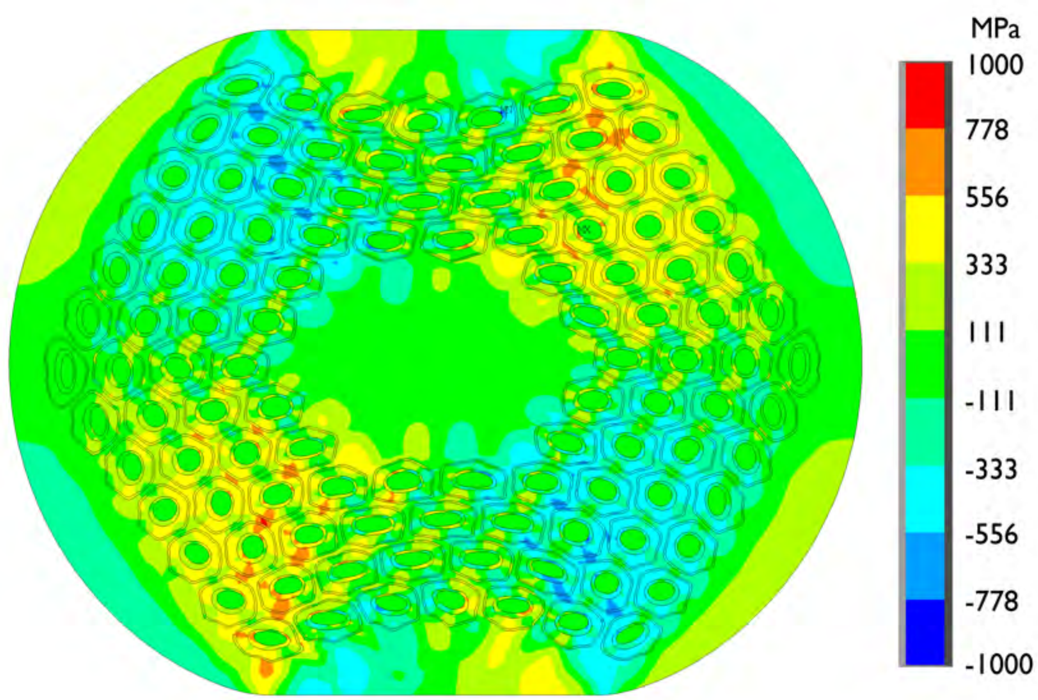

Figure 4.11: Shear stress in the wire for the model with the geometry taken from the SEM micrograph and properties measured at CERN.

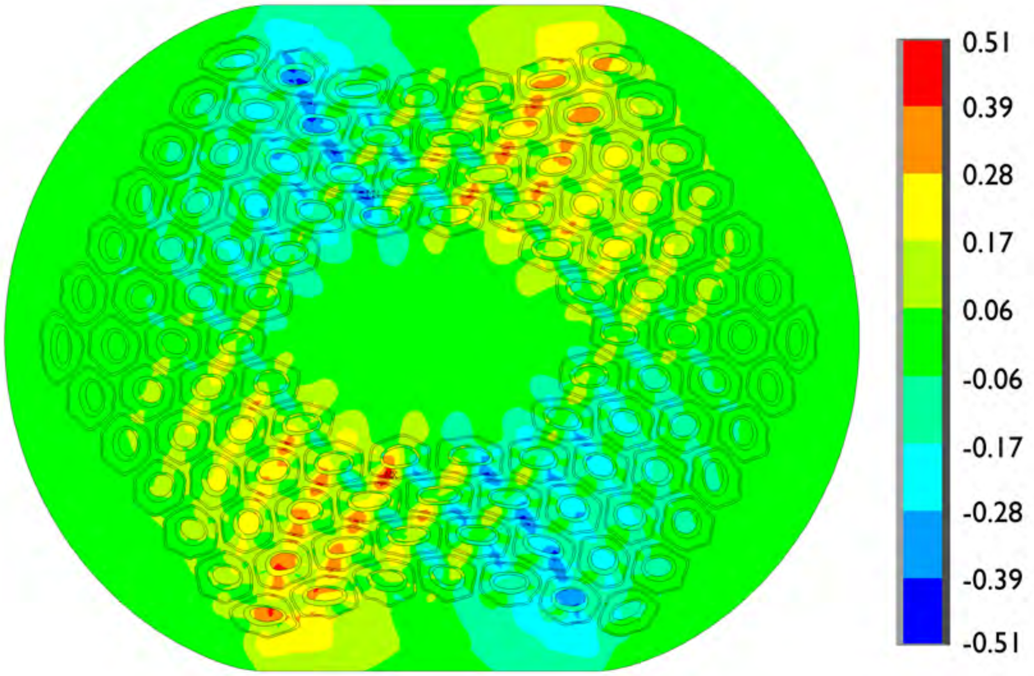

Figure 4.12: Shear strain in the wire for the model with the geometry taken from the SEM micrograph and properties measured at CERN. Note: strain is dimensionless.

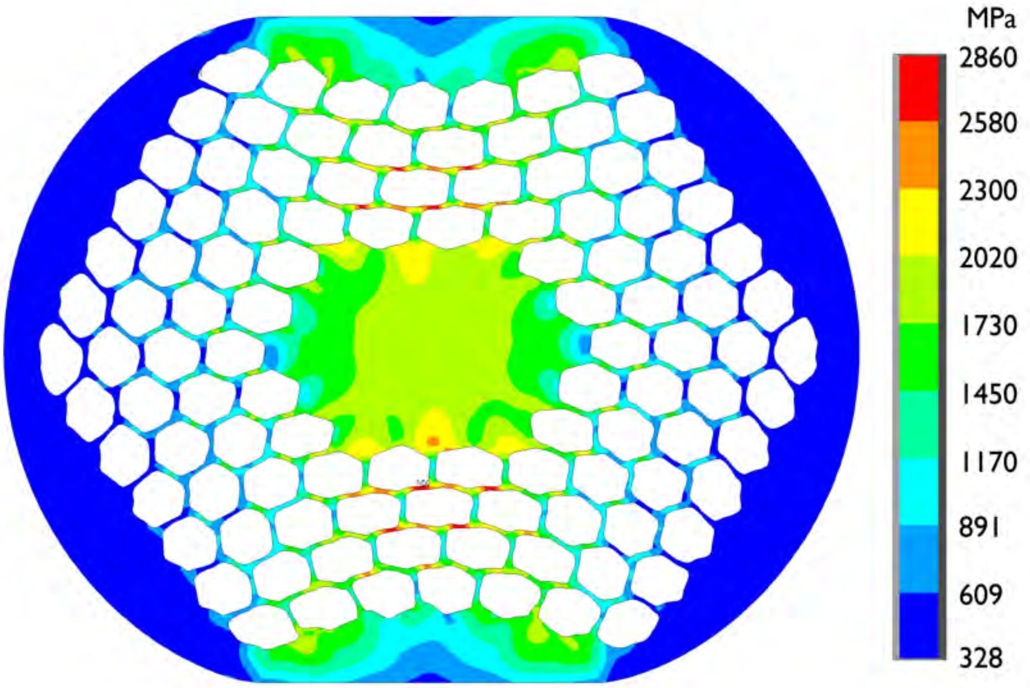

Figure 4.13: Von Mises stress in the copper matrix for the model with the geometry taken from the SEM micrograph and properties measured at CERN.

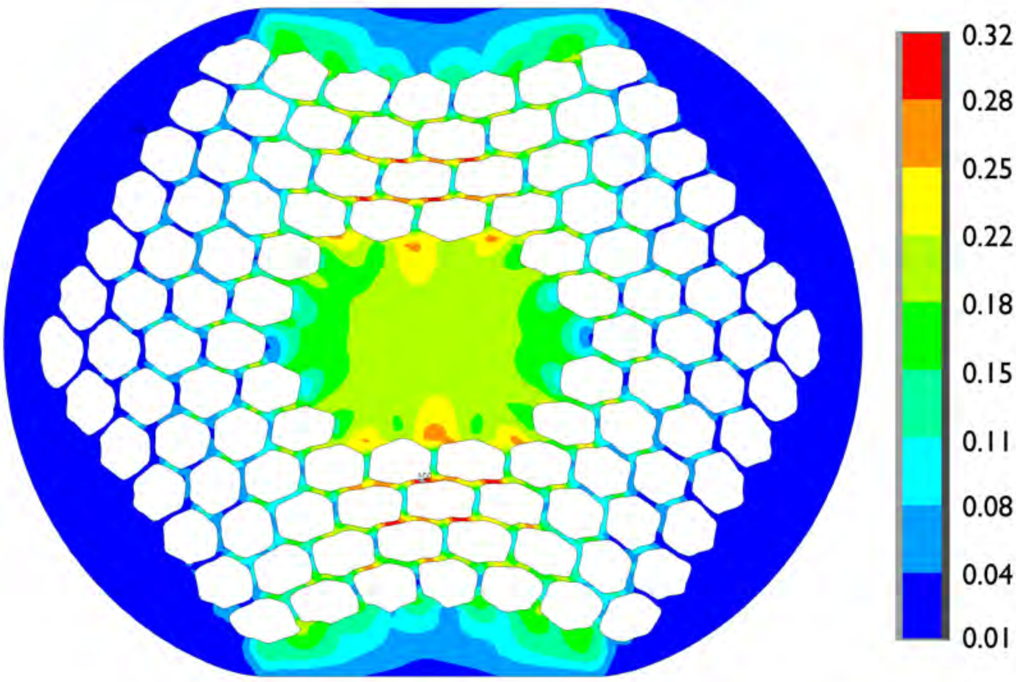

Figure 4.14: Total equivalent strain in the copper matrix in the copper matrix for the model with the geometry taken from the SEM micrograph and properties measured at CERN. Note: strain is dimensionless.

To provide a more rigorous quantification of these observations, the partitioning of the elliptical cross-section previously described was applied. Using the zones labelled A to L (see Fig. 4.7), the average percentage differences relative to the undeformed state were calculated according to Eq. 4.2. The results were then grouped by symmetry to facilitate a systematic comparison.

$$\%Change = \left(\frac{Parameter_{def} - Parameter_{undef}}{Parameter_{undef}}\right) \times 100 \tag{4.2}$$

As shown in Fig. 4.15, the zones along the diagonals and near the centre exhibit the greatest differences, which confirms that these sub-elements undergo the greatest deformation. In line with the procedure established for the experimental analysis, the same quantification was performed on SEM micrographs of both undeformed and deformed wires. This enabled a direct comparison of the deformation trends to be made, identifying zones A+B+C+D and E+F as the regions most heavily affected in both the models and the physical samples (see 4.15). These findings are consistent with experimental evidence from more severely deformed wires, where these specific areas typically exhibit mechanical failure first [79]. However, a notable discrepancy emerges when the simulation results are compared with the real wire data. As shown in Fig.

4.15, the region of the real wire that has undergone the most deformation corresponds to zones A+B+C+D ($\%Change = 97\%$). In contrast, the numerical models predict the highest deformation to occur in zones E+F, yielding values of 92% and 94% for the SEM-derived and idealised geometries, respectively. This shift in the location of the most deformed area suggests that the actual distribution of stress and strain during processing may be influenced by factors not yet fully captured by the simulations. This indicates the need for further refinement of the current modelling approach and warrants further investigation.

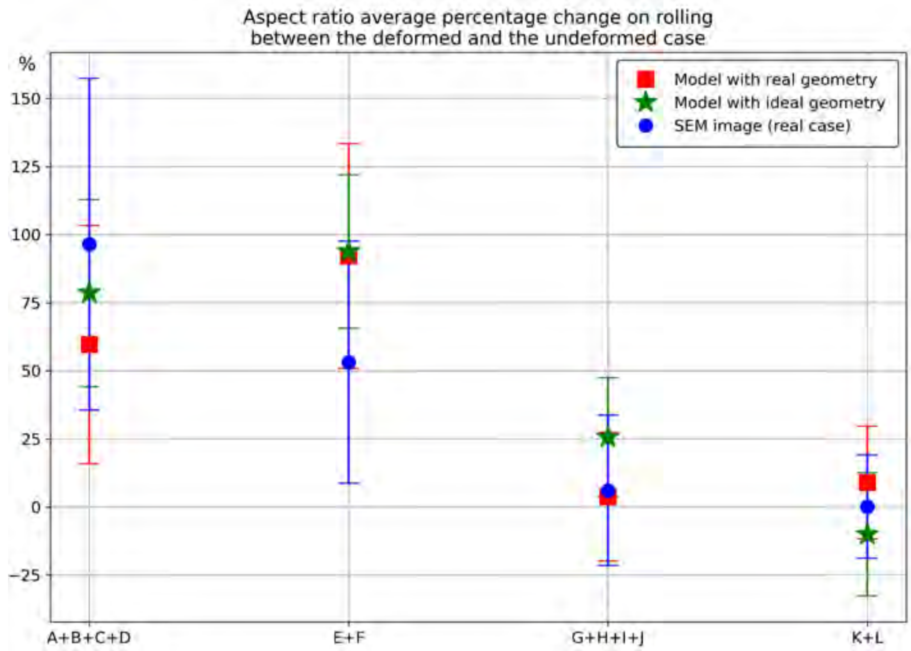

Figure 4.15: Average percentage differences for the aspect ratio between undeformed and deformed wires divided in zones. Red squares and green stars represents the case for the model prediction and blue dots for the experimental results.

4.5 Rotated models analysis

During the formation of a Rutherford cable, the wires are twisted in a helical pattern, causing them to assume different orientations as they advance through the cable. Consequently, the same cross-section of the wire may encounter the final compression at different angles. To represent this variability numerically, the orientation of the wire with respect to the direction of compression was varied in the finite element model, while keeping the way in which the deformation is applied unchanged, as shown in Fig. 4.16. Rotations of 5°, 10°, 15°, 20°, 25° and 30° were considered. These were chosen to regularly sample a range of possible orientations of the section during cabling; greater angles were not analysed because, due to symmetry, equivalent configurations recur beyond 30°.

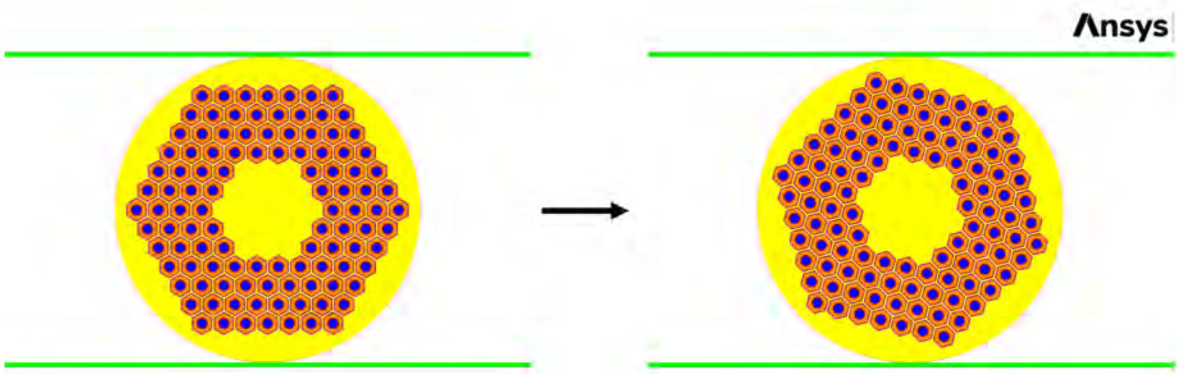

Figure 4.16: Representation of a rotation of 15° of the wire in the model.

For the purposes of this analysis, the idealised geometry of the wire was utilised. As outlined in the validation section, this geometry does not capture the local irregularities present in the actual cross-section. However, it correctly reproduces the overall arrangement of the sub-elements and provides a suitable basis for a preliminary assessment of the influence of load orientation. As the objective is not to quantitatively reproduce the experimental micrographs, but rather to qualitatively characterise the sensitivity to rotation, the use of the idealised model is suitable for this type of analysis.

As shown by the shear strain maps (Fig. 4.17), the diagonal localisation associated with compression is consistent across all simulations. However, the local distribution of shear varies from one orientation to another. By adjusting the arrangement of the sub-elements with respect to the direction of compression, the deformation is redistributed because the local constraints imposed on the matrix change. Depending on the angle considered, the stress can act on an edge, a side, or areas characterised by different spacings. This results in a slight but noticeable modification to the shape and intensity of the localisation. This local variation can generate a slightly asymmetrical distribution of shear in rotations where the arrangement of the sub-elements is not symmetrical. However, this asymmetry is not present in the original model and in the 30° configuration, where the arrangement with respect to the direction of compression is symmetrical. The analysis indicates that the shear strain is concentrated along the 45° diagonals, as observed in the original model, while the lateral regions of the section show reduced levels of deformation.

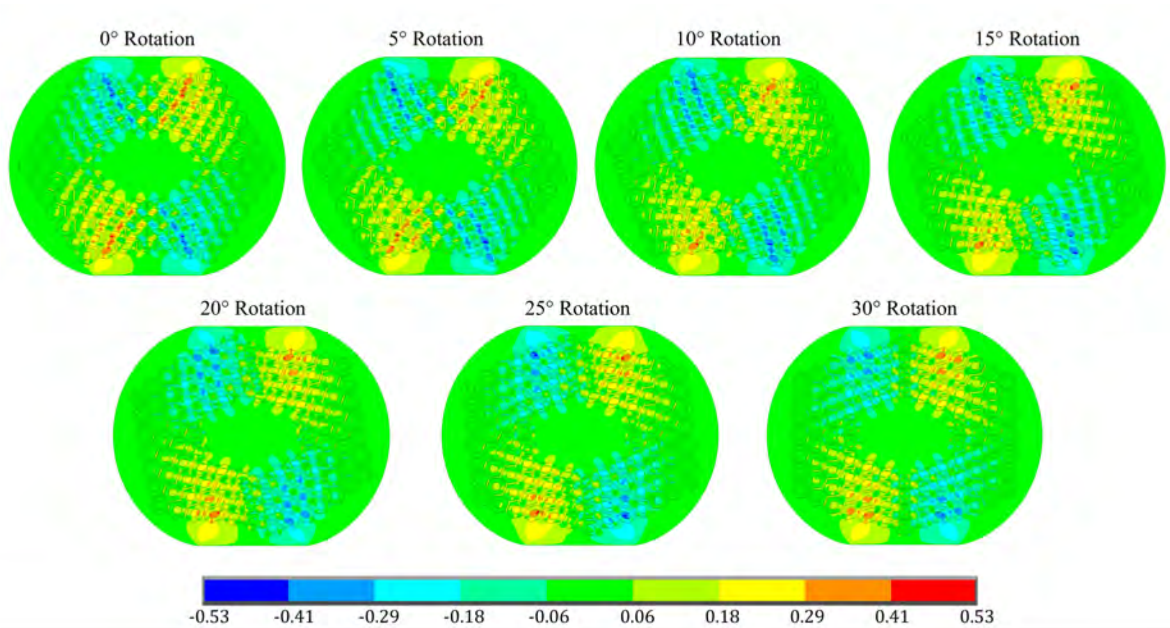

Figure 4.17: Shear strain distribution for the different rotation of the wire.

A similar behaviour emerges from the analysis of the equivalent strain in the copper matrix. As previously mentioned, the area of highest deformation is always located in the central region, while the appearance and extent of this area vary slightly with orientation due to different local geometric conditions. Specifically, in the 30° rotation configuration, the compression immediately intercepts a sub-element in the upper part of the section, rather than a row of sub-elements as in the other rotations. This results in a more compact distribution of equivalent strain and reduces the local peaks visible in the other cases. Overall, however, the rotations confirm the behaviour observed in the base model, with the central sub-elements experiencing the highest equivalent strain levels and the lateral ones remaining less affected.

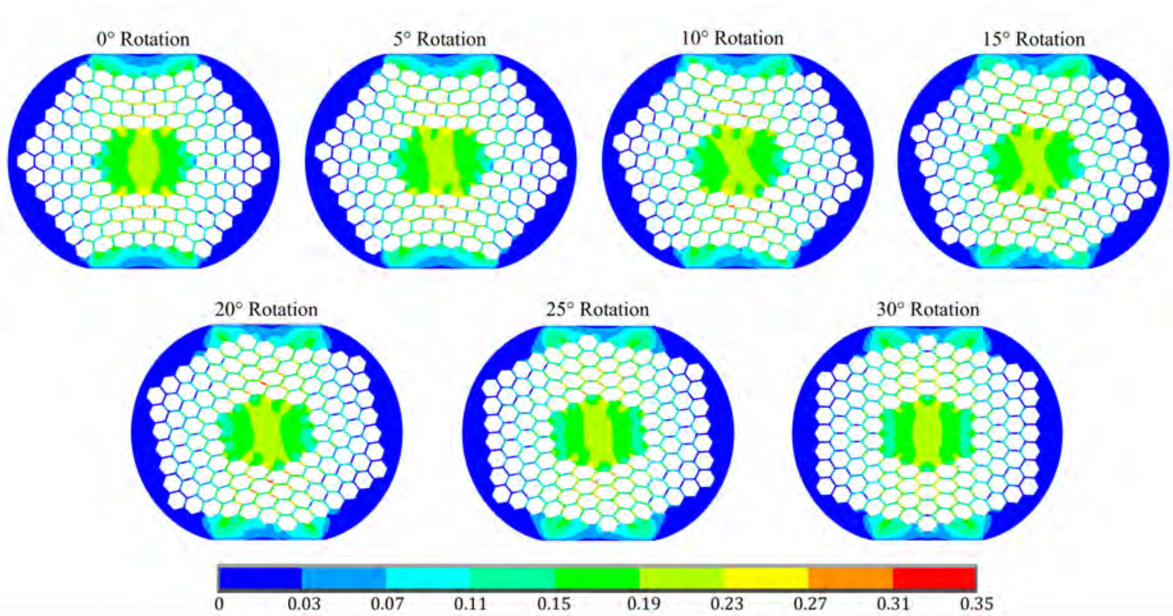

Figure 4.18: Shear strain distribution for the different rotation of the wire.

Overall, the rotated simulations show that the orientation of the wire does not alter the overall deformation mechanism. The diagonals associated with compression and the higher concentration of strain in the central part are evident in all configurations. The key difference that can be highlighted, however, is which subelements are present within these areas and, consequently, the level of deformation that each of them can reach, which may vary slightly depending on their different arrangement.

4.6 Model of a reacted wire

While the analysis of the rolling of the wire before the heat treatment provides fundamental insights into the mechanical limits of the conductor during fabrication, this only represents the initial stage of the material's condition. In order to fully evaluate the performance of a conductor in a superconducting magnet, the investigation must also consider the conductor's final state following heat treatment. This thermal process, which follows the winding of the coils, enables the formation of Nb_3Sn, but a key challenge lies in the material's brittleness. During magnet operation, the superconducting phase undergoes complex mechanical stress arising from differential thermal contraction during cooling and mechanical assembly, as well as intense Lorentz forces during operation. As these stresses significantly impact transport performance and consequently constrain the operational capabilities of high-field magnets, it is essential to understand how wires behave under stress following heat treatment in order to assess the impact of deformation on Nb_3Sn performance. To address this requirement, a numerical model was developed to simulate the stresses acting on the wire in its reacted state. Similar to the unreacted model, this model has been implemented in ANSYS APDL in ANSYS using PLANE182 elements with a generalized plane strain formulation. The dual geometrical approach, which utilises both idealised geometry with regular sub-elements and SEM-derived geometry, has also been used in this case. To imitate the experimental probes used in various transverse stress tests, such as those conducted at the INFN [86] and the University of Geneva (UNIGE) [87]–[89], the wire is incorporated into a resin box. The two models are shown alongside the SEM micrograph of the reacted wire in Fig. 4.19. In line with other modelling approaches [90], the presence of Kirkendall voids, which form as a consequence of the heat treatment [91], is neglected.

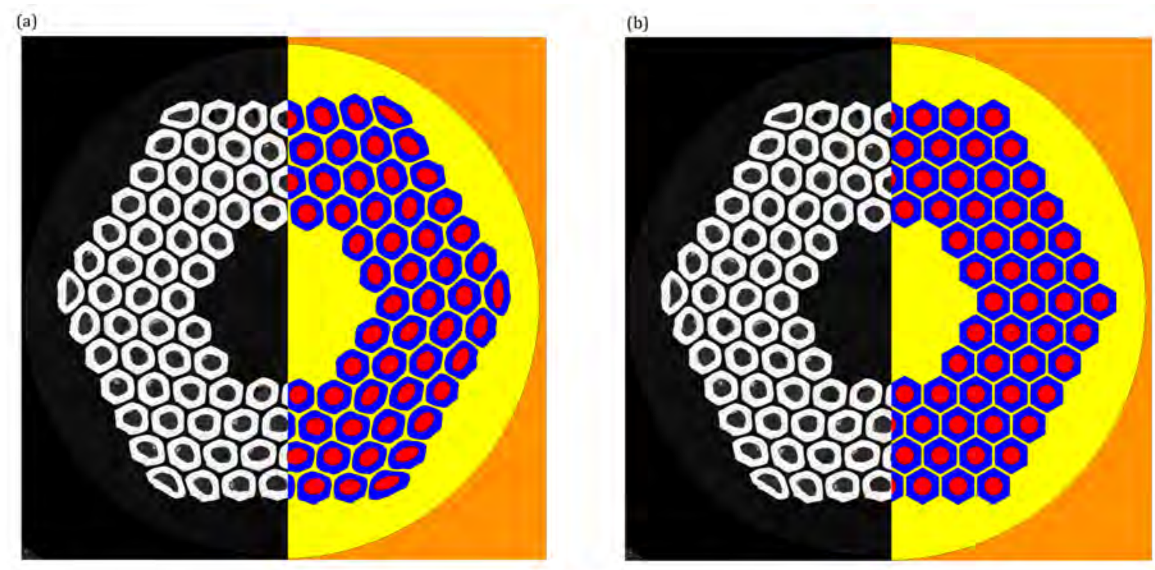

Figure 4.19: (a) FE model based on a SEM image together with the SEM micrograph of the wire. (b) Geometrical FE model together with the SEM micrograph of the wire. In the model, red represents the internal copper, blue the Nb_3Sn, yellow the copper matrix, and orange the epoxy resin.

The transverse load is applied as a uniform pressure to the top nodes of the resin box, as shown in Fig. 4.20.

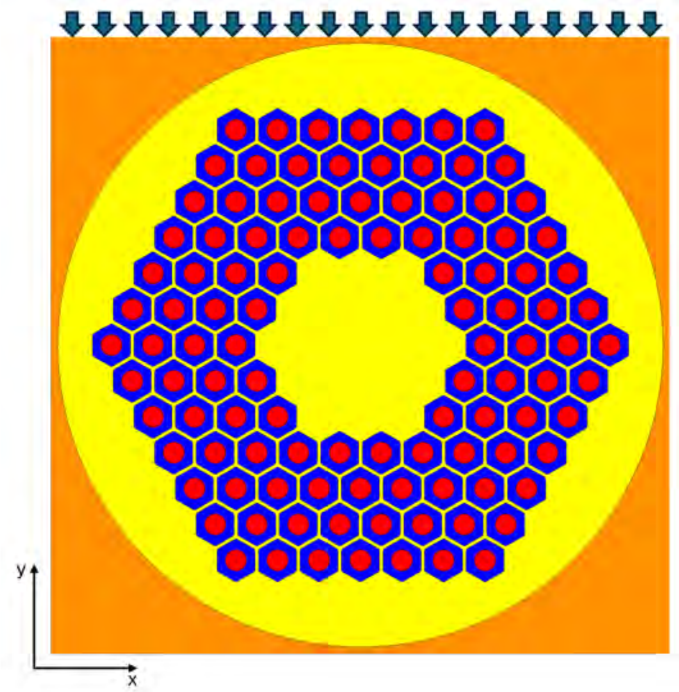

Figure 4.20: Schematic representation of how the load is applied to the model. The blue arrows represent the load.

In terms of material properties, the copper of the internal regions and of the matrix is modelled as elastoplastic, with behaviour defined by Young's modulus, yield strength and tangent modulus. In contrast, the Nb_3Sn filaments and the resin are treated as purely elastic materials characterised only by their Young's modulus, as their brittle nature precludes plastic deformation under the simulated loads. The properties are listed in table 4.2.

Table 4.2: Mechanical properties for the reacted wire

	E [GPa]	σ_y [MPa]	H [GPa]	ν
Copper	123[a]	350[a]	1.88[b]	0.3[b]
Nb_3Sn	170[a]	-	-	0.3[b]
Epoxy Resin	9	-	-	0.3

[a] Extimated at CERN by nanoindentation at CERN specifically for this study.
[b] Courtesy of G. Vernassa.

The primary objective of this model is to provide a foundation for future validation against experimental data. Once the local stress distributions obtained from the simulations have been validated through comparison with experimental measurements, the model can be used to perform preliminary assessments of the conductor's mechanical limits. Comparing these validated stress states with known I_c degradation thresholds will enable different designs and loading scenarios to be evaluated without the need for extensive experimental campaigns. Although the full simulation campaign is part of the future development of this research, the current implementation establishes the framework necessary for this quantitative analysis.

Chapter 5

The TRICHECO project

As previously discussed, the massive integration of renewable energy required by the European Green Deal calls for a radical rethinking of power transmission grids. In this context, superconducting cables represent a key solution to overcome the physical limitations of conventional systems. By enabling the transfer of gigawatt-scale power with minimal footprints and negligible losses, this technology effectively bypasses the saturation constraints of resistive conductors, even over long distances. Among the materials that can be used on a network scale, magnesium diboride (MgB_2) is distinguished by its robustness, relatively low cost and the possibility of producing reliable multifilament wires [42], [92], [93]. The material requires operating temperatures below 30 K to maintain superconductivity, and it was this cryogenic condition that provided the inspiration for developing the concept of the Superconducting Energy Pipeline (SCEP). This concept was initially proposed by Paul Grant [40], who envisioned an infrastructure capable of conveying both direct current electricity and chemical energy in the form of liquid hydrogen to a single platform. This ambitious undertaking would exploit the overlap between the thermal requirements of the superconducting material and the properties of hydrogen in its liquid state [56], [94], [95]. Within this framework, the cryogenic fluid is no longer merely an auxiliary element for cable operation but is the energy carrier itself. Liquid hydrogen guarantees the required operating conditions for the MgB_2 cable and, being in the liquid state, allows energy to be transported at its maximum density. The resulting infrastructure thus efficiently unifies two traditionally separate energy flows, thereby maximising the interaction between the superconducting material and the cryogenic fluid. [34], [36], [37], [41], [51]–[53], [96], [97].

The validity of this approach is no longer purely theoretical, but is supported by a significant series of technological demonstrations [36], [41]. The European Best Paths project is a prime example of this, having developed and tested very high power superconducting architectures (up to 3.2 GW at 320 kV) based on magnesium diboride (MgB_2) superconductors. These tests, conducted using gaseous helium (GHe) as a coolant at operating temperatures between 15 K and 25 K, demonstrate the stability and reliability of an MgB_2 cable when used on a grid scale. The cable has successfully passed HVDC test programmes for the 200kV and 320kV voltage classes. [34], [58], [61]. Further confirmation is provided by the Superconductor Links at CERN, where MgB_2 multifilament cables ensure the continuous transport of extremely high currents, with a total system capacity of 150 kA at operating temperatures between 20 K and 25 K. These connections operate in a real and complex operating environment, such as the underground tunnels of the LHC, demonstrating the industrial maturity of the material through production that has already reached the kilometre scale. Extensive testing campaigns on tensile stress and triple bending cycles have validated the mechanical robustness of the architecture, demonstrating that the material can withstand installation stresses and Lorentz forces without significant degradation of electrical performance. [62], [92], [93], [98]–[101]. In Italy, INFN's IRIS (Innovative Research Infrastructure on applied Superconductivity) project is leading the development of the Green Superconducting Line (GSL), a power cable demonstrator that will be tested in the new laboratory in Salerno. The demonstrator, measuring 130 metres in length, is designed to carry 1 GW of power with a current of 40 kA at a voltage of 25 kV, operating with almost zero dissipation thanks to the use of MgB_2 conductors. The line is engineered to operate at a temperature of 20 kelvin using gaseous helium as a coolant. This choice significantly reduces energy consumption and environmental impact when compared to traditional systems. [59].

Regarding hydrogen integration, prototypes developed by VNIIKP (Russian Scientific R&D Cable Institute) provided the world's first experimental evidence of the feasibility of simultaneously transporting direct current electricity and liquid hydrogen. Through a technological progression that saw the testing of a first 10-metre line in 2011 and a subsequent 30-metre flexible system in 2013, the principle behind SCEPs (Superconducting Energy Pipelines) was validated. These tests have demonstrated that liquid hydrogen can serve as both a high-density chemical energy carrier and an ideal cryogenic fluid for cooling the MgB_2 cable, achieving a total transport capacity of up to 135 MW (approximately 60 MW of chemical power and 75 MW of electrical power) in the demonstrators. [55], [60], [95], [102]–[104]. More recently, the European SCARLET programme has expanded this vision to gigawatt-scale MVDC (Medium Voltage Direct Current) systems. The project involves the integration of MgB_2 superconductor cables into pipelines designed to transport liquid hydrogen (LH_2) at temperatures of around 20 K. This dual-purpose infrastructure, also referred to as a "hybrid transmission" system, has been developed for the purpose of connecting energy-intensive industrial hubs, such as steelworks, and strategic port terminals. The objective of this study is to demonstrate the feasibility of a system capable of simultaneously transporting up to 1 GW of electrical power through a bipolar connection at $\pm$25 kV and 20 kA, while providing large flows of liquid hydrogen (up to 10 t/h) to meet industrial and logistical demand. This approach eliminates the need for expensive HVDC conversion stations and transforms the cost of cryogenic fluid into a source of profit through fuel delivery. [36], [37], [41], [51], [52].

The TRICHECO project, developed as part of an Italian High-Relevance National Project, fits into this context. The initiative is the result of collaboration between the Politecnico di Torino, the University of Bologna and INFN (Genoa section) with the aim of validating the technical and economic feasibility of a hybrid submarine infrastructure for the simultaneous transfer of electricity and liquid hydrogen (LH_2). This objective will be accomplished through the analysis of a real case study in the Adriatic Sea, off the coast of Romagna. The identified area will host an offshore energy hub (Romagna 1) consisting of a 200 MWe wind farm integrated with a 100 MWe floating photovoltaic plant located approximately 22 km from the coast, a second 400 MWe wind farm (Romagna 2) planned 26 km away, and an electrolyser system with a production capacity of up to 4000 tonnes of hydrogen per year [105]. In an offshore production scenario, the use of a single 30 km-long hybrid pipeline allows hydrogen to be conveyed in its maximum energy density configuration while simultaneously transporting low-voltage electricity with minimal losses using a MgB_2 superconductor cable, cooled under its critical temperature by the liquid hydrogen itself. The design of this pipeline requires an integrated multidisciplinary approach ranging from electromagnetic and thermo-fluid dynamic modelling — essential for defining operating parameters and studying the behaviour of the system in the event of electrical or cryogenic failures — to the assessment of mechanical robustness. The research also extends to the sizing of the entire plant, including the study of the necessary auxiliary components (such as storage tanks, pumps and current terminals) and a comparative techno-economic assessment with respect to conventional transmission technologies. Through these analyses, the TRICHECO project aims to demonstrate the competitiveness of a facility capable of transporting large amounts of energy with minimal losses and reduced environmental impact, defining a scalable trajectory for future integrated energy infrastructures.

5.1 Liquid hydrogen

The use of hydrogen as energy carrier is emerging as one of the most promising solutions for a decarbonised global energy system. The transition to a sustainable hydrogen-based energy system is considered essential to achieving ambitious international climate targets, such as reducing greenhouse gas emissions by 80–95% by 2050 [106]–[114]. Hydrogen has the potential to facilitate carbon emission reductions in energy-intensive sectors, known as "hard-to-abate", where direct electrification is not efficient. These include long-distance and heavy transport, the chemical industry (such as ammonia production, fertilisers and refining) and mineral processing, with particular reference to green steel production [106], [108], [109], [112], [113], [115], [116]. Additionally, it can be integrated with renewable energy sources to facilitate energy storage through Power-to-Gas (PtG) technology, offering a solution to manage the intermittency of production and balance supply and demand on the grid [106], [110], [113]. Finally, hydrogen has the potential to serve as a means of transporting renewable energy over long distances, allowing clean electricity produced in regions with abundant resources to be exported to countries with scarce energy resources [106], [109].

In particular, liquid hydrogen is seen as a promising option due to its advantageous properties, such as high energy density, low weight, high hydrogen purity, the possibility of low-pressure storage and minimal environmental impact when used as a fuel. [107], [117]. Liquid hydrogen was liquefied first by James Dewar in 1898 [118], however, the initial research on producing liquid hydrogen was linked to the creation of nuclear and later thermonuclear weapons by the United States, beginning in the 1940s [117]. The first compact liquefier was created in 1952 by the National Bureau of Standards in Boulder, CO. Since then, there has been extensive research aimed at developing more efficient hydrogen liquefaction systems [117]. Nevertheless, the process of hydrogen liquefaction remains difficult and poses numerous obstacles for constructing a large number of effective plants [117], [119].

5.1.1 Hydrogen Liquefaction principles

5.1.1.1 Ortho to Para Conversion

Molecular hydrogen H_2 has two spin isomers: ortho-hydrogen (o-H_2), with parallel nuclear spins, and para-hydrogen (p-H_2), with anti-parallel nuclear spins. The two isomers can coexist and concentrations at equilibrium are temperature dependent, as shown in fig. 5.1. At room temperature the composition is approx. 75% o-H_2 and 25% p-H_2 and this mixture is called normal hydrogen; at the boiling point of liquid hydrogen the amount of p-H_2 significantly increase and the composition is 0.2% o-H_2 and 99.8% p-H_2. This leads to an issue for hydrogen cryogenics: the ortho-to-para conversion is exothermic (700 kJ/kg, compared to the latent heat of vaporization of 450 kJ/kg) and occurs very slowly. When hydrogen is liquefied, it initially retains its normal ortho/para composition, but spontaneously undergoes the exothermic conversion to the equilibrium para composition at the boiling point. This releases a significant amount of heat, causing nearly all of the liquid hydrogen to turn into gas. To avoid this boil-off, the conversion processes must be carried out during the liquefaction cycle using catalysis.

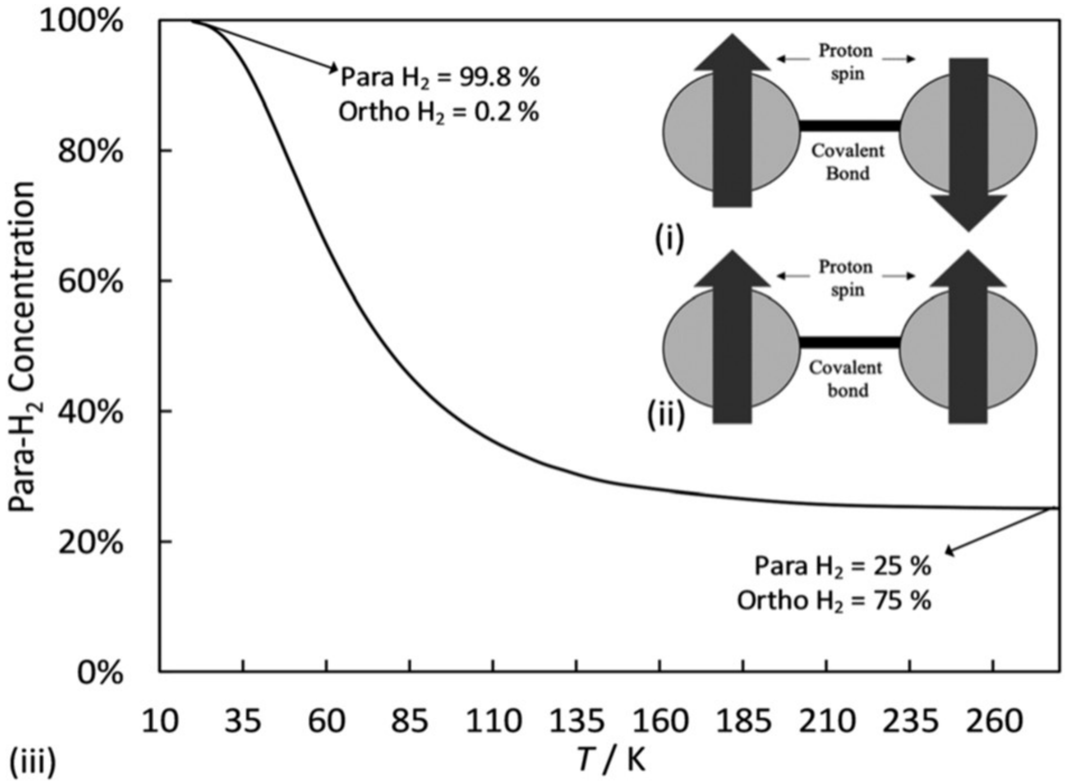

Figure 5.1: (i) para- and (ii) ortho-hydrogen spin isomers. (iii) para-hydrogen content of hydrogen at equilibrium as a function of temperature [106].

5.1.1.2 General Liquefaction Process

Conventionally, the liquefaction process consists in three subsequent steps, as can be seen in fig. 5.2:

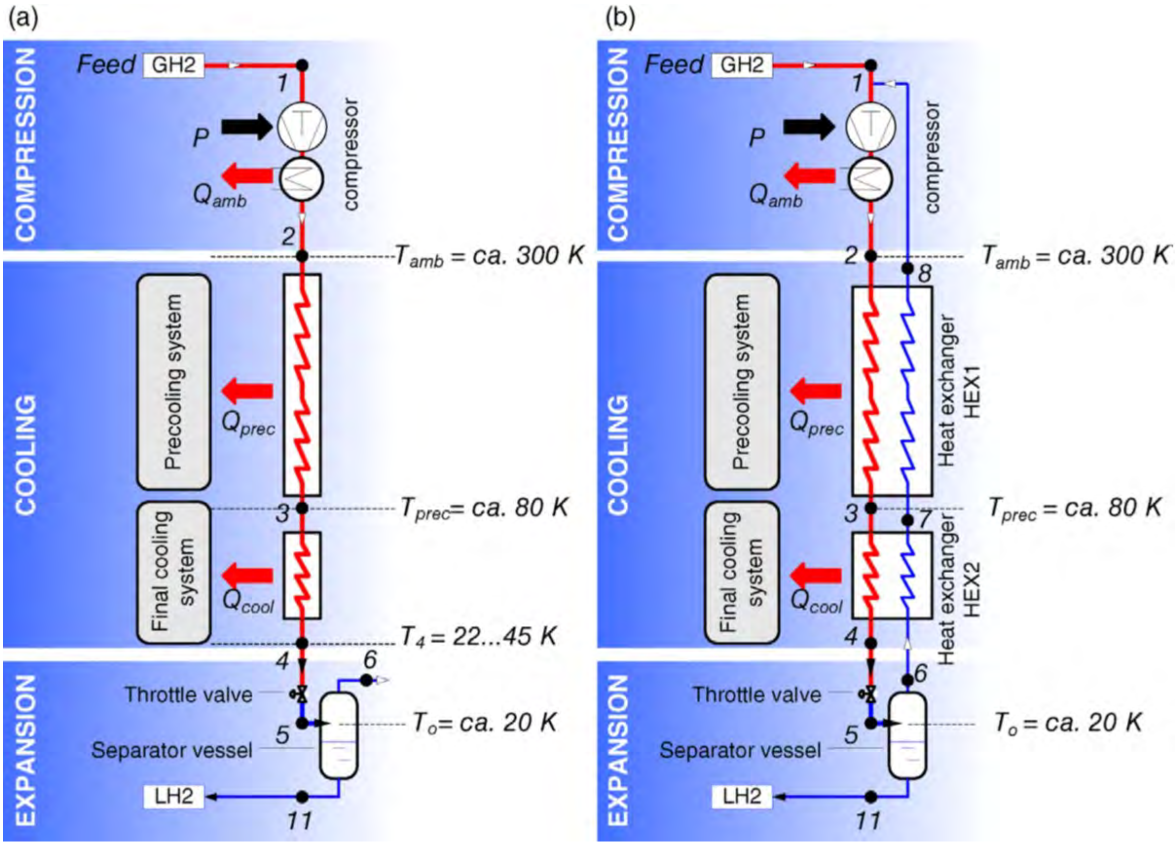

Figure 5.2: (a) general principle and (b) utilization of the flash gas cold [117].

1. *Compression*: the first stage consists in compressing pure and dry hydrogen to a pressure higher than the critical pressure.
2. *Cooling*: the second step is actually composed by two substeps:
   - pre-cooling from room temperature to 80 ± 15 K, typically using liquid nitrogen;
   - final cooling to temperatures less than 30 K, using a cryogenic refrigeration cycle. In this step is also involved the ortho to para catalysed conversion.
3. *Expansion*: the final step is an adiabatic and isenthalpic expansion from high pressure to low pressure using a throttle valve. In this process hydrogen becomes colder and partially liquefies, the liquid part is stored in a vessel and the vapor fraction, the so-called flash gas, is used as a refrigerant in the cooling step.

Liquefaction methods have developed over time in response to the changing requirements. From 1898 to 1960s the primary goals were to simplify process design and build hydrogen infrastructure by gaining operational experience. This results in processes involving compression to extremely high pressure, pre-cooling with liquid nitrogen, cooling solely by flash gas, and expansion through a basic throttle valve. From the 1960s to the 2000s, there was a growing emphasis on the importance of cost and efficiency in the process, with a focus on reducing significant thermodynamic losses. In order to accomplish this, the hydrogen feed compression is decreased to a moderate pressure and an external cold stream is introduced. it became crucial to focus on process and cost efficiency, with redesign and optimization of the process part below 80 K being essential. External cold stream is used for pre-cooling, multiple expansion turbines are utilized in the low temperature part, the use of Joule-Thomson turbine instead of valve is investigated, and and hardware components are being further developed. [117]. Nowadays there are three dominant types of hydrogen liquefaction system: the Linde-Hampson cycle, the Claude cycle, and the Brayton refrigeration cycle [106], [120]–[122]. Their efficiency is commonly expressed using the coefficient of performance (COP), which is defined as the ratio of the cooling power produced to the electrical power consumed. Because the COP is typically low for hydrogen liquefaction, the process involves a significant energy cost. Since 1960, when the first few liquid hydrogen plants were built to support the Apollo program, several plants were built. Today, there are more than 9 hydrogen liquefaction plants in the US, 4 plants in Europe and 11 plants in Asia. The liquid hydrogen produced is used to reduce the cost of hydrogen distribution; however, the current worldwide liquid hydrogen production capacity exceeds the market demand [121].

5.2 Multiphysics analysis and system assessment

The feasibility of the SCEP system, designed for transmitting 300 MW (10 kA at 30 kV DC), has been confirmed through the analyses presented in recent scientific literature [2], [123]–[126]. These studies demonstrate the effectiveness of the magnesium diboride (MgB_2) architecture by combining electromagnetic, thermal, and fluid dynamic models to define the operating envelope of the system and its safety margins. In the validated configuration, the superconducting cable consists of a central copper former with a diameter of 8.2 mm, around which 42 multifilamentary MgB_2 wires are helically wound. The electrical insulation of the cable is provides by a multilayer dielectric insulation system, consisting of 2.5 mm of laminated polypropylene paper (PPLP) and by semiconductive layers designed to prevent local charge accumulation. The entire assembly (Fig. 5.3a), with an overall diameter of 2.6 cm, is enclosed inside a flexible corrugated cryostat consisting of two concentric stainless-steel pipes: an inner pipe that carries liquid hydrogen and an outer pipe that provides the external containment. The diameters of the inner and outer corrugated pipes were selected from commercially available products. Following an initial assessment of suitable options, two diameter pairs were identified for the inner cryostat, namely 126.2/145 mm and 151.6/171 mm. For the outer corrugated pipe, only configurations with diameters exceeding 198/220 mm were considered appropriate.

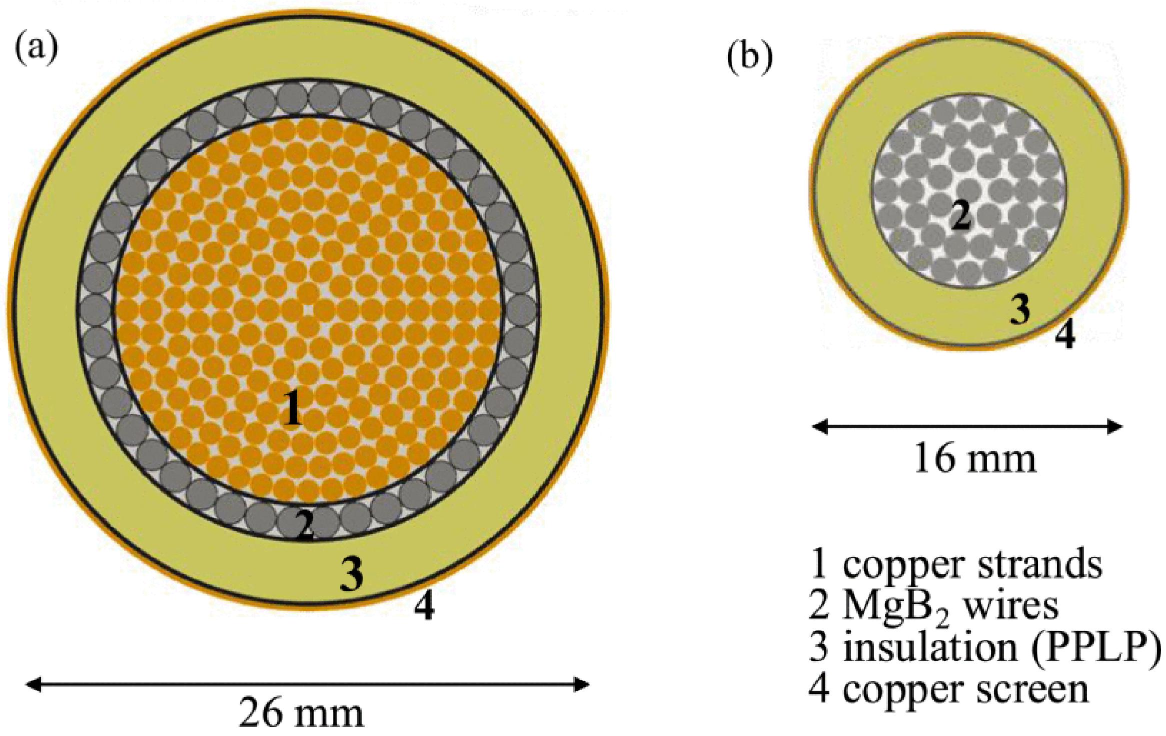

Figure 5.3: (a) Cross-section of the validated configuration of the cable and (b) Cross-section of the configuration without the copper former.

The space between the two pipes is kept under high vacuum conditions and contains multilayer superinsulation (MLI) screens to limit the parasitic heat load to less than 2 W/m along the 30 km line. These structural choices allow for the adoption of the Reel-lay method [127], in which the entire pipeline is assembled at a single site and subsequently unrolled from a cable-laying vessel for offshore installation.

Electrical fault simulations were performed with particular focus on pole-to-ground short circuits, with peak currents reaching up to 70 kA. These simulations demonstrate the stabilising role of the copper former, which absorbs the current during the quench transient and limits the temperature rise below the critical threshold of 35 K. This stabilisation mechanism is essential because, without the contribution of the copper former (configuration in Fig. 5.3b), the temperature of the superconductor would rapidly exceed 100 K. This would lead to violent boiling of the liquid hydrogen and generate overpressures in the cryostat of up to 40 bar. At the same time, the system integrates active protection devices, including superconducting fault current limiters (SFCL) and solid-state circuit breakers (SSCB), with response times of approximately 60 ms, which are necessary to limit the extent of transients and ensure the electrical and thermal integrity of the conductor.

From a fluid-dynamic perspective, simulations performed with the OPENSC2 calculation code [128] demonstrate that thermal management can be sustained with a minimum hydrogen flow rate of 0.5–0.6 kg/s, ensuring the fluid remains in a liquid state between 20 K (inlet) and 29 K (outlet). Building on these steady-state requirements, the robustness of the design has been further evaluated through the simulation of cryogenic failure scenarios, ranging from manageable incidents to critical emergencies. The least severe event, known as Loss-Of-Flow Accident (LOFA), involves a pump failure causing a gradual temperature rise detectable at the outlet on a 10^4 s timescale, allowing for the electrical load to be reduced without system damage. A more complex scenario is the Loss-Of-Coolant Accident (LOCA), where a breach in the inner wall leads to hydrogen leakage into the vacuum jacket. This intermediate failure requires the use of palladium-coated FBG sensors for early chemical detection before thermal signals develop. The most critical scenario, however, is the Loss-Of-Vacuum Accident (LOVA), where a breach of the outer wall allows seawater ingress. The resulting ice formation releases a significant amount of latent heat (up to 3×10^3 W/m), which requires the implementation of distributed fibre optic monitoring along the 30 km line to immediately detect the accident. To address these accidents, the project proposes a diagnostic layout, shown in Fig. 5.4, that integrates traditional sensors (pressure, temperature, flow) with distributed fibre optic systems. Additionally, the installation of safety valves at the terminals and intermediate points is essential to prevent mechanical damage from overpressures caused by sudden hydrogen evaporation.

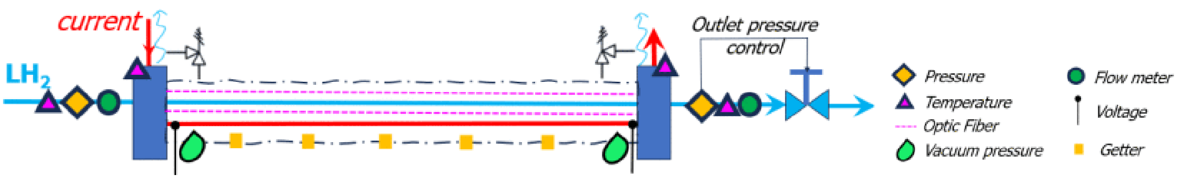

Figure 5.4: Proposed instrumentation layout for detecting cooling-related incidents in the hybrid cable.

The operation of the SCEP system is supported by auxiliary componenets located at the line terminals. This infrastructure, shown schematically in Fig. 5.5, integrates hydrogen storage, pumping systems, and electrical interfaces that connect the cryogenic section to external networks.

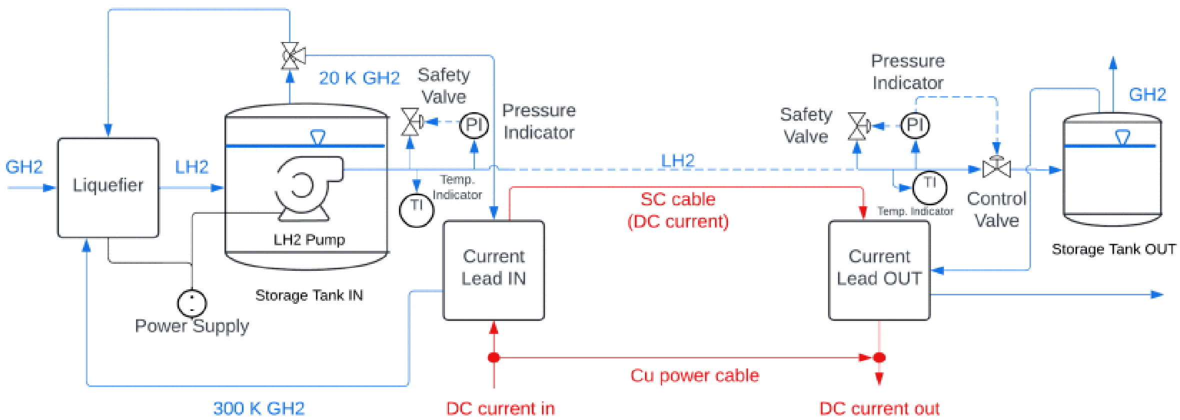

Figure 5.5: Layout of the hybrid pipeline, showing the auxiliaries for the supply and management of the cryogen.

Fluid management is handled by two 150m^3 tanks located at the ends of the pipeline. A submerged cryogenic pump ensures flow rates of up to 1.4 kg/s, thereby maintaining the operating temperature below 29 K. The electrical connection is made via differentiated terminals: a hybrid HTS/REBCO design at the inlet to minimise heat input, and a copper terminal at the outlet, which allows Joule heat to be recovered for heating the hydrogen destined for users. The system is completed by AC/DC conversion infrastructure necessary for interfacing with offshore generators and the national grid. While auxiliary components account for 25% of the total CAPEX (approximately €80 million), the majority of the cost is dominated by electrical conversion systems, with cryogenic units such as pumps and tanks accounting for only 3% of the investment.

In addition to the sustainability of individual components, the integration of SCEP into the national energy system, as assessed using the TEMOA-Italy model [129], is crucial for achieving net-zero targets. With an economic competitiveness threshold set at €610 million/km/MW, which could rise to €1,430 million/km/MW if the costs of traditional materials double, SCEP emerges as a competitive solution for the long-distance transport of large energy volumes, primarily due to its near-zero transmission losses. In order to validate this competitiveness, the model adopts an operating configuration with a nominal electrical power of 300 MW and an equivalent hydrogen power of 240 MW (based on a flow rate of 2 kg/s), operating with a transmission efficiency of 99% for hydrogen and 75% for electricity, including the energy required for liquefaction, corresponding to roughly 0.404 kWh of electricity per kWh of hydrogen energy. At the system level, SCEP would facilitate the restructuring of Italy's energy geography. While the analysis has focused on the implementation of the technology in the Adriatic basin, the TEMOA-Italy model demonstrates the solution's scalability and strategic relevance in other national geographical contexts. In particular, Sardinia is poised to play a pivotal role. The construction of the pipeline will enable the island to increase production through electrolysis by approximately ten times compared to the baseline scenario. This transformation will position Sardinia as an export hub for the industrial centres of northern Italy, effectively changing its status from a local consumption area to a significant economic hub. By effectively resolving the mismatch between production areas and consumption centres, SCEP acts as an enabling infrastructure that makes this production restructuring economically viable, thereby supporting Italy's transition towards the 2050 net-zero targets.

5.3 Thermo-mechanical analysis

In the field of studies dedicated to technologies based on MgB2 superconductor cables, significant progress has been made in recent years in the analysis of electromagnetic, thermal and fluid-dynamic phenomena. However, thermo-mechanical aspects are still being developed in less detail. The primary focus has been on the description of electrical transients, quench management and the behaviour of cryogenic fluid inside the cryostat. However, the structural response of components under real operating conditions is often represented using simplified models or applied to limited portions of cable. The geometric complexity of multi-wire cables, the heterogeneity of the materials used, the scarcity of reliable experimental parameters and the difficulty of modelling extended three-dimensional domains on a kilometre scale contribute to this methodological gap, which becomes particularly relevant in light of possible large-scale industrial applications. While it is possible to describe the set of thermo-mechanical phenomena along the entire submarine section in a fully coupled manner, such an approach would introduce a level of complexity that is disproportionate to the design objectives. It is therefore more effective to focus the analysis on those mechanisms that directly affect the behaviour of the system under the expected operating conditions. From this perspective, it is beneficial to consider the structural response of the cryostat and the behaviour of the superconductor cable during cooling separately. This will allow for a clear understanding of the physical characteristics of each of the two subsystems.

In the case of the cryostat, cryogenic cooling causes the inner wall to contract, which, when combined with the corrugated geometry of the tube, modifies the distribution of deformations along the structure. In addition to this behaviour, there is a pressure difference between the inner and outer surfaces of each corrugated tube, a parameter that directly governs the stress state of the wall. The response resulting from the interaction between thermal contraction and pressure difference is therefore the main criterion for assessing the cryostat's resistance to the expected operating loads and for verifying its suitability for use under the operating conditions considered. Furthermore, the design must take into account the assessment of stresses related to system pressure. While the management of internal pressure is a typical requirement for cryogenic piping, in the case of submarine installations, the hydrostatic load exerted by the water column introduces an additional contribution that further modifies the stress picture. The combined action of the external water pressure on the corrugated outer tube, the internal hydrogen pressure and thermal contraction of the corrugated inner tube, and the constraints at the ends connecting the two tubes imposes more severe operating conditions than in non-submerged cases and defines the limits of structural feasibility of the cryostat. This requires specific analysis to establish its reliability under actual operating conditions.

At the same time, superconducting cables have mechanical characteristics that require specific attention. Their multi-strand twisted structure and the presence of materials with different thermal expansion coefficients result in non-uniform behaviour along the entire section during the cooling process. The differences in contraction between the various components can generate localised tension in the MgB2 filaments and contribute to a reduction in the overall length of the conductor. This phenomenon is known as shrinkage, and it is particularly significant when considering distances of several kilometres. Accurate quantification of this shortening is a key aspect of the design. During the transition to operating temperature, the cable contracts while the terminations and connecting elements at its ends remain fixed. If the cable is too short, the additional contraction induced by cooling can cause it to work in traction against these rigid parts, generating unwanted stresses that can compromise the integrity of the system. Conversely, overestimating shrinkage can result in the manufacture of a cable that is longer than necessary, leading to increased costs due to the greater amount of material used. To avoid both of these conditions, shrinkage estimates cannot be based on overly simplified models, but require a geometric and material representation that is sufficiently accurate to reflect the actual behaviour of the conductor during cooling.

The separate but complementary analysis of these two systems allows us to define a coherent methodological framework that can be used to fill the gaps in the literature. A comprehensive understanding of the structural mechanisms affecting the cryostat and the cable during cooling and under load facilitates the establishment of more reliable design criteria and provides concrete support for the development of future hybrid pipelines for the integrated transport of electricity and liquid hydrogen.

5.3.1 Analysis of the cryostat

The cryostat was modelled using Ansys APDL, adopting a finite element approach aimed at realistically describing the mechanical response of the two corrugated tubes. Both tubes have a wall thickness of 1 mm, with the inner tube measuring 151.6 mm in inner diameter and 171 mm in outer diameter, and the outer tube measuring 198 mm in inner diameter and 220 mm in outer diameter. Since the behaviour of the section is axially symmetric, it was possible to exploit this symmetry to construct a two-dimensional model of the cross-section, shown in Fig. 5.6. The finite element used is PLANE183, which is suitable for modelling structures with complex geometries, used in the axisymmetric formulation.

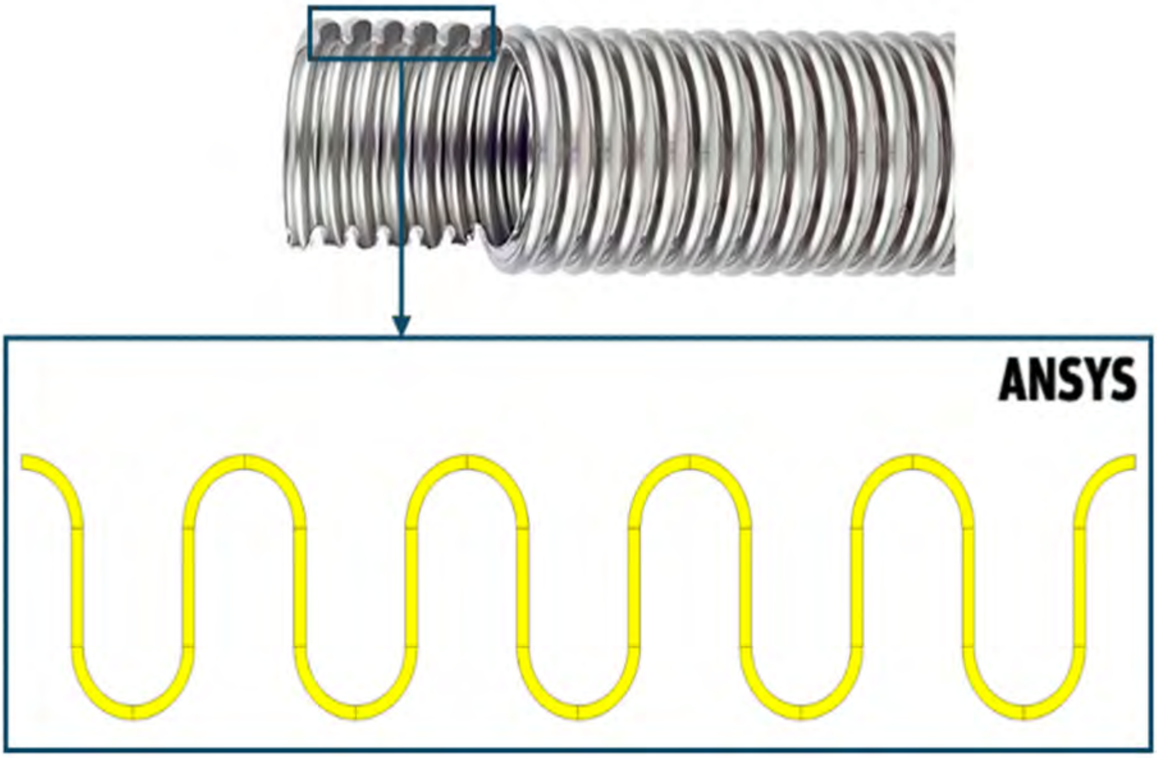

Figure 5.6: 2D axial-symmetric model of the transverse section of the corrugate.

The material is stainless steel, treated as linear elastic, with an elastic modulus of 191 GPa, a yield strength of 350 MPa, a Poisson's ratio of 0.28 and a total relative contraction of 2.8×10^{-3} over the whole temperature range. These values adequately represent the behaviour of the material under the expected operating conditions. Since the cryostat has a fixed length, the nodes at the ends of the model were constrained in order to reproduce this longitudinal constraint condition. The analysis was therefore divided into a series of distinct thermal and mechanical phases for the inner and outer corrugates, reflecting the fact that the two components operate at different temperatures and are subject to non-coinciding pressure conditions. For the inner corrugate, through which the hydrogen flows, the simulation first involves the cooling to 20 K, which introduces an initial state of tension in the structure. Subsequently, a pressure of 10 bar, corresponding to the pressure of the cryogenic fluid, is applied to the internal nodes, and a pressure of 10^{-5} bar is applied to the external nodes, simulating the vacuum condition outside. In this way, the actual operating conditions are reproduced, in which the inner tube must simultaneously withstand thermal contraction and the pressure differential between the inside and outside. In contrast, the outer corrugate maintains ambient temperature during operation and does not undergo a cooling phase. In this case, the simulation involves applying 10^{-5} bar to the internal nodes to simulate the vacuum condition, while applying a pressure of 4 bar to the outer surface, equal to the hydrostatic pressure at an operating depth of 30-40 metres below sea level.

The results shown in Fig. 5.7 and in Fig. 5.8 highlight that the inner corrugate is subject to the highest stress, due to the combination of thermal contraction and internal pressure, while the outer one is subject to less stress because it does not undergo the thermal cycle and only bears hydrostatic pressure. In both cases, the stresses obtained (with peak stress on the inner corrugate 123 MPa and on the outer one 56.2 MPa) remain below the material's resistance limits, confirming the compatibility of the planned configuration with the operating conditions.

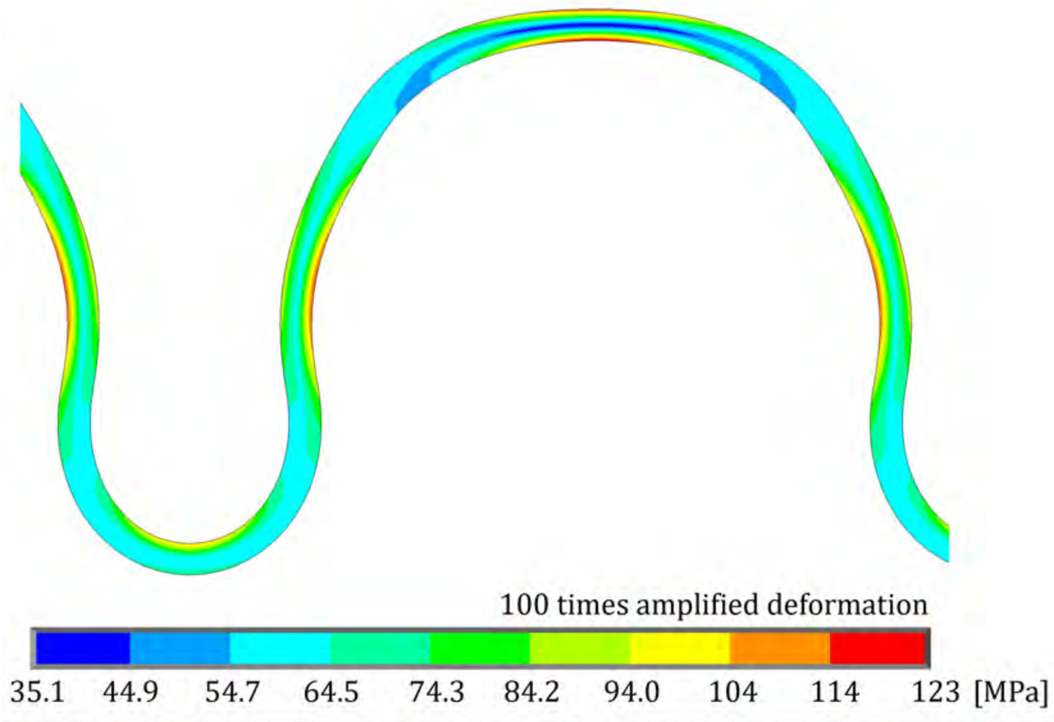

Figure 5.7: Von Mises Stress on the inner corrugated tube. The deformations are 100 times amplified to highlight the type of deformation.

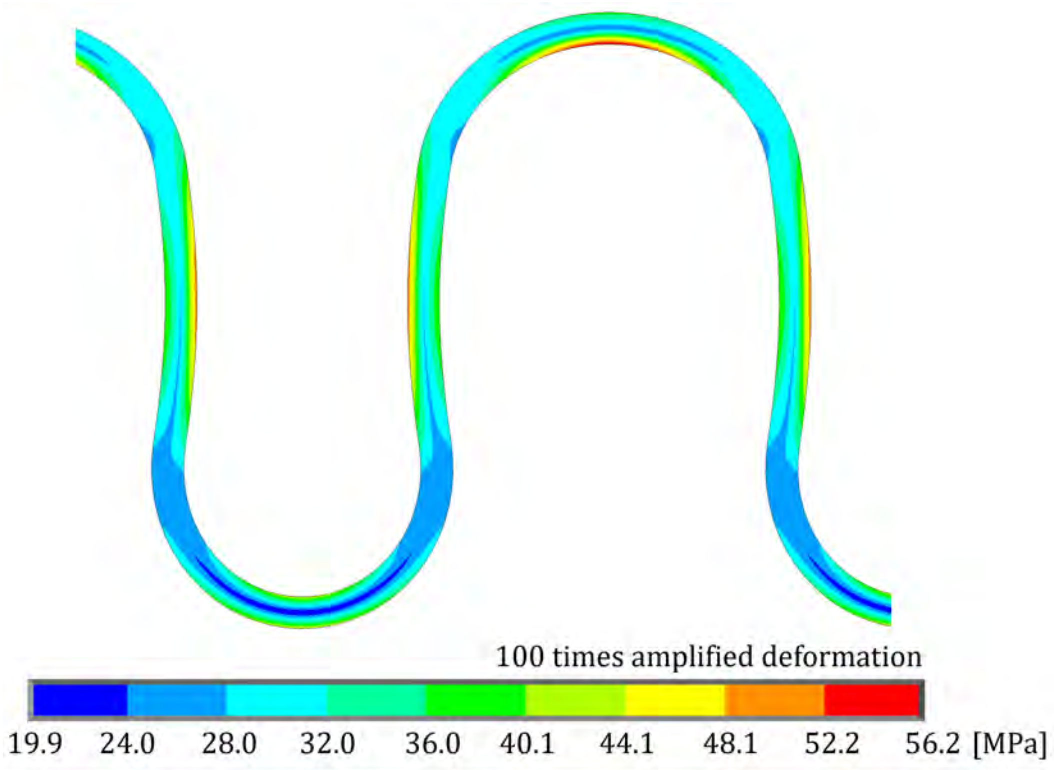

Figure 5.8: Von Mises Stress on the outer corrugated tube. The deformations are 100 times amplified to highlight the type of deformation.

With regard to the evaluation of the overall thermal contraction of the system, this can be referred exclusively to the cable, since the corrugated geometry of the inner tube is designed precisely to compensate for the variations in length that occur during the cooling process. The primary function of the cryostat model is to verify the structural resistance to the set of loads under consideration, while the quantification of shrinkage along the section is delegated to a dedicated cable model.

5.3.2 Analysis of the superconducting cable

The superconducting cable was modelled using a three-dimensional approach, employing ANSYS APDL and the SOLID186 element, which is suitable for representing the deformation of complex geometries subject to thermal and mechanical loads. The construction of the model required the explicit definition of the actual structure of the conductor, shown in Fig. 5.9, including the MgB_2 strands, the copper core and the various insulating layers. Particular attention was paid to the representation of the twisted configuration of the strands, as the winding pitch introduces a mechanical coupling that directly affects the distribution of deformations along the cable.

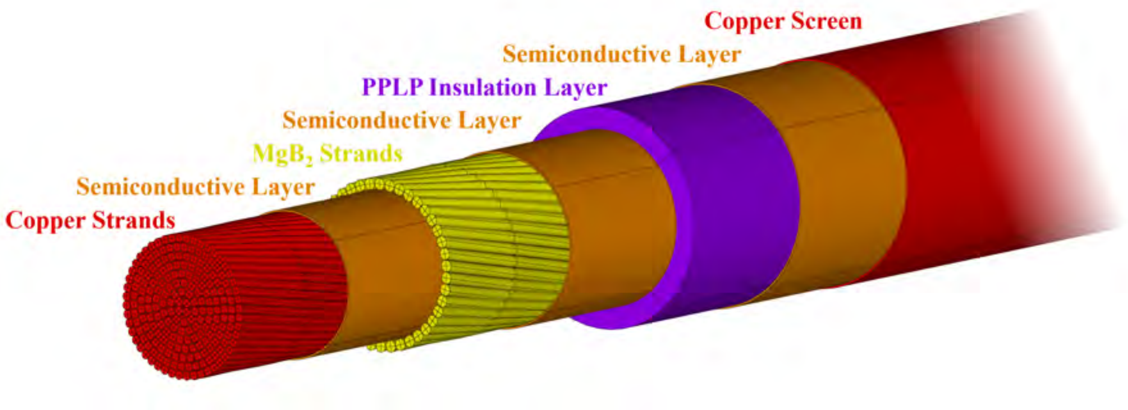

Figure 5.9: Geometry of the superconducting cable in the ANSYS model.

The definition of the material properties necessitated the formulation of certain assumptions, particularly in the case of MgB_2. While experimental values of the Young's modulus for MgB_2 are available from measurements on real wires [62], information on the thermal contraction of the specific wire used in this work was not provided. Consequently, the thermal expansion behaviour was estimated using the coefficient of the Monel matrix, which represents the predominant component of the wire, under the assumption that it has the most significant influence on the longitudinal contraction during the cooling process. This choice provides a reasonable approximation of the thermal behaviour of the conductor within the limits imposed by the available information. The simulation models the cooldown of the conductor from room temperature to the operating temperature of about 29 K. To accurately reflect the cable's configuration post-installation, where both ends are constrained, one terminal section of the model is fixed, while the opposing end is constrained to move as a rigid body. This approach prevents differential displacements among the nodes of the end section and makes it possible to measure the overall shortening of the cable in a consistent manner, in line with the actual anchoring conditions. The different thermal expansion coefficients of the materials involved result in a non-uniform contraction, which manifests as both localised stress concentrations in the MgB_2 filaments and as an overall axial deformation that defines the cable's shrinkage. For a half-twist pitch of 150 mm, the model yields a longitudinal shortening of 0.041 mm, shown in Fig. 5.10. When extrapolated to the full 30 km length of the line, this corresponds to a total shortening of approximately 8 m.

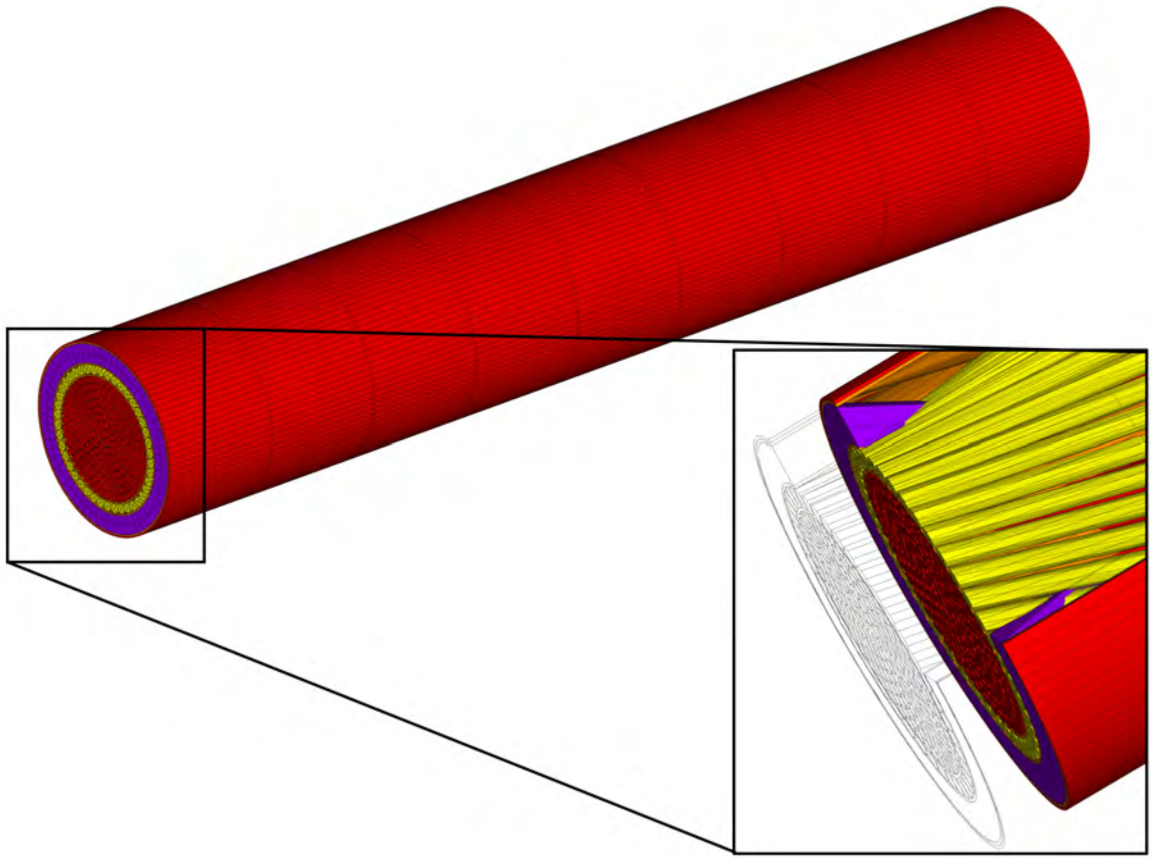

Figure 5.10: Full model of the cable with a zoom on the end to highlight the shortening due to cooling.

During the project, a configuration without the copper core was also analysed, and a second three-dimensional model was developed using the same methodology (Fig. 5.11). This option was considered to explore alternative design solutions, although it was later discarded for reasons related to the electrical protection of the system, as discussed in the previous chapters. The analysis nevertheless made it possible to quantify how the absence of the internal support affects the axial deformation. In fact, without the copper core, the total shrinkage decreases to about 5 m, showing that the central support contributes significantly to the longitudinal stiffness of the conductor.

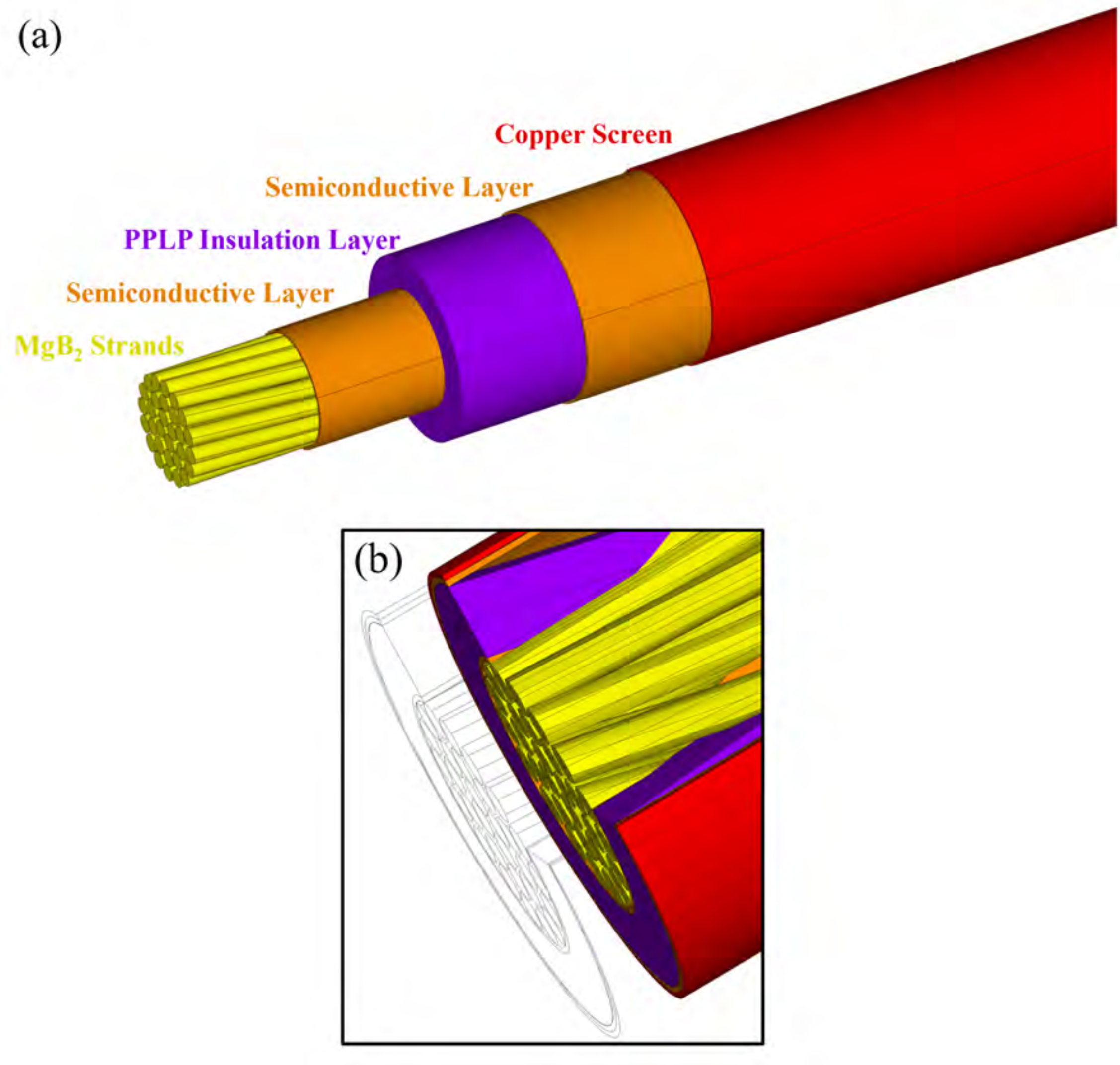

Figure 5.11: (a) Layout of the superconducting cable without the copper former in the ANSYS model with (b) a zoom on the shortening due to cooling.

Alongside the complete models, a simplified model was also developed to reduce the computational time. In this version, the copper core is represented as a solid cylinder and the internal structure is not modelled in detail (Fig. 5.12). This results in a higher axial stiffness compared with the real configuration. Consequently, the overall shortening is underestimated and the calculated shrinkage is reduced to values of the order of 1 metre. Although this model is not suitable for the final assessment of deformations or internal stresses, it is useful for obtaining quick estimates and for evaluating the effect of preliminary modifications to the cable configuration.

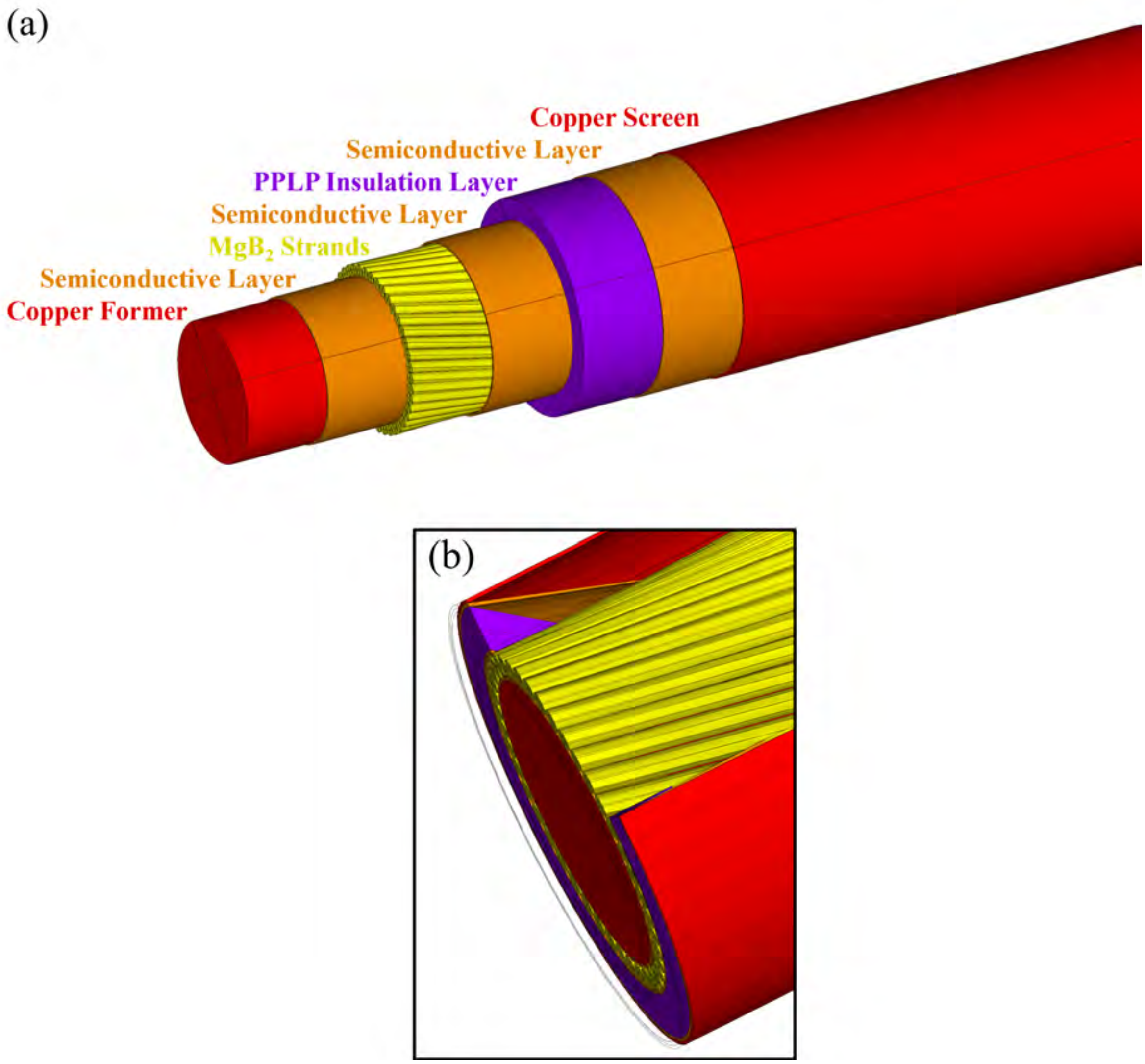

Figure 5.12: (a) Layout of the simplified superconducting cable with the solid cilindric copper former in the ANSYS model with (b) a zoom on the shortening due to cooling.

The three-dimensional model remains the reference tool for the thermo-mechanical characterisation of the conductor, as it allows both the overall deformation of the wire and the onset of local stresses along the section to be described. This is particularly useful for verifying that the stress and strain state generated on the MgB_2 wire due to cooling falls within the known irreversible limits for ex-situ MgB_2 conductors. As demonstrated in Fig. 5.13, the simulations indicate maximum Von Mises stress values of 30.6 MPa and a maximum equivalent strain of 0.0185%. These values are well below the thresholds identified in the literature as the onset of wire performance degradation [62], [130]. Consequently, there is no risk to the mechanical integrity of the filaments or to the maintenance of superconducting properties.

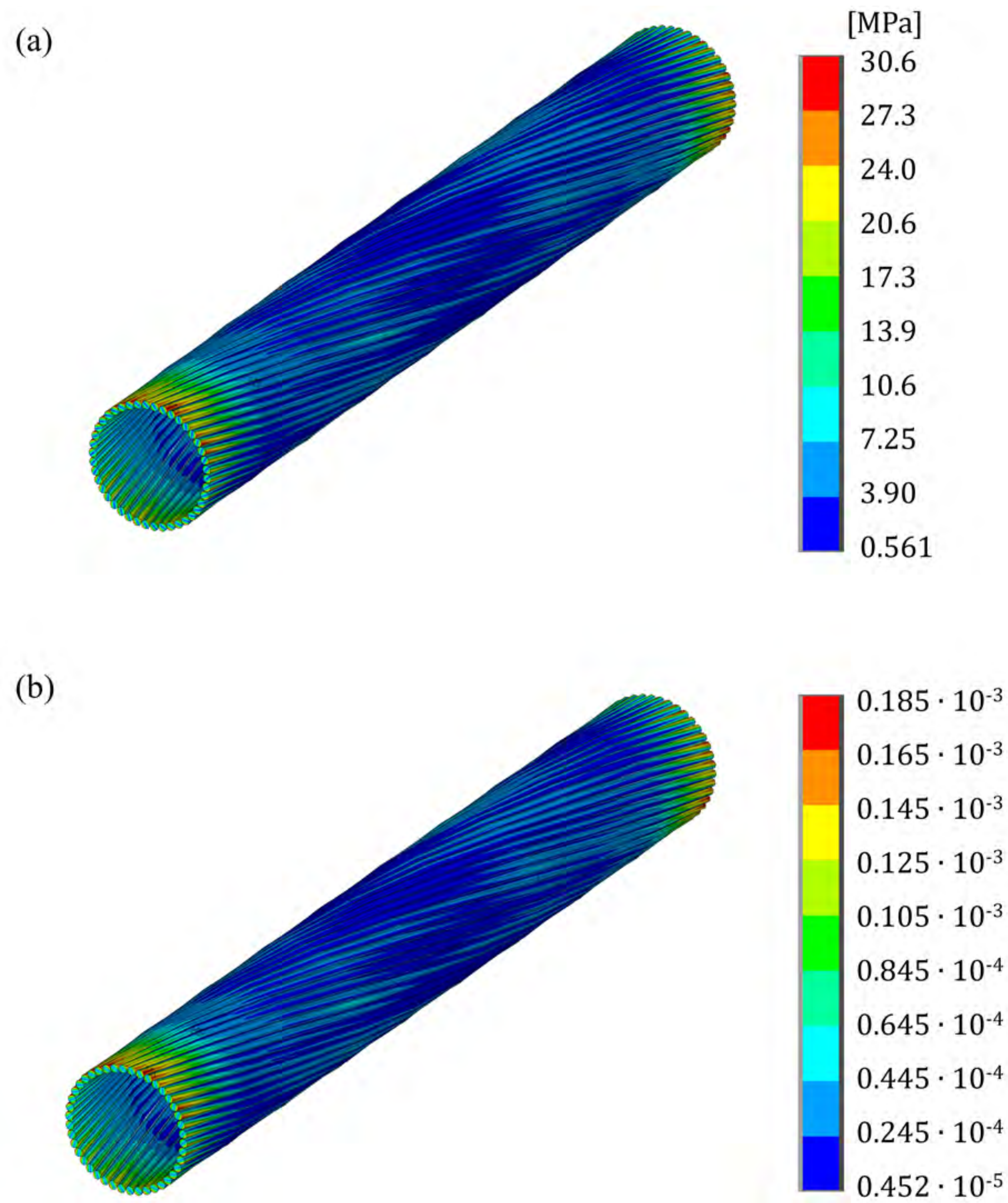

Figure 5.13: Von Mises stress (a) and strain (b) for the MgB_2 strands of the cable in the approved configuration.

Overall, the detailed model offers the most reliable basis for estimating the manufacturing length of the cable and for checking the compatibility between the conductor and the rigid components of the system.

Chapter 6

Conclusions

In this thesis, the finite element method (FEM) numerical modelling was used to analyse the mechanical behaviour of two superconductors intended for cutting-edge technological applications: multifilamentary Nb3Sn wires for the construction of high-field magnets for particle accelerators, and MgB2 cables within the Tricheco project, an underwater energy infrastructure integrating direct current power transmission and liquid hydrogen transport. Despite their differences in application domains, both research areas share the need to understand the role of mechanical stresses and severe operating conditions on conductor performance. They also demonstrate the effectiveness of finite element analysis in investigating phenomena that are difficult to characterise using experimental measurements alone, due to the complexity of the conditions to be reproduced and the costs associated with large-scale testing campaigns.

6.1 Nb_3Sn wire model

In the case of Nb_3Sn wires in the unreacted state, two-dimensional modelling has made it possible to quantitatively describe the effects of strain induced by cabling. A comparison between the idealised geometry and that obtained from SEM micrographs highlighted the importance of considering the actual conductor architecture in order to accurately reproduce the local stress distribution and identify the regions most sensitive to sub-element distortion. At the same time, the model based on the idealised geometry proved to be a useful tool for exploring hypothetical configurations and design scenarios not accessible experimentally, enabling parametric analyses of the wire's mechanical response and providing a methodological basis for the study of future multifilamentary layouts. These results help to understand how the deformations introduced during the pre-heat treatment phase can alter the internal architecture of the wire and subject certain sub-elements to high stress and strain, conditions that may lead to damage to the barriers or the matrix, with consequences for the RRR and the performance of the conductor. Alongside the study of the unreacted wire, a preliminary model of the reacted wire configuration was developed, with the aim of providing a numerical basis for future analyses of the conductor's behaviour following heat treatment.

Possible future developments of this work include, first and foremost, a refinement of the mechanical characterisation of the materials, with the aim of obtaining a more accurate estimate of the tangent moduli and plastic properties that have not yet been measured experimentally. A refinement of the constitutive parameters would make it possible to reduce the model's uncertainty and to describe more accurately the wire's response to the stresses introduced during cabling. In parallel with this, it will be important to extend the analysis to different wire architectures, in order to understand how changes in the internal arrangement of the sub-elements influence local deformation and stress distribution. An evaluation of these solutions would facilitate a determination of the layouts that are more robust both against the deformations introduced by cabling and under transverse loads in the reaction-supported configuration. The analysis of the wire architecture is complemented by the opportunity to investigate the effect of wire diameter and variations in the Cu/non-Cu ratio. These are parameters that could influence the distribution of deformation and the ability of copper to absorb stresses during wiring and under transverse pressure. The width of the copper channels between sub-elements also requires dedicated evaluation, as it has been identified in previous studies as a factor capable of altering the localisation of stresses and the sub-elements' susceptibility to distortion [79]. The ability to explore geometric parameters such as layout, diameter, Cu/non-Cu ratio or the width of the copper channels through simulations allows for the evaluation of alternative design scenarios without having to physically produce new wires. This process reduces time and costs, and enables the preliminary identification of the most promising solutions to be verified experimentally.

From a modelling perspective, a particularly significant extension involves modelling the heat-treated wire directly from the deformed geometry of the untreated wire obtained from the simulations. This approach would enable the analysis of the conductor's response following heat treatment on a geometric basis consistent with the actual process.

A further advancement concerns the integration of the mechanical model with the electromagnetic model, incorporating into the model the relationship between the stress state and the critical current, thereby establishing a quantitative link between the deformations induced in the wire and the variation in the parameter I_c. This would facilitate a more detailed description of the relationship between mechanical stresses and electromagnetic performance.

Finally, the extension of the modelling to sets of wires in a Rutherford configuration, as analysed in relevant studies [131], [132], represents a significant step towards a more realistic description of the collective response of the cable. This allows for the analysis of the effects of mechanical contact between wires, distributed transverse pressure and deformation under typical operating conditions of accelerator magnets.

6.2 The TRICHECO project

The second study focused on the MgB_2 cable intended for the 30 km hybrid pipeline of the Tricheco project, which connects an offshore energy hub based on renewable sources to the onshore grid and incorporates the transport of liquid hydrogen. In this architecture, liquid hydrogen fulfils a dual role, serving as both an energy carrier and providing the cryogenic conditions essential for the operation of the superconducting cable, which requires operating temperatures ranging from 20 to 29 K. The thermo-mechanical conditions imposed by the underwater environment and the pipeline's operation generate a complex stress state, where thermal contraction, external hydrostatic pressure, and restrictions on longitudinal movement resulting from the line's geometry all contribute to determining the response of the cable and the cryostat. Finite element analysis has made it possible to quantify these effects, describing the stress distribution in the main components and providing an estimate of the cable shortening over kilometre-scale lengths. This longitudinal contraction is a critical parameter for determining the effective installation length of the cable: an insufficient allowance would place the line under tensile load, with the risk of mechanical failure along the infrastructure.

Based on the results obtained, there are numerous opportunities to further develop this work. The construction of a small-scale demonstrator would provide an experimental platform for verifying the thermo-mechanical analyses and, at the same time, for evaluating the electrical, electromagnetic and fluid-dynamic aspects identified by the modelling. This would offer comprehensive validation of the various components of the hybrid system. However, its realisation would necessarily have to take into account the constraints and operational challenges associated with the use of liquid hydrogen in the system.

Completing the mechanical model of the conductor under operating conditions will require the integration of residual cable stresses and Lorentz forces, in order to describe the actual stress state during operation. In this context, the ability to couple thermo-hydraulic modelling of fault transients with structural analyses would allow for the evaluation of the impulse stresses generated by the rapid temperature variations typical of accident scenarios. Extending this approach to the study of thermal fatigue during repeated cooling and heating cycles would represent a significant step towards accurately determining the robustness and overall service life of the entire system.

6.3 Final Considerations

The two studies included in this thesis demonstrate the importance of finite element modelling in understanding the behaviour of technical superconducting conductors in critical applications and in supporting the design process of systems based on such materials. In the case of Nb_3Sn, the finite element method (FEM) allows for a detailed analysis of the effects of mechanical deformation associated with cabling and the role it plays in defining the geometric configuration on which the conductor's performance depends. In the case of MgB_2, thermo-mechanical modelling is a valuable tool that can be used to assess the feasibility and reliability of a hybrid energy pipeline, in which direct current power transmission is integrated with the cryogenic transport of liquid hydrogen. The work carried out provides a solid foundation for extending numerical models towards a more comprehensive description of the mechanical and electromagnetic phenomena governing the operation of superconducting conductors, and for their application in advanced technologies for high-energy physics and the energy networks of the future.

Appendix

Solid Mechanics

1. Stress and strain: fundamental definitions

When a force acts on a solid body, it is never applied at a single point, but is always distributed over an area, however small. Stress is defined as the intensity with which this force acts on a surface:

$$\sigma = \frac{F}{A}. \tag{6.1}$$

In the International System, stress is measured in pascals (Pa), where $1\,\mathrm{Pa} = 1\,\mathrm{N/m^2}$.

Strain, on the other hand, is a measurement of the relative change in length (small-strain regime):

$$\varepsilon = \frac{\Delta L}{L_0}. \tag{6.2}$$

The relationship between stress and strain depends on the material and the region of the σ–ε diagram (6.1) in which we are located. In the elastic region, for small strains, the linear relationship holds:

$$\sigma = E\varepsilon, \tag{6.3}$$

where E is the Young's modulus.

2. σ–ε diagram

The σ–ε diagram provides fundamental information about the mechanical properties of a material. For ductile materials (6.1), the curve shows an elastic region followed by a plastic region. The point at which the material transitions from one region to the other is is defined as the yield strength σ_Y. Once this value is exceeded, the material will no longer return to its original length once the stress is removed.

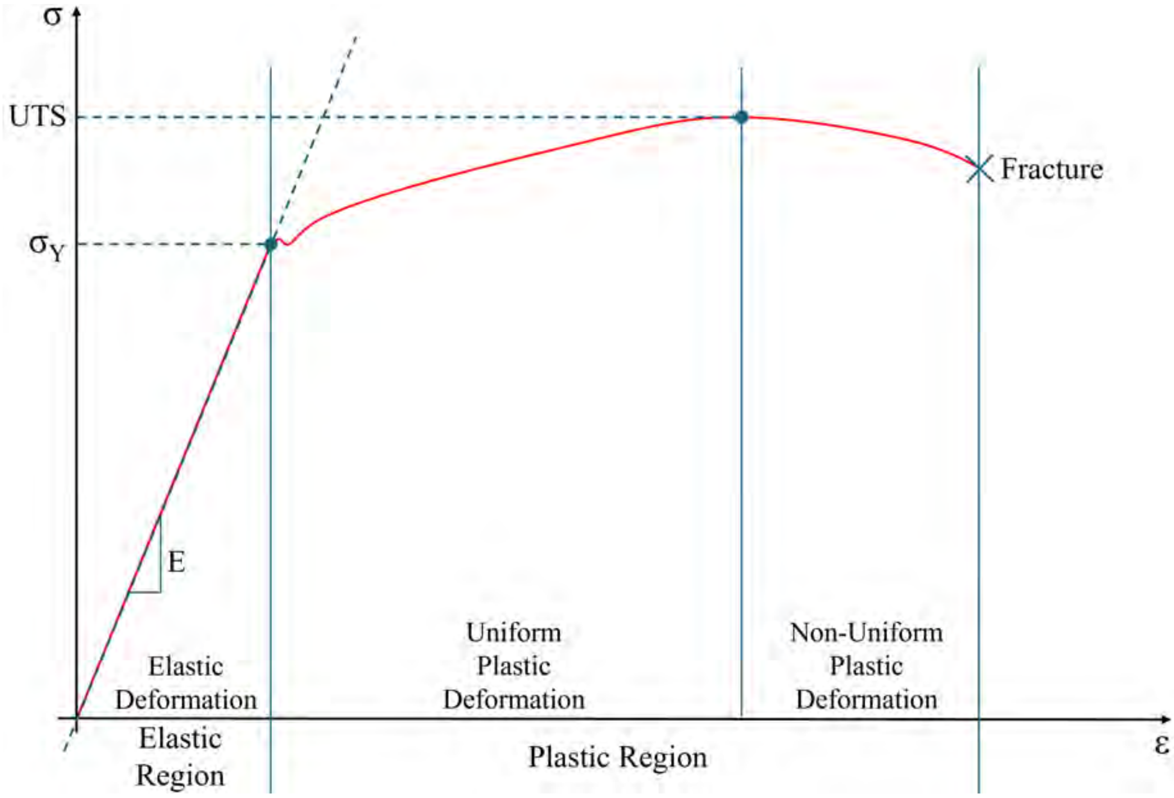

Figure 6.1: Representation of a stress-strain curve for a ductile material.

As the load on the material is further increased, a strain-hardening phase is observed, followed by the material reaching its ultimate tensile strength (UTS). Beyond this point, deformation localisation (necking) begins, culminating in fracture. In contrast, brittle materials fracture immediately after the elastic region, without exhibiting any significant plastic behaviour.

3. Stress tensor

To provide a more comprehensive overview of stress states, it is essential to consider the influence of surface orientation on stress levels. Therefore, the local stress state at a given point is described by the Cauchy tensor σ_{ij}:

$$t_i = \sigma_{ij} n_j, \tag{6.4}$$

where t_i is the traction acting on a plane with normal n_j.

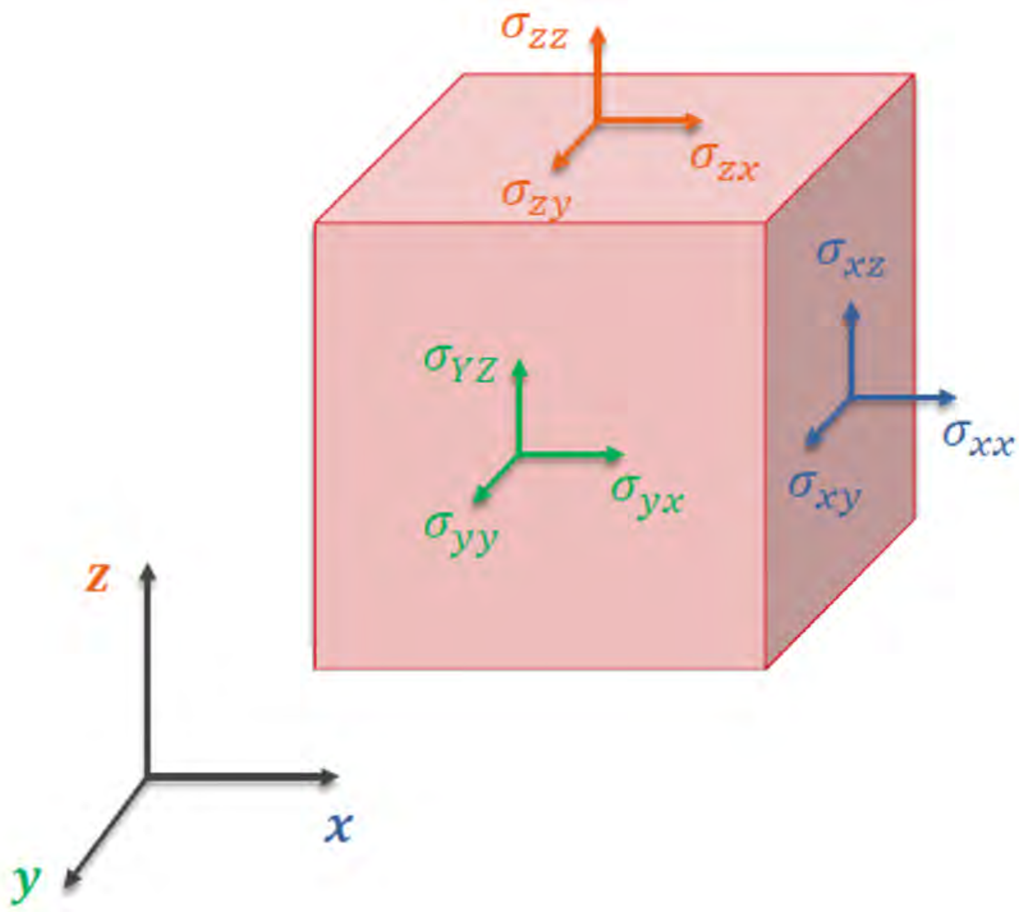

Figure 6.2: Schematic representation of the geometric interpretation of the stress tensor components.

The stress tensor is symmetric:

$$\sigma_{ij} = \sigma_{ji}, \tag{6.5}$$

as a consequence of angular momentum conservation. In matrix form:

$$\sigma = \begin{bmatrix} \sigma_{xx} & \sigma_{xy} & \sigma_{xz} \\ \sigma_{xy} & \sigma_{yy} & \sigma_{yz} \\ \sigma_{xz} & \sigma_{yz} & \sigma_{zz} \end{bmatrix}. \tag{6.6}$$

The diagonal components represent normal stresses, while the off-diagonal components correspond to shear stresses.

4. Principal stresses and invariants of the stress tensor

Since σ_{ij} there is always an orthonormal basis in which the tensor becomes diagonal. The eigenvalues of the matrix correspond to the principal stresses:

$$\sigma' = \begin{bmatrix} \sigma_1 & 0 & 0 \\ 0 & \sigma_2 & 0 \\ 0 & 0 & \sigma_3 \end{bmatrix}, \qquad \sigma_1 > \sigma_2 > \sigma_3. \tag{6.7}$$

These stresses correspond to pure normal stresses acting on surfaces oriented in such a way that the shear components vanish. The maximum stress in absolute value is usually associated with σ_1, whereas σ_3 typically represents the compressive state.

The principal stresses σ_1, σ_2 and σ_3 naturally emerge as the roots of the characteristic equation of the stress tensor:

$$\det(\sigma - \lambda I) = 0, \tag{6.8}$$

which can be equivalently expressed as a cubic polynomial:

$$\lambda^3 - I_1\lambda^2 + I_2\lambda - I_3 = 0. \tag{6.9}$$

The coefficients of this polynomial are the invariants of the stress tensor:

$$I_1 = \sigma_1 + \sigma_2 + \sigma_3, \; I_2 \qquad = \sigma_1\sigma_2 + \sigma_2\sigma_3 + \sigma_1\sigma_3, \; I_3 = \sigma_1\sigma_2\sigma_3. \tag{6.10}$$

These invariants remain unchanged under orthogonal transformations and thus provide an objective, frame-independent characterization of the stress state. In terms of the components of the stress tensor σ_{ij}, they can be written as:

$$I_1 = \mathrm{tr}(\sigma) = \sigma_{xx} + \sigma_{yy} + \sigma_{zz}, \tag{6.11}$$

$$I_2 = \sigma_{xx}\sigma_{yy} + \sigma_{yy}\sigma_{zz} + \sigma_{zz}\sigma_{xx} - (\sigma_{xy}^2 + \sigma_{xz}^2 + \sigma_{yz}^2) = \frac{1}{2}\left[(\mathrm{tr}\sigma)^2 - \mathrm{tr}(\sigma^2)\right], \tag{6.12}$$

$$I_3 = \det(\sigma). \tag{6.13}$$

The invariant I_1 represents the sum of the principal stresses and provides an overall measure of the intensity of the stress state, whereas I_2 and I_3 provide information related to the distortional behavior and the global characteristics of the stress field.

5. Hydrostatic–deviatoric decomposition

To distinguish the components of the stress state associated with volumetric changes from those responsible for distortional effects, the stress tensor can be decomposed into a hydrostatic part $p\delta_{ij}$ and a deviatoric part s_{ij}:

$$\sigma_{ij} = p\delta_{ij} + s_{ij}, \qquad p = \frac{1}{3}\sigma_{kk}. \tag{6.14}$$

The hydrostatic part $p\delta_{ij}$ acts uniformly on the material, compressing or expanding it without altering its shape. In contrast, the deviatoric part s_{ij} is responsible for shear deformations, modifying the shape while preserving the volume.

By definition, the deviatoric stress tensor is traceless:

$$\sigma_{kk}^{dev} = 0. \tag{6.15}$$

This property identifies a purely distortional stress state, free of volumetric contribution, and is therefore associated with a state of pure shear. Consequently, the deviatoric tensor is directly linked to shape-changing deformations and shear stresses.

In matrix form:

$$s = \begin{bmatrix} \sigma_{xx} - p & \sigma_{xy} & \sigma_{xz} \\ \sigma_{xy} & \sigma_{yy} - p & \sigma_{yz} \\ \sigma_{xz} & \sigma_{yz} & \sigma_{zz} - p \end{bmatrix}. \tag{6.16}$$

The deviatoric tensor shares the same eigenvectors as σ_{ij}. Its characteristic polynomial introduces the deviatoric invariants:

$$\det(s_{ij} - \lambda\delta_{ij}) = -\lambda^3 + J_1\lambda^2 + J_2\lambda + J_3 = 0. \tag{6.17}$$

with:

$$J_1 = \mathrm{tr}(s) = 0, \tag{6.18}$$

$$J_2 = \frac{1}{2}s_{ij}s_{ij}, \tag{6.19}$$

$$J_3 = \det(s). \tag{6.20}$$

The secondo deviatoric invariant J_2 plays a fundamental role in yield criteria for ductile materials.

6. Strain tensor

In analogy with the stress state, the strain state can also be described by a tensor. For small displacements, the strain tensor is defined as:

$$\varepsilon_{ij} = \frac{1}{2}\left(\frac{\partial u_i}{\partial x_j} + \frac{\partial u_j}{\partial x_i}\right). \tag{6.21}$$

In this case as well, the strain tensor can be decomposed into a volumetric part and a deviatoric part:

$$\varepsilon_{ij} = \frac{1}{3}\varepsilon_{kk}\delta_{ij} + e_{ij}. \tag{6.22}$$

7. Elasticity and Hooke's law

In the linear elastic regime, the constitutive relation between stress and strain is expressed in the general form:

$$\sigma_{ij} = C_{ijkl}\varepsilon_{kl}, \tag{6.23}$$

where C_{ijkl} is a fourth-order tensor which, in general, contains 81 components. Due to symmetry considerations, the number of independent components reduces to 36, similarly to stress σ and strain ε, which can each be represented by 6 components. In the case of hyperelastic materials, for which an elastic potential can be defined, the number of independent components further reduces to 21.

For isotropic and homogeneous materials, the elastic response is fully determined by two independent parameters: the Young's modulus E and Poisson's ratio ν. The isotropic Hooke's law can be written in its direct form:

$$\sigma_{ij} = \frac{E}{1+\nu}\left[\varepsilon_{ij} + \frac{\nu}{1-2\nu}\varepsilon_{kk}\delta_{ij}\right], \tag{6.24}$$

or in its inverse form:

$$\varepsilon_{ij} = \frac{1+\nu}{E}\sigma_{ij} - \frac{\nu}{E}\sigma_{kk}\delta_{ij}. \tag{6.25}$$

By employing the hydrostatic–deviatoric decomposition of stress and strain:

$$\sigma_{ij} = \frac{1}{3}\sigma_{kk}\delta_{ij} + s_{ij} \qquad \varepsilon_{ij} = \frac{1}{3}\varepsilon_{kk}\delta_{ij} + e_{ij} \tag{6.26}$$

the deviatoric e_{ij} and hydrostatic ε_{kk} components are obtained as:

$$e_{ij} = \frac{1+\nu}{E}s_{ij} \qquad \varepsilon_{kk} = \frac{1-2\nu}{E}\sigma_{kk} \tag{6.27}$$

In this formulation, the deviatoric part of the strain is proportional to the deviatoric part of the stress and describes shear deformations, while the hydrostatic part of the strain depends solely on the trace of the stress and accounts for volumetric changes in the material.

Finally, Poisson's ratio ν can be interpreted operationally, under uniaxial loading, as the ratio between the transverse contraction and the longitudinal extension:

$$\nu = -\frac{\varepsilon_{transversal}}{\varepsilon_{longitudinal}}. \tag{6.28}$$

For computational convenience, Hooke's law can also be expressed in terms of the Lamé parameters λ and G, which are defined from the engineering constants E and ν come:

$$G = \frac{E}{2(1+\nu)}, \qquad \lambda = \frac{E\nu}{(1+\nu)(1-2\nu)}. \tag{6.29}$$

The parameter G represents the shear modulus and provides the direct proportionality between deviatoric stresses and deviatoric strains:

$$s_{ij} = 2Ge_{ij}. \tag{6.30}$$

8. Thermal contraction

A temperature change induces an isotropic strain that superimposes onto the mechanical strains:

$$\varepsilon_{ij}^{th} = \alpha(T)\Delta T\,\delta_{ij}. \tag{6.31}$$

where α is the thermal expansion coefficient, defined as:

$$\alpha = \frac{1}{V}\left(\frac{\partial V}{\partial T}\right)_P. \tag{6.32}$$

For materials operating at temperatures significantly lower than room temperature, the total contraction from T_{RT} to T_{op} is:

$$\frac{\Delta L}{L} = \int_{T_{RT}}^{T_{op}} \alpha(T)\,dT. \tag{6.33}$$

In composite materials (such as superconducting wires), the mismatch between the thermal contraction coefficients of the different constituents generates differential thermal strains:

$$\Delta\varepsilon_{th} = (\alpha_m - \alpha_f)\Delta T, \tag{6.34}$$

which generate residual stresses that can significantly affect the performance of the conductors.

9. Yield and Von Mises criterion

In the linear elastic regime, the elastic strain energy density is defined as:

$$U = \frac{1}{2}\sigma_{ij}\varepsilon_{ij}. \tag{6.35}$$

By exploiting the volumetric–deviatoric decomposition, the energy can be separated into the contributions:

$$U = U_{hydro} + U_{dev}, \quad \text{con } U_{dev} = \frac{1+\nu}{2E}s_{ij}s_{ij}. \tag{6.36}$$

Since the hydrostatic component of the energy is associated exclusively with volumetric changes, it does not contribute to yielding in ductile materials. It follows that the yield condition depends solely on the deviatoric part of the stress state and is therefore linked to the second deviatoric invariant J_2.

On this basis, the von Mises criterion states that yielding begins when J_2 reaches a critical value characteristic of the material. To determine this value, the experimental case of uniaxial tension along the z-axis is considered. In this configuration, the principal stresses are:

$$\sigma_1 = \sigma, \quad \sigma_2 = 0, \quad \sigma_3 = 0. \tag{6.37}$$

and the trace of the stress tensor is $\sigma_{kk} = \sigma$.

By subtracting the hydrostatic component, the principal deviatoric stresses are obtained:

$$s_i = \sigma_i - \frac{1}{3}\sigma_{kk} \quad \Rightarrow \quad s_1 = \frac{2}{3}\sigma, \quad s_2 = -\frac{1}{3}\sigma, \quad s_3 = -\frac{1}{3}\sigma. \tag{6.38}$$

The second deviatoric invariant therefore becomes:

$$J_2 = \frac{1}{2}(s_1^2 + s_2^2 + s_3^2) = \frac{1}{3}\sigma^2. \tag{6.39}$$

When the uniaxial stress σ reaches the yield value σ_Y, the invariant attains its critical value:

$$J_{2,\text{crit}} = \frac{1}{3}\sigma_Y^2. \tag{6.40}$$

To generalize the yield criterion to a three-dimensional stress state, the von Mises equivalent stress σ_{VM}, is introduced, a scalar quantity that represents the same distortional effect as a uniaxial load:

$$\sigma_{VM} = \sqrt{3J_2}, \tag{6.41}$$

and in the uniaxial case it follows that $\sigma_{VM} = \sigma$, in agreement with the experimental observation. For a general stress state, expressed in terms of the principal stresses, the most common form is:

$$\sigma_{VM} = \sqrt{\frac{(\sigma_1 - \sigma_2)^2 + (\sigma_1 - \sigma_3)^2 + (\sigma_2 - \sigma_3)^2}{2}}. \tag{6.42}$$

The von Mises yield condition can therefore be expressed as a safety check:

$$\sigma_{VM} \leq \sigma_Y, \tag{6.43}$$

which represents the material's yield surface in the three-dimensional principal stress space, namely the set of all possible combinations of σ_1, σ_2 e σ_3 for which the material begins to deform plastically. In practice, the von Mises criterion makes it possible to predict the onset of plasticity even under multiaxial loading conditions, since it reduces any complex stress state to a single scalar value σ_{VM} that quantifies the intensity of the distortion.

10. Total deformation

In the presence of different sources of deformation, the total strain can be decomposed into elastic, plastic, residual, and thermal contributions:

$$\varepsilon_{ij}^{tot} = \varepsilon_{ij}^{el} + \varepsilon_{ij}^{pl} + \varepsilon_{ij}^{res} + \varepsilon_{ij}^{th}. \tag{6.44}$$

Since only the elastic component contributes to the stress state, the constitutive relation can be expressed as

$$\sigma_{ij} = 2G\varepsilon_{ij}^{el} + \lambda\varepsilon_{kk}^{el}\delta_{ij}. \tag{6.45}$$

where G and λ are the Lamé parameters.

Bibliography

[1] M. Bracco, J. Bijlsma, J. Baumann, *et al.*, "Numerical Analysis of Unreacted Nb_3Sn Wires Under Compression," *IEEE Transactions on Applied Superconductivity*, vol. 36, no. 5, 2026. DOI: 10.1109/TASC.2026.3659580.

[2] M. Bracco, A. Balbo, C.-E. Bruzek, *et al.*, "Design of a Submarine 30-km MgB_2 Cable for the Combined Transfer of 0.3 GW_e and LH_2 from Offshore Plants to the Ravenna Port," *IEEE Transactions on Applied Superconductivity*, vol. 35, no. 5, 2025. DOI: 10.1109/TASC.2025.3528923.

[3] P. Seidel, *Applied Superconductivity: Handbook on Devices and Applications*. John Wiley & Sons, Incorporated, 2015. DOI: 10.1002/9783527670635.

[4] P. J. Lee, "Superconducting wires and cables: Materials and processing," in *Encyclopedia of Materials: Science and Technology*, Elsevier Ltd, 2011.

[5] J. V. Yakhmi, *Superconducting Materials and Their Applications*. IOP Publishing, 2021. DOI: 10.1088/978-0-7503-2256-0.

[6] M. N. Wilson, *Superconducting Magnets*. Oxford University Press, 1983.

[7] J. F. Annett, *Superconductivity, Superfluids and Condensates*. Oxford University Press, 2004.

[8] H. Ibach and H. Lüth, *Solid-State Physics - An Introduction to Principles of Materials Science*. Springer, 2009.

[9] G. Iannone, F. Quero, U. Gambardella, P. Fabbricatore, S. Farinon, and G. Volpini, "Composite superconducting wires for fast ramped magnets," *Composites Part B: Engineering*, vol. 90, 2016. DOI: https://doi.org/10.1016/j.compositesb.2015.12.023.

[10] B. M. Maple, "A15 phases," *AccessScience*, 2024. DOI: 10.1036/1097-8542.000100.

[11] K. H. Matucha, Ed., *Materials Science and Technology, Volume 8, Structure and Properties of Nonferrous Alloys*, vol. 8, 1996.

[12] A. Godeke, "A review of the properties of Nb_3Sn and their variation with A15 composition, morphology and strain state," *Superconductor Science and Technology*, vol. 19, no. 8, Jun. 2006. DOI: 10.1088/0953-2048/19/8/R02.

[13] E. Barzi and A. V. Zlobin, "Research and development of wires and cables for high-field accelerator magnets," *IEEE Transactions on Nuclear Science*, vol. 63, no. 2, 2016. DOI: 10.1109/TNS.2015.2500440.

[14] D. Schoerling and A. V. Zlobin, *Nb_3Sn Accelerator Magnets : Designs, Technologies and Performance*, 1st ed. 2019. Springer Nature, 2019.

[15] L. Bottura and A. Godeke, "Superconducting materials and conductors : Fabrication and limiting parameters," *Reviews of Accelerator Science and Technology*, vol. 05, 2012. DOI: 10.1142/S1793626812300022.

[16] C. Scheuerlein, J. Andrieux, M. Michels, *et al.*, "Effect of the fabrication route on the phase and volume changes during the reaction heat treatment of nb_3sn superconducting wires," *Superconductor Science and Technology*, vol. 33, no. 3, Jan. 2020. DOI: 10.1088/1361-6668/ab627c.

[17] R. Flükiger, D. Uglietti, C. Senatore, and F. Buta, "Microstructure, composition and critical current density of superconducting Nb_3Sn wires," *Cryogenics*, vol. 48, no. 7, Jul. 2008. DOI: 10.1016/j.cryogenics.2008.05.005.

[18] J. Nagamatsu, N. Nakagawa, T. Muranaka, Y. Zenitani, and J. Akimitsu, "Superconductivity at 39 K in magnesium diboride," *Nature*, vol. 410, no. 6824, Mar. 2001. DOI: 10.1038/35065039.

[19] Inamuddin, *Superconductors : Materials and Applications.* (Materials Research Foundations ; v.132), 1st ed. Materials Research Forum LLC, 2022.

[20] C. Buzea and T. Yamashita, "Review of the superconducting properties of MgB_2," *Superconductor Science and Technology*, vol. 14, no. 11, Nov. 2001. DOI: 10.1088/0953-2048/14/11/201.

[21] M. Tropeano, L. Soldati, A. Ansaldo, *et al.*, "Progress in MgB_2 wires manufacturing at asg superconductors and perspective for applications," *IEEE Transactions on Applied Superconductivity*, vol. 35, no. 5, 2025. DOI: 10.1109/TASC.2024.3499965.

[22] A. Ballarino and R. Flükiger, "Status of MgB_2 wire and cable applications in europe," *Journal of Physics: Conference Series*, vol. 871, no. 1, Jul. 2017. DOI: 10.1088/1742-6596/871/1/012098.

[23] G. P. Willering, "Stability of superconducting rutherford cables for accelerator magnets," PhD Thesis - Research UT, graduation UT, University of Twente, Netherlands, May 2009. DOI: 10.3990/1.9789036528177.

[24] M. Wilson, "Superconducting magnets for accelerators: A review," *IEEE transactions on applied superconductivity*, vol. 7, no. 2, 1997.

[25] E. Barzi, N. Andreev, C. Boffo, *et al.*, "Development and study of rutherford-type cables for high-field accelerator magnets at fermilab," *Superconductor science technology*, vol. 17, no. 5, 2004.

[26] A. Devred, L. Bacquart, P. Bredy, *et al.*, "Interstrand resistance measurements on Nb_3Sn rutherford-type cables," *IEEE Transactions on Applied Superconductivity*, vol. 9, no. 2, 1999. DOI: 10.1109/77.783397.

[27] E. W. Collings, M. D. Sumption, M. A. Susner, *et al.*, "Influence of a stainless steel core on coupling loss, interstrand contact resistance, and magnetization of an Nb_3Sn rutherford cable," *IEEE Transactions on Applied Superconductivity*, vol. 18, no. 2, 2008. DOI: 10.1109/TASC.2008.921896.

[28] N. Andreev, E. Barzi, E. Borissov, *et al.*, "Development of rutherford-type cables for high field accelerator magnets at fermilab," *IEEE transactions on applied superconductivity*, vol. 17, no. 2, 2007.

[29] E. Barzi, R. Bossert, S. Caspi, *et al.*, "RRP Nb_3Sn strand studies for LARP," *IEEE Transactions on Applied Superconductivity*, vol. 17, no. 2, 2007. DOI: 10.1109/TASC.2007.899579.

[30] D. Dietderich and A. Godeke, "Nb_3Sn research and development in the USA – wires and cables," *Cryogenics*, vol. 48, no. 7, 2008, Special Issue: Low-Tc Superconducting Materials. DOI: https://doi.org/10.1016/j.cryogenics.2008.05.004.

[31] F. Maltini, "1 - The implications of climate change and energy security for global electricity supply: The Energy (R)evolution," in *Eco-Friendly Innovation in Electricity Transmission and Distribution Networks*, J.-L. Bessède, Ed., Oxford: Woodhead Publishing, 2015, pp. 3–45, ISBN: 978-1-78242-010-1. DOI: https://doi.org/10.1016/B978-1-78242-010-1.00001-X.

[32] A. Battaglini and S. Bätjer, "9 - reducing the environmental impacts of power transmission lines," in *Eco-Friendly Innovation in Electricity Transmission and Distribution Networks*, J.-L. Bessède, Ed., Oxford: Woodhead Publishing, 2015, pp. 183–198, ISBN: 978-1-78242-010-1. DOI: https://doi.org/10.1016/B978-1-78242-010-1.00009-4.

[33] F. Delfino, S. Bracco, and F. Pampararo, "2 - key performance indicators in assessing new technology for electricity transmission and distribution networks," in *Eco-Friendly Innovation in Electricity Transmission and Distribution Networks*, J.-L. Bessède, Ed., Oxford: Woodhead Publishing, 2015, pp. 47–63, ISBN: 978-1-78242-010-1. DOI: https://doi.org/10.1016/B978-1-78242-010-1.00002-1.

[34] S. Klöppel, A. Marian, C. Haberstroh, and C.-E. Bruzek, "Thermo-hydraulic and economic aspects of long-length high-power MgB_2 superconducting cables," *Cryogenics*, vol. 113, 2021. DOI: https://doi.org/10.1016/j.cryogenics.2020.103211.

[35] C. Bruzek, A. Allais, D. Dickson, N. Lallouet, K. Allweins, and E. Marzahn, "7 - Superconducting DC cables to improve the efficiency of electricity transmission and distribution networks: An overview," in *Eco-Friendly Innovation in Electricity Transmission and Distribution Networks*, J.-L. Bessède, Ed., Oxford: Woodhead Publishing, 2015, pp. 135–167. DOI: 10.1016/B978-1-78242-010-1.00007-0.

[36] C.-E. Bruzek, A. Marian, C. Creusot, M. Gammelsæter, and A. Allais, "High-power medium-voltage superconducting cables for Europe's energy transition," in *28th International Conference and Exhibition on Electricity Distribution 2025*, CIRED, Geneva, Switzerland: Zenodo, 2025. DOI: 10.5281/zenodo.17568703. [Online]. Available: https://hal.science/hal-05408326.

[37] F. Mimmi, E. Guerra, M. Simonazzi, A. Morandi, U. Melaccio, and C.-E. Bruzek, "Comparative Analysis of MgB_2 Cable Layouts for 1 GW Superconducting Transmission-Insights From the SCARLET Project," *IEEE transactions on applied superconductivity*, vol. 35, no. 5, 2025. DOI: 10.1109/TASC.2024.3520535.

[38] F. Grilli, A. Chervyakov, V. Zermeno, *et al.*, "Numerical modeling of MgB_2 conductors for high power AC transmission," *Physica C: Superconductivity and its Applications*, vol. 504, 2014. DOI: https://doi.org/10.1016/j.physc.2014.04.037.

[39] R. Wesche, A. Anghel, B. Jakob, G. Pasztor, R. Schindler, and G. Vécsey, "Design of superconducting power cables," *Cryogenics*, vol. 39, no. 9, 1999. DOI: https://doi.org/10.1016/S0011-2275(99)00098-3.

[40] P. Grant, "The SuperCable: dual delivery of chemical and electric power," *IEEE transactions on applied superconductivity*, vol. 15, no. 2, 2005. DOI: 10.1109/TASC.2005.849298.

[41] N. Magnusson, A. Allais, G. Angeli, *et al.*, "SCARLET - A European Effort to Develop HTS and MgB_2 Based MVDC Cables," *IEEE transactions on applied superconductivity*, vol. 34, no. 3, 2024. DOI: 10.1109/TASC.2023.3340646.

[42] C.-E. Bruzek and A. Marian, "Superconducting links for very high power transmission based on MgB_2 wires," in *2021 AEIT HVDC International Conference (AEIT HVDC)*, 2021. DOI: 10.1109/AEITHVDC52364.2021.9474597.

[43] A. Ballarino, "Development of superconducting links for the Large Hadron Collider machine," *Superconductor Science and Technology*, vol. 27, no. 4, 2014. DOI: 10.1088/0953-2048/27/4/044024.

[44] F. Schmidt and A. Allais, "Superconducting cables for power transmission applications - a review," in *Workshop on accelerator magnet superconductors. Proceedings*, Nexans-Superconducting Cable System, Hanover (Germany), 2004.

[45] M. Stemmle, F. Merschel, M. Noe, and A. Hobl, "AmpaCity - Installation of advanced superconducting 10 kV system in city center replaces conventional 110 kV cables," in *2013 IEEE International Conference on Applied Superconductivity and Electromagnetic Devices (ASEMD)*, IEEE, 2013, pp. 323–326. DOI: 10.1109/ASEMD.2013.6780785.

[46] K. Berger, G. Hajiri, A. Allais, *et al.*, "Progress of the SuperRail Project in Paris and Qualification Results of the 35 m Prototype HTS Cable System," in *4th International Workshop on Cooling Systems for HTS Applications (IWC-HTS)*, Cryogenics and Superconductivity Society of Japan (CSSJ), 2024. [Online]. Available: https://hal.science/hal-04752808.

[47] A. Allais, J.-M. Saugrain, B. West, *et al.*, "SuperRail–World-First HTS Cable to be Installed on a Railway Network in France," *IEEE Transactions on Applied Superconductivity*, vol. 34, no. 3, 2024. DOI: 10.1109/TASC.2024.3356450.

[48] S. Aboudrar, A. Allais, K. Allweins, *et al.*, "SuperRail - Current Status of the First Commercial HTS DC Cable System in a Railway Grid," in *Proceedings of the Symposium on Advanced Technologies in Electrical Systems - SATES 2025 (https://hal.science/SATES-2025)*, 2025. [Online]. Available: https://hal.science/hal-05065361.

[49] A. Ballarino, W. Bailey, C. Barth, *et al.*, "A system solution for a 100 kA class high temperature superconducting line for HL-LHC and for wider energy applications," *Scientific Reports*, vol. 15, no. 1, 2025. DOI: 10.1038/s41598-025-08543-9.

[50] T. Spina, A. Ansaldo, A. Tumino, *et al.*, "Recent Development and Status of Ex-Situ PIT MgB_2 Wires at ASG Superconductors," *IEEE transactions on applied superconductivity*, vol. 34, no. 3, 2024. DOI: 10.1109/TASC.2024.3353144.

[51] C. E. Bruzek, T. Spina, U. Melaccio, *et al.*, "MVDC MgB_2 superconducting cables for hybrid power transmission," in SEE, 2023. DOI: 10.5281/zenodo.10628423.

[52] C. E. Bruzek, T. Spina, U. Melaccio, *et al.*, "MgB_2-Based MVDC Superconducting Power Cable in Liquid Hydrogen for Hybrid Energy Distribution," *IEEE Transactions on Applied Superconductivity*, vol. 34, no. 3, 2024. DOI: 10.1109/TASC.2023.3347216.

[53] L. Trevisani, M. Fabbri, and F. Negrini, "Long distance renewable-energy-sources power transmission using hydrogen-cooled MgB_2 superconducting line," *Cryogenics (Guildford)*, vol. 47, no. 2, 2007. DOI: https://doi.org/10.1016/j.cryogenics.2006.10.002.

[54] L. Savoldi, A. Balbo, C. E. Bruzek, G. Grasso, M. Patti, and M. Tropeano, "Conceptual Design of a SuperConducting Energy Pipeline for LH2 and Power Transmission Over Long Distances," *IEEE Transactions on Applied Superconductivity*, vol. 34, no. 3, 2024. DOI: 10.1109/TASC.2024.3370123.

[55] V. S. Vysotsky, A. A. Nosov, S. S. Fetisov, *et al.*, "Hybrid Energy Transfer Line With Liquid Hydrogen and Superconducting MgB_2 Cable-First Experimental Proof of Concept," *IEEE transactions on applied superconductivity*, vol. 23, no. 3, 2013. DOI: 10.1109/TASC.2013.2238574.

[56] S. Yamada, Y. Hishinuma, T. Uede, *et al.*, "Conceptual design of 1 gw class hybrid energy transfer line of hydrogen and electricity," *Journal of physics. Conference series*, vol. 234, no. 3, 2010. DOI: 10.1088/1742-6596/234/3/032064.

[57] M. J. Cheadle, M. Wozniak, L. Bromberg, *et al.*, "DC Superconducting Cable Using MgB_2 Wires," *IEEE transactions on applied superconductivity*, vol. 23, no. 3, 2013. DOI: 10.1109/TASC.2013.2248313.

[58] C. E. Bruzek, A. Ballarino, G. Escamez, *et al.*, "Cable Conductor Design for the High-Power MgB_2 DC Superconducting Cable Project of BEST PATHS," *IEEE transactions on applied superconductivity*, vol. 27, no. 4, pp. 1–5, 2017. DOI: 10.1109/TASC.2016.2641338.

[59] M. Statera, S. Maffezzoli Felis, L. Canonica, *et al.*, "A Magnesium Diboride Test Line Rated 1 GW Conceptual Design," *IEEE transactions on applied superconductivity*, vol. 34, no. 3, 2024. DOI: 10.1109/TASC.2023.3341989.

[60] V. V. Kostyuk, I. V. Antyukhov, E. V. Blagov, *et al.*, "Experimental hybrid power transmission line with liquid hydrogen and MgB_2-based superconducting cable," *Technical physics letters*, vol. 38, no. 3, 2012. DOI: https://doi.org/10.1134/S106378501203025X.

[61] A. Ballarino, C. E. Bruzek, N. Dittmar, *et al.*, "The BEST PATHS Project on MgB_2 Superconducting Cables for Very High Power Transmission," *IEEE transactions on applied superconductivity*, vol. 26, no. 3, 2016. DOI: 10.1109/TASC.2016.2545116.

[62] K. Konstantopoulou, A. Ballarino, A. Gharib, *et al.*, "Electro-mechanical characterization of MgB_2 wires for the Superconducting Link Project at CERN," *Superconductor science technology*, vol. 29, no. 8, 2016. DOI: 10.1088/0953-2048/29/8/084005.

[63] R. Courant, "Variational methods for the solution of problems of equilibrium and vibrations," *Bulletin of the American Mathematical Society*, vol. 49, 1943.

[64] O. C. Zienkiewicz and R. L. Taylor, *The Finite Element Method for Solid and Structural Mechanics*, 6th ed. Elsevier Butterworth-Heinemann, 2005.

[65] J. N. Reddy, *An introduction to the finite element method*, 2nd ed. Mcgraw-Hill, 1993.

[66] I. Babuška and T. Strouboulis, *The Finite Element Method and its Reliability.* Oxford University Press, 2001. DOI: 10.1093/oso/9780198502760.001.0001.

[67] Ansys Inc. [Online]. Available: https://www.ansys.com/.

[68] S. Farinon, "Notes from the lectures of the course: *Design of superconductor magnets*," PhD in Physics and Nanoscience, XXXVIII Cicle.

[69] E. Todesco, "Status and Perspectives of High Field Magnets for Particle Accelerators," *IEEE Transactions on Applied Superconductivity*, vol. 35, no. 5, 2025. DOI: 10.1109/TASC.2025.3558196.

[70] D. Turrioni, E. Barzi, M. Bossert, *et al.*, "Effects of Rutherford Cable Parameters on Nb_3Sn Extracted Strand Deformation and Performance," *IEEE Transactions on Applied Superconductivity*, vol. 18, no. 2, 2008. DOI: 10.1109/TASC.2008.922386.

[71] A. A. Polyanskii, P. J. Lee, M. C. Jewell, *et al.*, "Evidence for highly localized damage in internal tin and powder-in-tube Nb_3Sn strands rolled before reaction obtained from coupled magneto-optical imaging and confocal laser scanning microscopy," *Superconductor Science and Technology*, vol. 22, no. 9, Aug. 2009. DOI: 10.1088/0953-2048/22/9/095008.

[72] M. Brown, C. Tarantini, W. Starch, W. Oates, P. J. Lee, and D. C. Larbalestier, "Correlation of filament distortion and RRR degradation in drawn and rolled PIT and RRP Nb_3Sn wires," *Superconductor Science and Technology*, vol. 29, no. 8, Jul. 2016. DOI: 10.1088/0953-2048/29/8/084008.

[73] S. C. Hopkins, B. Medina-Clavijo, C. Rastoll, *et al.*, "Deformation Behavior and Degradation on Rutherford Cabling of Nb_3Sn Wires," *IEEE Transactions on Applied Superconductivity*, vol. 34, no. 3, 2024. DOI: 10.1109/TASC.2024.3375274.

[74] S. Farinon, T. Boutboul, A. Devred, D. Leroy, and L. Oberli, "Nb_3Sn Wire Layout Optimization to Reduce Cabling Degradation," *IEEE Transactions on Applied Superconductivity*, vol. 18, no. 2, 2008. DOI: 10.1109/TASC.2008.922299.

[75] V. Previtali, T. Boutboul, S. Le Naour, D. Leroy, and L. Oberli, "Critical Current Studies on Nb-Ti Deformed-Strands," *IEEE Transactions on Applied Superconductivity*, vol. 16, no. 2, 2006. DOI: 10.1109/TASC.2006.873348.

[76] E. Barzi, N. Andreev, B. Bordini, *et al.*, "Instabilities in transport current measurements of Nb_3Sn strands," *IEEE Transactions on Applied Superconductivity*, vol. 15, no. 2, 2005. DOI: 10.1109/TASC.2005.848906.

[77] D. Turrioni, E. Barzi, M. Bossert, *et al.*, "Study of effects of deformation in Nb_3Sn multifilamentary strands," *IEEE Transactions on Applied Superconductivity*, vol. 17, no. 2, 2007. DOI: 10.1109/TASC.2007.899352.

[78] S. Farinon, T. Boutboul, A. Devred, P. Fabbricatore, D. Leroy, and L. Oberli, "Finite Element Model to Study the Deformations of Nb_3Sn Wires for the Next European Dipole (NED)," *IEEE Transactions on Applied Superconductivity*, vol. 17, no. 2, 2007. DOI: 10.1109/TASC.2007.899138.

[79] E. Barzi, M. Bossert, and G. Gallo, “A Model to Study Plastic Deformation in RRP Nb_3Sn Wires,” *IEEE Transactions on Applied Superconductivity*, vol. 21, no. 3, 2011. DOI: 10.1109/TASC.2011.2108991.

[80] E. Rochepault, D. Arbelaez, I. Pong, and D. R. Dietderich, “Analysis and Modeling of Damage in RRP Nb_3Sn Wires During Cabling,” *IEEE Transactions on Applied Superconductivity*, vol. 25, no. 3, 2015. DOI: 10.1109/TASC.2014.2385471.

[81] P. Ferracin, G. Ambrosio, M. Anerella, *et al.*, “Development of MQXF: The Nb_3Sn Low- β Quadrupole for the HiLumi LHC,” *IEEE Transactions on Applied Superconductivity*, vol. 26, no. 4, 2016. DOI: 10.1109/TASC.2015.2510508.

[82] L. D. Cooley, A. K. Ghosh, D. R. Dietderich, and I. Pong, “Conductor Specification and Validation for High-Luminosity LHC Quadrupole Magnets,” *IEEE Transactions on Applied Superconductivity*, vol. 27, no. 4, 2017. DOI: 10.1109/TASC.2017.2648738.

[83] ImageJ. [Online]. Available: https://imagej.net/ij/.

[84] A. Devred, B. Baudouy, D. E. Baynham, *et al.*, “Overview and status of the next european dipole joint research activity,” *Superconductor Science and Technology*, vol. 19, no. 3, Feb. 2006. DOI: 10.1088/0953-2048/19/3/010.

[85] S. Pfeiffer, T. Baumgartner, S. Löffler, *et al.*, “Analysis of inhomogeneities in nb3sn wires by combined sem and shpm and their impact on jc and tc,” *Superconductor Science and Technology*, vol. 36, no. 4, Feb. 2023. DOI: 10.1088/1361-6668/acb857.

[86] S. Burioli, R. Cereseto, M. Frascio, *et al.*, “A New Experimental Setup to Measure the Critical Current of Nb_3Sn Wires at 4.2 K Imposing a Controlled Transverse Deformation,” *IEEE Transactions on Applied Superconductivity*, vol. 35, no. 5, 2025. DOI: 10.1109/TASC.2024.3520097.

[87] C. Calzolaio, G. Mondonico, A. Ballarino, *et al.*, “Electro-mechanical properties of PIT Nb_3Sn wires under transverse stress: experimental results and FEM analysis,” *Superconductor Science and Technology*, vol. 28, no. 5, 2015. DOI: 10.1088/0953-2048/28/5/055014.

[88] L. Gämperle, J. Ferradas, C. Barth, B. Bordini, D. Tommasini, and C. Senatore, “Determination of the electromechanical limits of high-performance Nb_3Sn rutherford cables under transverse stress from a single-wire experiment,” *Phys. Rev. Res.*, vol. 2, 1 2020. DOI: 10.1103/PhysRevResearch.2.013211.

[89] J. F. Troitino, T. Bagni, C. Barth, *et al.*, "Effects of the initial axial strain state on the response to transverse stress of high-performance RRP Nb_3Sn wires," *Superconductor Science and Technology*, vol. 34, no. 3, 2021. DOI: 10.1088/1361-6668/abd388.

[90] T. Bagni, C. Calzolaio, G. Bovone, *et al.*, "Investigating the effect of rolling deformation on the electro-mechanical limits of Nb3Sn wires produced by RRP® and PIT technologies," *Superconductor Science and Technology*, vol. 37, no. 9, 2024. DOI: 10.1088/1361-6668/ad6a9c.

[91] C. Scheuerlein, M. Di Michiel, and A. Haibel, "On the formation of voids in internal tin Nb_3Sn superconductors," *Applied Physics Letters*, vol. 90, no. 13, 2007. DOI: 10.1063/1.2716346.

[92] A. Ballarino, "Design of an mgb_2 feeder system to connect groups of superconducting magnets to remote power converters," vol. 234, no. 3, Jun. 2010. DOI: 10.1088/1742-6596/234/3/032003.

[93] K. Konstantopoulou, J. Hurte, P. W. Retz, and A. Ballarino, "Design optimization and evaluation of the 3 kA MgB_2 cable at 4.3 K for the superconducting link project at CERN," *Superconductor Science and Technology*, vol. 32, no. 8, Jul. 2019. DOI: 10.1088/1361-6668/ab13e7.

[94] S. Yamada, Y. Hishinuma, T. Uede, K. Schippl, and O. Motojima, "Study on 1 GW class hybrid energy transfer line of hydrogen and electricity," *Journal of Physics: Conference Series*, vol. 97, no. 1, Feb. 2008. DOI: 10.1088/1742-6596/97/1/012167. [Online]. Available: https://doi.org/10.1088/1742-6596/97/1/012167.

[95] V. Vysotsky, I. Antyukhov, V. Firsov, *et al.*, "Energy transfer with hydrogen and superconductivity – the review of the first experimental results," *Physics Procedia*, vol. 65, 2015, Proceedings of the 27th International Symposium on Superconductivity (ISS 2014) November 25-27, 2014, Tokyo, Japan. DOI: https://doi.org/10.1016/j.phpro.2015.05.158.

[96] L. Cavallucci, A. Musso, G. Angeli, *et al.*, "Optimization Procedure to Design a DC Transmission Line with MgB_2 Wires in Liquid Hydrogen," *IEEE Transactions on Applied Superconductivity*, vol. 35, no. 5, 2025. DOI: 10.1109/TASC.2024.3513946.

[97] S. Palacios, M. J. Wolf, M. Noe, M. Wehr, and T. Arndt, "Design of a 75 km GW-class hybrid pipeline for the synergetic transmission of liquid hydrogen and electrical energy by high-temperature superconductivity," *Superconductor Science and Technology*, vol. 38, no. 12, Dec. 2025. DOI: 10.1088/1361-6668/ae2cf7.

[98] A. Ballarino, "Alternative Design Concepts for Multi-Circuit HTS Link Systems," *IEEE Transactions on Applied Superconductivity*, vol. 21, no. 3, 2011. DOI: 10.1109/TASC.2010.2096378.

[99] J. Fleiter and A. Ballarino, "Results of the Cold Powering Tests of the Demonstrators of HL-LHC SC-Links," *IEEE Transactions on Applied Superconductivity*, vol. 32, no. 4, 2022. DOI: 10.1109/TASC.2022.3172053.

[100] M. Sugano, A. Ballarino, B. Bartova, R. Bjoerstad, C. Scheuerlein, and G. Grasso, "Characterization of Mechanical Properties of MgB_2 Conductor for the Superconducting Link Project at CERN," *IEEE Transactions on Applied Superconductivity*, vol. 25, no. 3, 2015. DOI: 10.1109/TASC.2014.2364740.

[101] M. Sugano, A. Ballarino, B. Bartova, R. Bjoerstad, A. Gerardin, and C. Scheuerlein, "Evaluation of Young's modulus of MgB_2 filaments in composite wires for the superconducting links for the high-luminosity LHC upgrade," *Superconductor Science and Technology*, vol. 29, no. 2, Dec. 2015. DOI: 10.1088/0953-2048/29/2/025009.

[102] V. Kostyuk, E. Blagov, I. Antyukhov, *et al.*, "Cryogenic design and test results of 30-m flexible hybrid energy transfer line with liquid hydrogen and superconducting MgB_2 cable," *Cryogenics*, vol. 66, 2015, ISSN: 0011-2275. DOI: https://doi.org/10.1016/j.cryogenics.2014.11.010.

[103] V. Vysotsky, I. Antyukhov, V. Firsov, *et al.*, "Cryogenic Tests of 30 m Flexible Hybrid Energy Transfer Line with Liquid Hydrogen and Superconducting MgB_2 Cable," *Physics procedia*, vol. 67, 2015, ISSN: 1875-3892.

[104] V. S. Vysotsky, E. V. Blagov, V. V. Kostyuk, *et al.*, "New 30-m Flexible Hybrid Energy Transfer Line With Liquid Hydrogen and Superconducting MgB_2 Cable—Development and Test Results," *IEEE Transactions on Applied Superconductivity*, vol. 25, no. 3, 2015. DOI: 10.1109/TASC.2014.2361635.

[105] Agnes. [Online]. Available: https://www.agnespower.com/.

[106] S. Z. Al Ghafri, S. Munro, U. Cardella, *et al.*, "Hydrogen liquefaction: a review of the fundamental physics, engineering practice and future opportunities," *Energy Environ. Sci.*, vol. 15, 7 2022. DOI: 10.1039/D2EE00099G.

[107] M. Aziz, "Liquid Hydrogen: A Review on Liquefaction, Storage, Transportation, and Safety," *Energies*, vol. 14, no. 18, 2021, ISSN: 1996-1073. DOI: 10.3390/en14185917.

[108] R. Angelico, F. Giametta, B. Bianchi, and P. Catalano, "Green Hydrogen for Energy Transition: A Critical Perspective," *Energies*, vol. 18, no. 2, 2025, ISSN: 1996-1073. DOI: 10.3390/en18020404.

[109] F. Arpino, C. Canale, G. Cortellessa, *et al.*, "Green hydrogen for energy storage and natural gas system decarbonization: An Italian case study," *International Journal of Hydrogen Energy*, vol. 49, 2024, ISSN: 0360-3199. DOI: https://doi.org/10.1016/j.ijhydene.2023.09.299.

[110] M. Ball and M. Weeda, "11 - The hydrogen economy — Vision or reality?" In *Compendium of Hydrogen Energy*, ser. Woodhead Publishing Series in Energy, M. Ball, A. Basile, and T. N. Veziroğlu, Eds., Oxford: Woodhead Publishing, 2016, ISBN: 978-1-78242-364-5. DOI: https://doi.org/10.1016/B978-1-78242-364-5.00011-7.

[111] M. Harada, T. Ichikawa, H. Takagi, and H. Uchida, "14 - building a hydrogen infrastructure in japan," in *Compendium of Hydrogen Energy*, ser. Woodhead Publishing Series in Energy, M. Ball, A. Basile, and T. N. Veziroğlu, Eds., Oxford: Woodhead Publishing, 2016, ISBN: 978-1-78242-364-5. DOI: https://doi.org/10.1016/B978-1-78242-364-5.00014-2.

[112] U. Bünger, J. Michalski, F. Crotogino, and O. Kruck, "7 - large-scale underground storage of hydrogen for the grid integration of renewable energy and other applications," in *Compendium of Hydrogen Energy*, ser. Woodhead Publishing Series in Energy, M. Ball, A. Basile, and T. N. Veziroğlu, Eds., Oxford: Woodhead Publishing, 2016, ISBN: 978-1-78242-364-5. DOI: https://doi.org/10.1016/B978-1-78242-364-5.00007-5.

[113] M. Steen, "12 - building a hydrogen infrastructure in the eu," in *Compendium of Hydrogen Energy*, ser. Woodhead Publishing Series in Energy, M. Ball, A. Basile, and T. N. Veziroğlu, Eds., Oxford: Woodhead Publishing, 2016, ISBN: 978-1-78242-364-5. DOI: https://doi.org/10.1016/B978-1-78242-364-5.00012-9.

[114] C. Wulf and M. Kaltschmitt, "15 - environmental impacts of hydrogen use in vehicles," in *Compendium of Hydrogen Energy*, ser. Woodhead Publishing Series in Energy, M. Ball, A. Basile, and T. N. Veziroğlu, Eds., Oxford: Woodhead

Publishing, 2016, ISBN: 978-1-78242-364-5. DOI: https://doi.org/10.1016/B978-1-78242-364-5.00015-4.

[115] J. Wind, "1 - hydrogen-fueled road automobiles – passenger cars and buses," in *Compendium of Hydrogen Energy*, ser. Woodhead Publishing Series in Energy, M. Ball, A. Basile, and T. N. Veziroğlu, Eds., Oxford: Woodhead Publishing, 2016, ISBN: 978-1-78242-364-5. DOI: https://doi.org/10.1016/B978-1-78242-364-5.00001-4.

[116] B. Parkinson, P. Balcombe, J. F. Speirs, A. D. Hawkes, and K. Hellgardt, "Levelized cost of CO2 mitigation from hydrogen production routes," *Energy Environ. Sci.*, vol. 12, 1 2019. DOI: 10.1039/C8EE02079E.

[117] A. Alekseev, "Hydrogen Liquefaction," in *Hydrogen Science and Engineering : Materials, Processes, Systems and Technology*. John Wiley Sons, Ltd, 2016, ch. 30, ISBN: 9783527674268. DOI: https://doi.org/10.1002/9783527674268.ch30.

[118] J. Dewar, "Preliminary Note on the Liquefaction of Hydrogen and Helium," *Science*, vol. 8, no. 183, 1898. DOI: 10.1126/science.8.183.3.

[119] K. Reddi, M. Mintz, A. Elgowainy, and E. Sutherland, "13 - Building a hydrogen infrastructure in the United States," in *Compendium of Hydrogen Energy*, ser. Woodhead Publishing Series in Energy, M. Ball, A. Basile, and T. N. Veziroğlu, Eds., Oxford: Woodhead Publishing, 2016, ISBN: 978-1-78242-364-5. DOI: https://doi.org/10.1016/B978-1-78242-364-5.00013-0.

[120] A. Abdi, J. N. Chiu, and V. Martin, "State of the art in hydrogen liquefaction," *Proceedings of the ISES Solar World Congress 2019*, 2019. DOI: 10.18086/swc.2019.23.01.

[121] S. Krasae-in, J. H. Stang, and P. Neksa, "Development of large-scale hydrogen liquefaction processes from 1898 to 2009," *International Journal of Hydrogen Energy*, vol. 35, no. 10, 2010, Novel Hydrogen Production Technologies and Applications, ISSN: 0360-3199. DOI: https://doi.org/10.1016/j.ijhydene.2010.02.109.

[122] K. Ohlig and L. Decker, "The latest developments and outlook for hydrogen liquefaction technology," *AIP Conference Proceedings*, vol. 1573, no. 1, 2014, ISSN: 0094-243X. DOI: 10.1063/1.4860858.

[123] M. Cais, M. Nicoli, M. Gandiglio, *et al.*, "Hybrid superconducting energy pipelines: key cost thresholds and system implications for Italy," *International Journal of Hydrogen Energy*, vol. 210, 2026, ISSN: 0360-3199. DOI: https://doi.org/10.1016/j.ijhydene.2026.153627.

[124] L. Cavallucci, M. Breschi, A. Macchiagodena, *et al.*, "Analysis of Electric Fault in a MV DC MgB_2 Transmission Line Cooled by Liquid Hydrogen," *IEEE Transactions on Applied Superconductivity*, vol. 36, no. 5, 2026. DOI: 10.1109/TASC.2026.3655642.

[125] G. Mangiulli, M. Bracco, M. Breschi, *et al.*, "Sizing and Economic Assessment for Auxiliar Components and Grid Connection of a MgB_2-LH_2 Hybrid Power Cable," *IEEE Transactions on Applied Superconductivity*, vol. 36, no. 5, 2026. DOI: 10.1109/TASC.2026.3651232.

[126] L. Savoldi, M. Bracco, M. Breschi, *et al.*, "Analysis of the Evolution of Accidental Transients in the Cooling of a MgB_2-LH_2 Hybrid Power Cable," *IEEE Transactions on Applied Superconductivity*, vol. 36, no. 5, 2026. DOI: 10.1109/TASC.2026.3651230.

[127] [Online]. Available: https://ouco-industry.com/offshore-pipe-laying-the-ultimate-guide/.

[128] L. Savoldi, D. Placido, and S. Viarengo, "Thermal-hydraulic analysis of superconducting cables for energy applications with a novel open object-oriented software: OPENSC2," *Cryogenics*, vol. 124, 2022, ISSN: 0011-2275. DOI: https://doi.org/10.1016/j.cryogenics.2022.103457.

[129] M. Nicoli, V. A. D. Faria, A. R. de Queiroz, and L. Savoldi, "Modeling energy storage in long-term capacity expansion energy planning: an analysis of the Italian system," *Journal of Energy Storage*, vol. 101, 2024, ISSN: 2352-152X. DOI: https://doi.org/10.1016/j.est.2024.113814.

[130] Kováč, P and Búran, M and Kováč, J and Melišek, T and Hušek, I and Berek, D and Mauceri, P and Spina, T and Bruzek, Ch-E, vol. 37, no. 6, 2024. DOI: 10.1088/1361-6668/ad3f7e.

[131] E. Barzi, G. Gallo, and P. Neri, "FEM Analysis of Nb-Sn Rutherford-Type Cables," *IEEE Transactions on Applied Superconductivity*, vol. 22, no. 3, 2012. DOI: 10.1109/TASC.2012.2186951.

[132] A. Baskys, J.-F. Croteau, M. Naus, *et al.*, “RRP Nb_3Sn Subelement Shear Dependence on Hexagonal Subelement Stack Orientation and the Strand’s Position Within a Rutherford Cable,” *IEEE Transactions on Applied Superconductivity*, vol. 33, no. 5, 2023. DOI: 10.1109/TASC.2023.3265910.